2018-03-01

Rotational Stiffness Models for Shallow Embedded Column-to-Footing Connections

Ashley Lauren Sadler
Brigham Young University

Rotational Stiffness Models for Shallow Embedded Column-to-Footing Connections

Ashley Lauren Sadler

A thesis submitted to the faculty of
Brigham Young University
in partial fulfillment of the requirements for the degree of

Master of Science

Paul W. Richards, Chair
Fernando S. Fonseca
Kyle M. Rollins

Department of Civil and Environmental Engineering

Brigham Young University

ABSTRACT

Rotational Stiffness Models for Shallow Embedded
Column-to-Footing Connections

Ashley Lauren Sadler
Department of Civil and Environmental Engineering, BYU
Master of Science

Shallow embedded steel column connections are widely used in steel buildings; however, there is insufficient research about this connection type to understand the actual rotational stiffness that the connection provides. Shallow embedded steel columns are when a steel column is anchored to the foundation slab and then unreinforced concrete is poured around the base plate and the base of the column. This thesis seeks to further quantify the rotational stiffness available in this type of connection due to the added concrete and improve an existing model in order to represent the rotational stiffness.

Existing data from two series of experiments on shallow embedded columns were used to validate and improve an existing rotational stiffness model. These two data sets were reduced in the same manner so that they could be compared to one another. In addition, the rotational stiffness for each test column was determined so they could be evaluated against the outputs of the model.

The existing model was improved by evaluating each parameter in the model: the modulus of subgrade reaction, exposed column length, modulus of concrete for the blockout and the foundation slab, flange effective width, embedment depth, and effective column depth. It was determined that the model was sensitive to the subgrade reaction, modulus of concrete, embedment depth and effective column depth. The exposed length was not a highly sensitive parameter to the model. Flange effective width was determined to not be needed, especially when the other parameters were altered.

In order to test the sensitivity of the total stiffness to the rotational stiffness, equations were developed using the stiffness method for several different moment frame configurations with partial fixity at the column base. It was seen that if the rotational stiffness was changed by 100% then there could be seen a change in the total stiffness was only up to 20%.

Keywords: steel columns, shallowly embedded connections, rotational stiffness, blockout

ACKNOWLEDGEMENTS

This thesis would not have been possible without the support of several people, which I would like to thank. I would like to first acknowledge the constant support and advice from my committee chair Dr. Paul Richards. Without his time and effort this research would not have progressed as much as it did. I would also like to thank my family and friends for their constant support and encouragement. Finally, I want to thank the American Institute of Steel Construction which provided funding for this project.

TABLE OF CONTENTS

LIST OF TABLES

LIST OF FIGURES

1 INTRODUCTION

1.1 Overview of Steel Column-to-Footing Connections

Steel is one of the most affordable and durable materials, which is why it is commonly used for framing multi-story buildings. Concrete is also an efficient material and is typically used for the foundations of steel buildings. One of the most common connections in construction is the connection of a steel column to a concrete footing. Figure 1-1 shows how this connection is often accomplished, by leaving a square hole (blockout) in the floor slab, so that the steel column can be bolted directly to the footing under the slab. After the column is installed the square hole (blockout) is filled in with concrete, hiding the bolts and base plate; no extra reinforcing steel is added in the blockout section.

Figure 1-2 shows the configuration for another common steel column to concrete footing connection, an exposed column base plate. It can be seen that the major difference between the two figures is the blockout. The exposed base plate in Figure 1-2 does not have a concrete blockout around the column and the base plate.

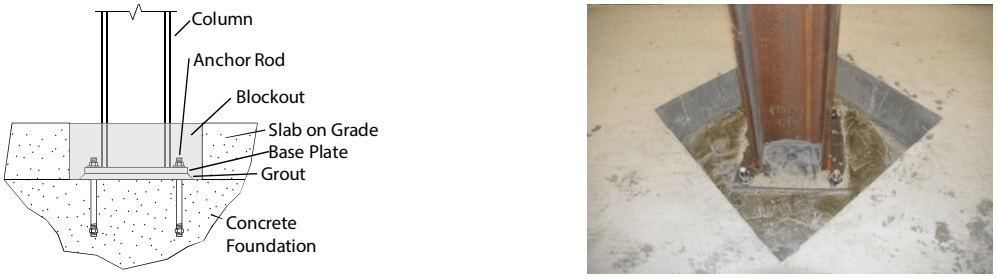

Figure 1-1: Blockout connection commonly used at the base of steel buildings: (a) detail; (b) picture of blockout just after column installation and prior to pouring of blockout concrete.

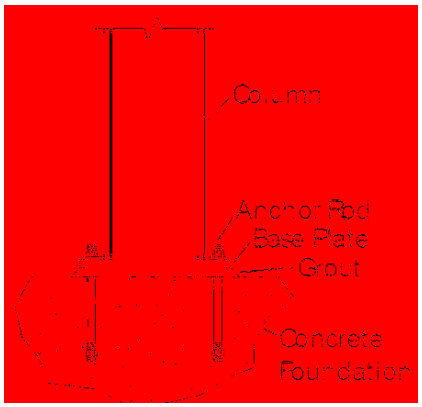

Figure 1-2: Exposed base plate connection commonly used at the base of steel buildings.

1.2 Motivation

Engineers and researchers rely heavily on computer simulations to estimate how buildings will respond to earthquakes. In order to have accurate computer models, engineers and researchers need to be able to put elements into a computer model to reasonably reflect the rotational stiffness at the bottom of the base columns. Most studies assume the columns are "pinned" or "fixed" at the base. This may be reasonable in some circumstances; overall, it may result in inaccurate building drifts or inaccurate moment demands on footings.

Prior to 2014, experiments had not been performed to determine the rotational stiffness of the connection shown in Figure 1-1, and engineers and researchers did not know how to properly simulate them. In response to this need, the American Institute of Steel Construction (AISC) sponsored a multi-year project at Brigham Young University (BYU) and University of California, Davis (UC Davis) to develop recommendations.

During the recent years, Barnwell (2015) and Hanks (2016) completed separate series of experiments on column-to-footing connections similar to the one shown in Figure 1-1 Around the same time, two series of large-scale experiments were conducted at UC Davis (Grilli and Kanvinde 2015). Further research was done by Tyron (2016) who created a model to predict the

rotational stiffness of such connections; he used values from Barnwell's tests to calibrate his model.

1.3 Scope of Research

The purpose of this research was to evaluate the recently generated experimental data collectively, and to develop a rotational stiffness model that engineers and researchers can use in computer models to simulate the response of buildings from earthquakes. Tryon's original model was refined based on observations from the experimental data.

The research that was accomplished can be separated into three sections. First, all recent experimental data was evaluated; second, the existing mathematical model was refined to better represent all of the data; and third, several moment frame configurations were evaluated with a closed form solution of the total stiffness to determine the sensitivity of the rotational stiffness.

1.4 Outline

This chapter has included a brief introduction to the research that was conducted and to introduce the motivation for additional research. Chapter 2 reviews the current literature on column-to-footing connections. Chapter 3 describes the method used for data reduction of Barnwell's and Hanks' data sets. The description of the modification of Tryon's model is discussed in Chapter 4. The system level sensitivity of different configurations and Tryon's modified model is discussed in Chapter 5. Finally, conclusions are presented in Chapter 6.

2 LITERATURE REVIEW

2.1 Exposed Column Base Plate Connections

Exposed base plate connections were introduced in Section 1.1 (Figure 1-1). A great deal of research has been performed on these connections and the models are fairly accurate in predicting the rotational stiffness. Even though these models are not perfect for embedded columns, they provide a good starting point for the interaction of the base plate and concrete foundation.

2.1.1 DeWolf and Sarisley (1980)

DeWolf and Sarisley (1980), investigated the strength of exposed base plate connections. They used two methods, the working stress and the ultimate strength methods, to determine the strength of the connections. Figure 2-1 shows the compression block for both methods. They conducted 16 tests to compare the models' results, Table 2-1 shows the test matrix. The 16 specimens were tested by inducing a moment on the column from an axial load with an eccentricity. The main differences between the two models were the compression block. The working stress method had a triangular distributed bearing stress and the ultimate strength method was modeled as a rectangular stress block. The average factor of safety was 2.16 for the working stress method and 1.11 for the ultimate strength method.

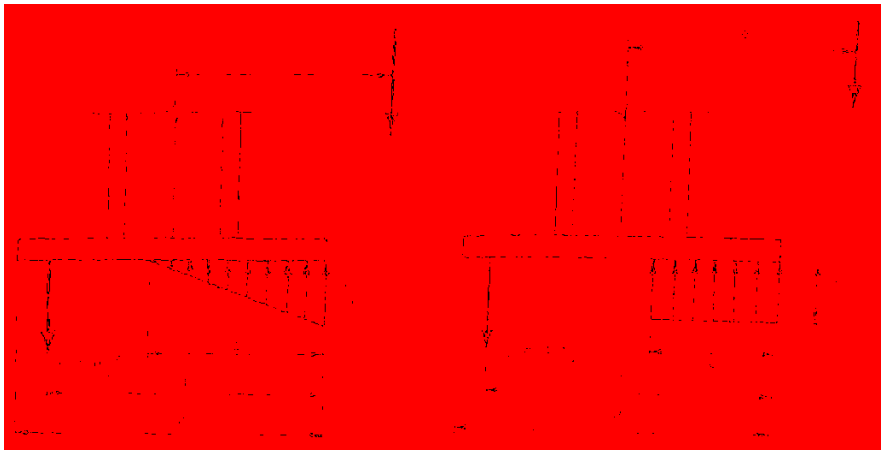

(a) Working stress Method **b) Ultimate Strength Method**

Figure 2-1: Base Plate Strength Methods (DeWolf and Sarisley 1980).

Table 2-1: Specimen Test Matrix and Results (DeWolf and Sarisley 1980)

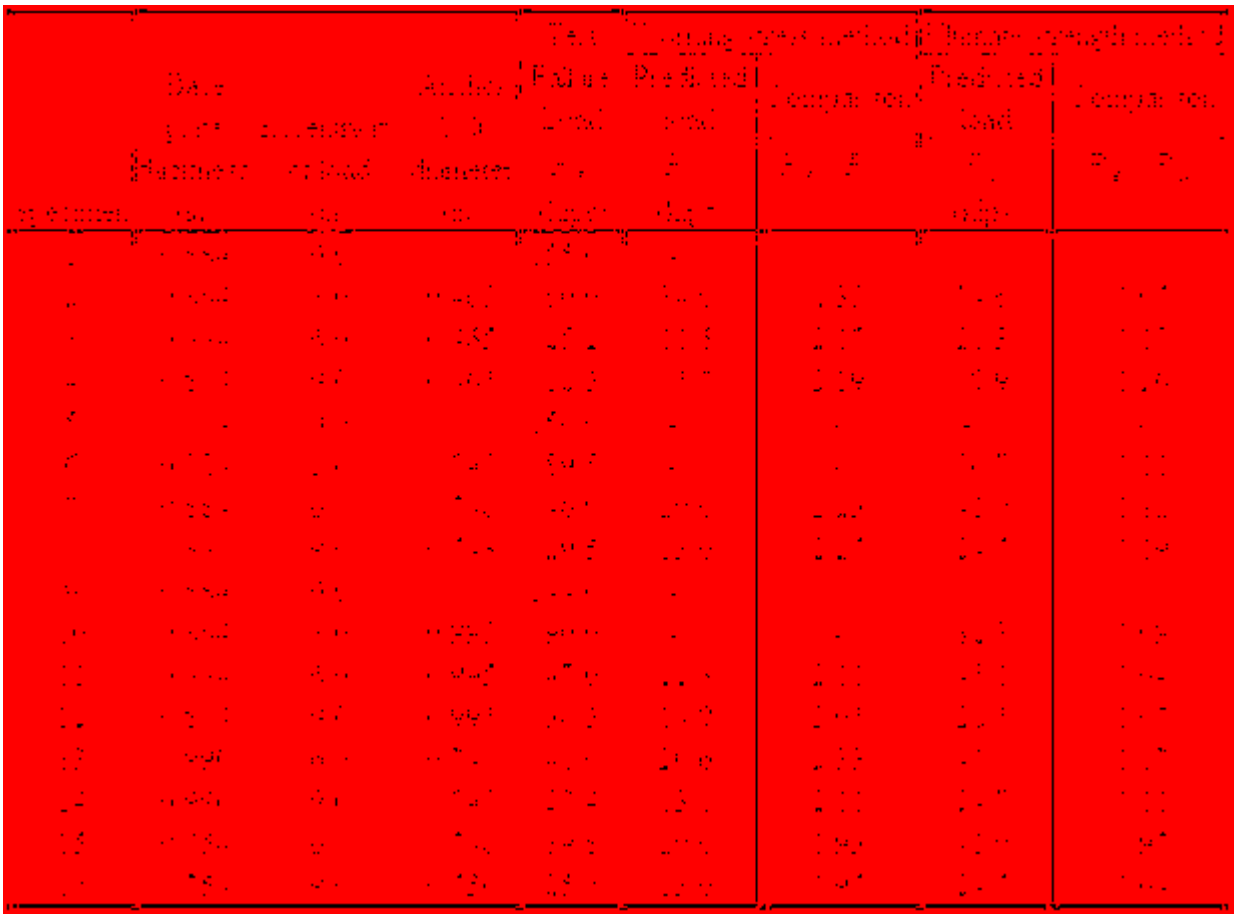

The authors reached three conclusions from their experiments:

1. When the diameter of the anchor bolts was large in comparison to the base plate dimensions, then the distance from the anchor bolt to the bearing zone of the plate on the concrete was small. The smaller bearing area, did not allow the anchor bolt to reach capacity, and therefore, some of the bolts were ineffective.
2. When the concrete area was greater than the base plate area, then a confining effect needed to be accounted for in the design.
3. Increased plate thickness decreased capacity at a point, due to the plate acting like a rigid plate and would cause premature failure. This was due to large bearing stresses from the plate not being as flexible.

The authors recommended that the ultimate strength method be used for design, because it more accurately predicted the connection behavior.

2.1.2 Kanvinde and Deierlein (2011)

Kanvinde and Deierlein (2011), conducted experiments on 20 exposed base plate connections. These tests were meant to be compared to the AISC Design Guide (Fisher and Kloiber 2006), which is the current standard for designing exposed column base plate connections. They also were concerned with the behavior of the columns for three different scenarios which were tested to failure: an applied axial load with an eccentricity to induce a moment, an axial load and a shear force applied at the base of the column, and an axial and moment loads on columns designed to isolate the column to base plate weld. The first two mechanisms had seven specimens in the test series and the final mechanism had 6 specimens. All specimens were constructed to two-third scale and then tested to failure.

The authors reached the following conclusions for each mechanism:

1. Moment Capacity
    i. All tests showed "excellent deformation capacity" with little strength degradation until after 7% - 10% drift. This suggested that the current design assumption, i.e., the base plate remaining elastic, may be rather conservative and significant deformation and energy dissipation capacity were available in the base plate.
    ii. The *AISC Design Guide* gave highly conservative predictions. It was observed that the experimental data showed connection strengths that were 80% greater than the predicted values on average.
2. Shear Capacity
    i. A coefficient of friction value of 0.45 was recommended to be used between the grout and steel. This was slightly higher than the value recommended in *AISC Design Guide* of 0.40.
    ii. The *AISC Design Guide* was accurate for shear loads resisted by anchor bolts. The bolts should be checked for the interaction between flexural axial forces and direct axial loads.
    iii. Concrete Capacity Design (CCD) was recommended for use in design when a shear key or shear lug is used, since the current method of 45° cone method was not conservative.

3. Weld Capacity
    i. The Complete Joint Penetration (CJP) and Partial Joint Penetration (PJP) were both adequate for use in seismic design, which could withstand up to 3% to 5% drift.
    ii. PJP performed better than the CJP. This was attributed to the stress concentrations that form around the access hole for the CJP groove weld.

2.1.3 Kanvinde et al. (2011)

Kanvinde et al. (2011) focused on the rotational stiffness of exposed column base connections, due to the fact that this element is often ignored in the design process. They developed an analytical model which was validated with nine experimental specimens.

Their method to estimate the design stiffness of base connections had three steps:

1. Determine the design strength and internal force distribution
2. Determine the deformation under high eccentricity
3. Calculate the connection rotation for each individual component

The components that contributed to the total deformation were the stretching of anchor rods that were in tension, the bending of the plate on the tension and compression sides, and the deformation of the concrete under the compression side of the plate; Figure 2-2 depicts these different deformations.

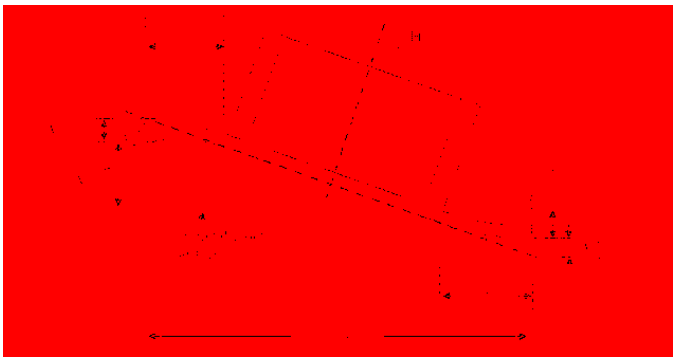

Figure 2-2: Model of various deformation (Kanvinde et al. 2011).

The authors stated that the design of the connections cannot be classified as pinned or fixed, for it was somewhere in the middle. The classification of the base fixity was important for the design, for if the column was designed as fixed, then increased story drift could occur in the first story. Additionally, if the connection was designed as pinned then it would be possible for a more conservative response. Therefore, for safety and economy reasons it is important to understand the true fixity of the connection.

The authors warned that there were a few inherent inaccuracies in the method that was included from the AISC Design Guide (Fisher and Kloiber 2006). One of the main assumption was the shape of the stress block. Both of these models assume that the stress block was rectangular; however, this was not a perfect representation of the behavior.

2.1.4 Kanvinde et al. (2013)

Kanvinde et al. (2013) investigated the connection response of exposed base plate connections by adjusting the base plate thickness. They noted that previous models had simplified assumptions in order to perform tests, since it was extremely difficult to test individual components due to the highly interactive nature of all the components. Therefore, the

authors performed finite element analysis in order to isolate single components. They then validated the model with physical experiments.

From these comparisons, the authors noted that the current method for determining the rotational stiffness may be adequate; however, a perfect prediction would be too complex for normal design situations. It was additionally noted that the thickness of the base plate should be a key factor in the design formulas since it was seen that a thicker base plate increased the connection stiffness capacity.

The important finding from their finite element analysis was that the rectangular compression block may be non-conservative for thicker plates since thicker plates tend to have higher stress concentrations at the toe of the compression side of the base plate.

2.2 Embedded Column Connections

Embedded column connections were introduced in Section 1.1 (Figure 1-2) and are formed by pouring concrete around the base of the column after the foundation and main slab have been poured and the steel columns has been anchored into place. These connections are commonly used due to the ease of construction as well as it being more aesthetically pleasing. However, there is limited research on the behavior of this type of connection.

2.2.1 Cui et al. (2009)

Cui et al. (2009) conducted experiments to investigate the effect of earthquake loads on shallow-embedded column base connections, specifically the effect on the slab. Their tests included eight two-third scale HSS columns. They investigated the effects of slab thickness, shape, and reinforcement on elastic stiffness, strength, and energy dissipation capacity of the embedded column.

The test specimens were all constructed from HSS 200 mm tubes. Seven columns had 9 mm tube thickness and one column had 12 mm tube thickness. The base plates were all 25-mm thick and 300 mm square. Each base plate had twelve anchor bolts spread evenly around the base plate and the foundation was designed to be stiff enough that the anchor bolts governed the strength. One of the specimens was left with an exposed base plate to act as the control. The other seven had varying amounts of reinforcement and slab shapes. The columns were all loaded axially with a 511 kN load.

The authors reasoned that the contribution of the concrete slab to resist the applied moment was provided by two mechanisms: 1) The direct bearing of the slab on the column in compression, and 2) Punching resistance of the slab from the rotation of the base plate.

The authors reached six conclusions from their experiments.

1. The elastic stiffness, maximum strength, and dissipated energy saw improvement with the inclusion of the floor slab.
2. The thickness and shape of the floor slab caused significant changes in the maximum strength. The inclusion of horizontal rebar also greatly improved the strength.
3. Horizontal rebar increased the deformation capacity.
4. The main failure mode was punching shear in the column slab. This was true until the column base connection strength was increased to be larger than the plastic moment of the column, then the column failed in local buckling.
5. A strengthened slab and elevated foundation slab shape should be used.

6. The plastic theory could reasonably estimate the maximum strength of the column regardless of thickness and geometric shape of the floor slab, with less than 20% error.

2.2.2 Grilli and Kanvinde (2015)

Grilli and Kanvinde (2015) investigated the performance of embedded column base connections under seismic loads. They tested five full scale test specimens with the consideration of three main variables: embedment depth, column size, and axial load, Table 2-2 summarizes the tests conducted. The specimens were constructed by a welding a base plate to a wide flange shape. They also welded a stiffener on the column where the blockout slab would end. Their purpose was for the base plate to be used in uplift resistance and the stiffener for compression resistance.

Table 2-2: Specimen Test Matrix (Grilli and Kanvinde 2015)

Test #	Column Size, (b_f [mm])	P [kN]	d_{embed} [mm]	Base Plate, $t_p \times N \times B$ [mm]	Z [m]	M_{base}^{max} [kN-m]	β_{base}^{test} * [10^5 kN-m/rad]	$\frac{\Delta_{test}}{\Delta_{fixed}}$ ***	$\frac{M_{base}^{y}}{M_{base}^{max}}$	Λ_{max} (%)
1	W14x370 (419)	445 (C)	508	51 × 762 × 762	2.84	2579(+)	3.23	1.21	0.87	3.85
						2613(-)			0.69	3.82
2	W18x311 (305)			51 × 864 × 711		2324(+)	3.84	1.16	0.709	3.01
						2168(-)			0.66	2.89
3	W14x370 (419)	0	762	51 × 762 × 762	3.10	3741(+)	3.07	1.30	0.72	6.97
						3444(-)			0.67	7.77
4		445 (C)				4124 (+)	3.38	1.30	0.66	6.48
						3612(-)			0.81	5.09
5		667 (T)				3800 (+)	3.25	1.29	0.73	2.72**
						3464(-)			0.72	2.65**
							Mean	**1.25**	**0.72**	**4.98**
							CoV	**0.05**	**0.07**	**0.38**

*Average stiffness of both directions
**Test terminated due to slip prior to failure (Mean, COV does not include these data points)
***Notional columns used for Tests #1-5 are W14X145, W14X132, W14X193, W14X211, and W14X193 respectively.

These experiments demonstrated that the strength and stiffness of the embedded column were greater than that of the exposed base connection and that the stiffness increased as the embedment depth increased. Another observation was that increased connection strength occurred with increased flange width. In the experiments, there was a correlation between compressive axial load and strength compared with that of no applied load; however, no correlation was seen for a tensile load. Finally, strength and stiffness were seen to decrease as the concrete cracked.

The authors also proposed a strength model calibrated from their experimental data. The model was based on three mechanisms. The first was horizontal bearing stress that acts on the column flanges. The second was the vertical bearing stresses that act on the embedded base plate at the bottom of the column, and the third was panel shear. The authors suggested that their model was applicable for deeper columns; however, for shallow embedment, a model like Barnwell's (2015) or any other model that was better suited. A final note by the authors was about connection fixity. They stated that although their column connections were designed as if they were fixed, there was still some flexibility in the connection, which should be accounted for during design.

2.2.3 Barnwell (2015)

Figure 2-3 showed Barnwell's test setup. He investigated shallow-embedded columns with blockout concrete. The test matrix included twelve two-third scale specimens in order to investigate the effect of the blockout concrete on the rotational stiffness and overall strength of the connection. The original eight specimens are shown in Table 2-3. Four additional tests were conducted on four of the eight original specimens as summarized in Table 2-4. All specimens were tested to failure and had four anchor bolts located in the corners of the base plate.

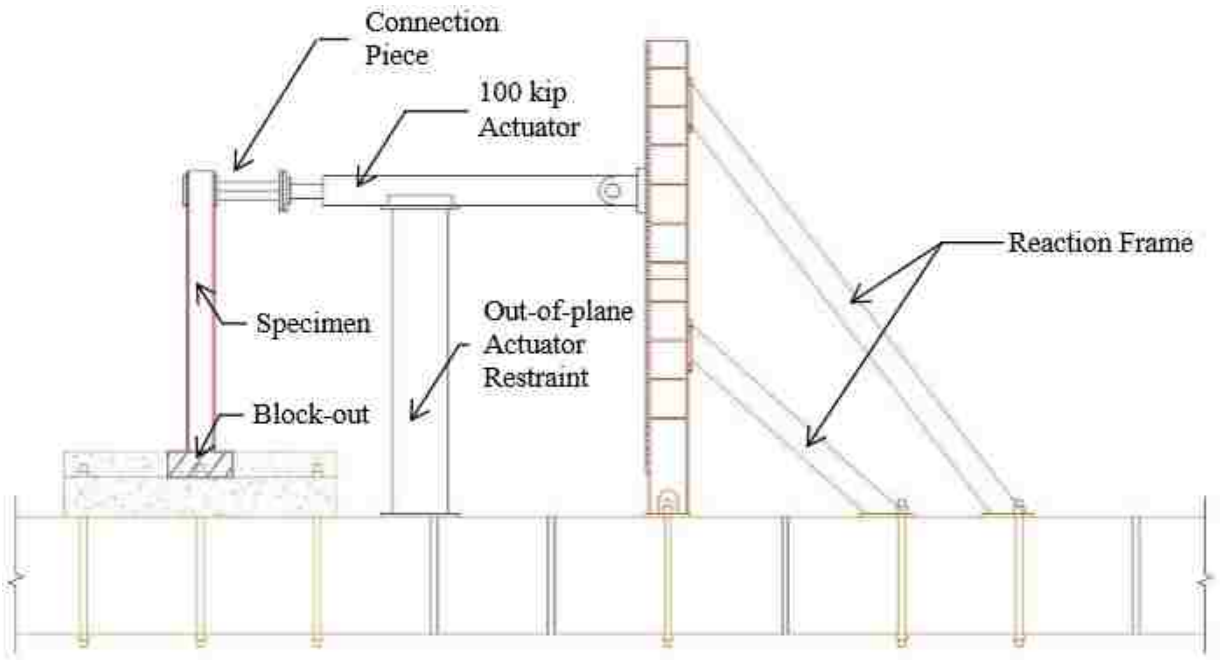

Figure 2-3: Barnwell's test setup used for first and second testing (Barnwell 2015).

Table 2-3: Original Specimen Test Matrix (Barnwell 2015)

Specimen	Embedment [in]	Orientation	Shape
A1	8	Strong	W8 × 35
A2	8	Strong	W8 × 48
A3	8	Weak	W8 × 35
A4	8	Weak	W8 × 48
B1	16	Strong	W8 × 35
B2	16	Strong	W8 × 48
B3	16	Weak	W8 × 35
B4	16	Weak	W8 × 48

Table 2-4: Retested Specimen Test Matrix (Barnwell 2015)

Specimen	Embedment [in]	Orientation	Shape	Braced Slab
CA2	8	Strong	W8 × 48	Y
CA2	8	Strong	W8 × 48	N
CB2	16	Strong	W8 × 48	Y
CB2	16	Strong	W8 × 48	N

Barnwell reached the following conclusions:

1. Strength from the specimens was higher than the predicted values from *AISC Design Guide*, and rotational stiffness increased with the depth of the blockout concrete.
2. The compression resultant was not located underneath the baseplate. This is unlike what was assumed with an exposed base plate column connection. The resultant compression block was instead found to be located a distance farther away from the edge of the base plate.
3. The compression block resultant could be determined using a 45-degree line from the compression face of the column to the base slab/ blockout interface.

2.2.4 Tryon (2016)

Tryon (2016) developed a numerical model to predict the stiffness of shallowly embedded column-to-footing connections. The model had three parts: the exposed column, embedded portion of the column, and the base plate as shown in Figure 2-4. The first part, the exposed section of the column, was analyzed using classic Bernoulli beam theory. The second part, was the portion of the column that was encased in concrete, was analyzed using the closed-form

solutions developed by Hetényi for beams of infinite length (Hetényi 1971). The final part, the base plate, was modeled as a rotational spring.

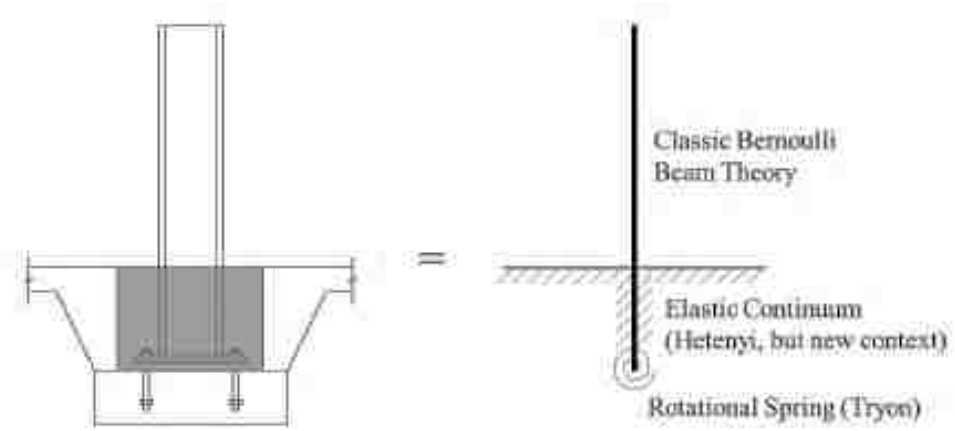

Figure 2-4: Model for embedded column connection (Tryon, 2016).

The main parameters in Tryon's continuum model were the embedment depth, exposed length of the column, modulus of subgrade reaction, flange effective width (Tryon called this parameter flange duality). In order for the governing equations of Hetényi's beams of infinite length to be relevant to shallow-embedded columns, the separate parameters were calibrated. The data from Barnwell's experiment was used for calibration and testing of the model.

The main equations in Tryon's model for the rotational stiffness of the base plate are Equation (2-1) and Equation (2-2). Equation (2-1) represents the rotational stiffness of the base plate when the column is oriented in the strong axis. The rotational stiffness for the weak axis orientation is represented in Equation (2-2).

$$k_s = \frac{kd^3}{24}\left(\frac{b_f}{2b_f - t_w}\right)\left(\frac{E_{footing}}{E_{blockout}} + 1\right) \quad (2\text{-}1)$$

$$k_s = \frac{kb_f^3}{24}\left(\frac{E_{footing}}{E_{blockout}} + 1\right) \quad (2\text{-}2)$$

One parameter of interest was the flange effective width for the strong axis orientation. This factor assumed that both flanges bearing against the concrete blockout acted in resisting. Figure 2-5 shows the depiction of the dual flanges resisting against the concrete blockout. Tryon accounted for the two flanges with the term $(2b_f - t_w)$ in Equation (2-1). He incorporated the flange effective width into the equations for base plates rotational stiffness. The flange effective width is not included in Equation (2-2) because the weak axis orientation only has the depth of the column resisting against the concrete blockout.

Figure 2-5: Tryon's model for effective flange width. (Tryon, 2016).

Tryon also accounted for the differing strength in the blockout concrete and the base slab of concrete since these have an effect on the stiffness. This parameter is given in Equation (2-3), which is the average of the two concrete strengths to the blockout modulus. However, the ratio

of the modulus of concretes would cancel out if the strength of the two were equal or close to equal.

$$k_s = \frac{1}{2}\left(\frac{E_{footing}}{E_{blockout}} + 1\right) \tag{2-3}$$

Tryon demonstrated that the rotational stiffness of the base plate was related to the modulus of subgrade reaction. The stiffness of the concrete was determined by the modulus of subgrade reaction multiplied with the depth of the column bearing against the concrete. This meant that for a column loaded in the strong axis direction, the subgrade modulus was multiplied by the flange width and the weak axis was multiplied by the depth of the column.

In addition to the model, Tryon developed curves and simplified equations to go along with the curves that could be used in order to predict rotational stiffness of the spring. Figure 2-6 shows an example of such a curve. The x-axis shows the normalized column length and depth for better comparison. Equation (2-4) shows the simplified equations that Tryon developed in order to represent the rotational stiffness curve.

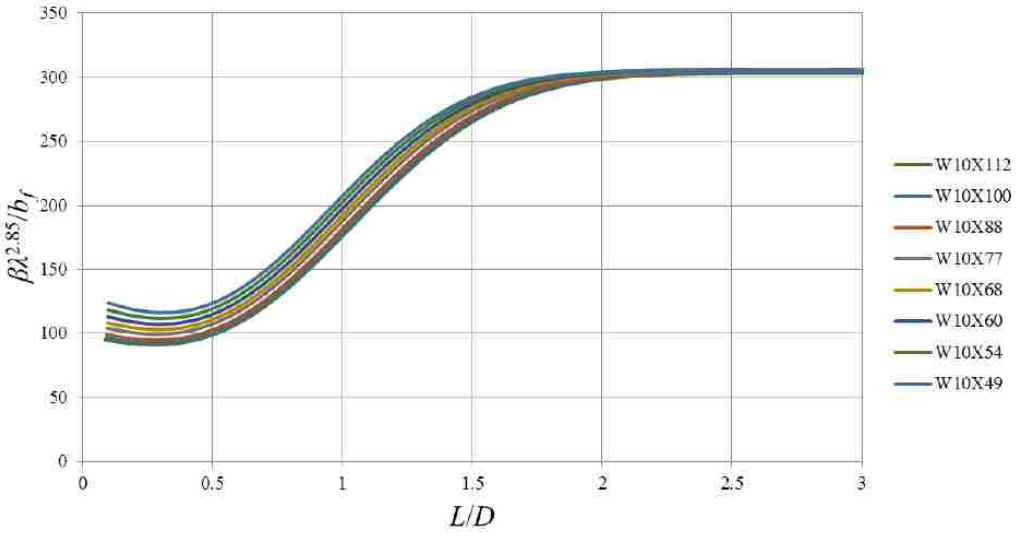

Figure 2-6: Tryon's model for rotational stiffness vs. normalized embedment depth for W10s (Tryon 2016).

$$\frac{\beta\lambda^{2.85}}{b_f} = \begin{cases} 135 & \frac{L}{D} < 0.50 \\ 110 \cdot \frac{L}{D} + 80 & 0.5 \le \frac{L}{D} < 2.0 \\ 300 & 2.0 \le \frac{L}{D} \end{cases} \quad (2\text{-}4)$$

Where:

β = Rotational stiffness at the embedment concrete (kip-in/radians)

b_f = Width of column flange (in)

L = Embedment depth of the column (in)

D = Depth of the column (in)

λ = Factor that incorporates the material properties of both the embedment material and the column material.

$$\sqrt[4]{\frac{k_0(2 \cdot b_f - t_w)}{4 \cdot E \cdot I_x}}$$

k_o = modulus of reaction of the embedment material, assumed to be = 500 kip/in^3

t_w = web thickness of column (in)

E = Modulus of Elasticity of column material = 29000 ksi

I_x = Moment of Inertia of the column about its strong axis (in^4)

2.2.5 Hanks (2016)

Hanks (2016) validated the model proposed by Barnwell (2015) as well as studied the effects of the stiffness of shallow embedded moment frame columns on the ductility of the frame. He constructed eight two-third scale test specimens, which were similar in design to Barnwell's specimens. Hanks' test set up was also quite similar to Barnwell's as shown in Figure 2-7.

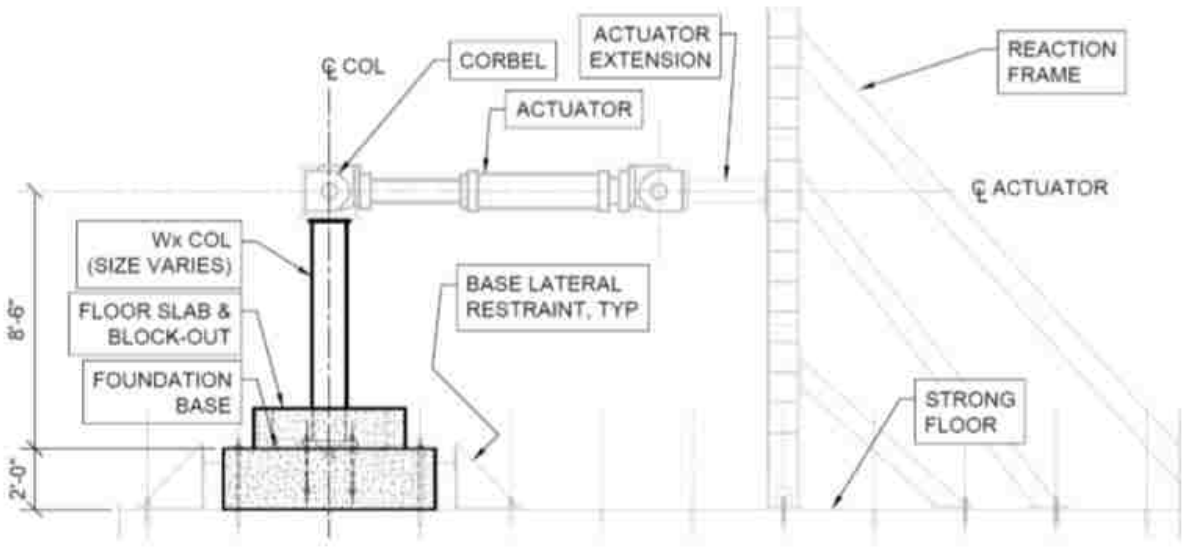

Figure 2-7: Hanks' test set up (Hanks 2016).

The eight specimens were divided into two series of tests; each series being defined by a different column size. The first specimen in each series acted as the control, i.e., specimens with no blockout concrete and only an exposed base plate connection. The second specimen in each series had a blockout with a depth of 8 inches. The third and fourth specimens had blockouts that were 16 inches deep. The difference between the third and fourth specimens in the series was the number of anchor bolts. The full test matrix is shown in Table 2-5. The number of anchor bolts used in each connection was one of the key changes from Barnwell's tests. Additional differences between Hanks' experiment and Barnwell's was the inclusion of a shear tab at the bottom of the base plate as well as larger column sizes.

Table 2-5: Specimen Test Matrix (Hanks 2016)

Specimen Name	Column Size	Base Plate		Shear Lug	Anchor Bolts			Base Depth (in)	Block-out Depth (in)
		Thickness (in)	ASTM grade		Qty	DIA (in)	Grade		
D1	W14x53	2.25	A36	Yes	8	1	F1554 Gr 36	24	0
D2	W14x53	2.25	A36	Yes	8	1	F1554 Gr 36	24	8
D3	W14x53	2.25	A36	Yes	8	1	F1554 Gr 36	24	16
D4	W14x53	1.5	A36	Yes	4	1	F1554 Gr 36	24	16
F1	W10x77	3	A36	Yes	8	1 1/8	F1554 Gr 36	24	0
F2	W10x77	3	A36	Yes	8	1 1/8	F1554 Gr 36	24	8
F3	W10x77	3	A36	Yes	8	1 1/8	F1554 Gr 36	24	16
F4	W10x77	2	A36	Yes	4	1 1/8	F1554 Gr 36	24	16

Hanks' concluded the following:

1. The addition of the blockout concrete provided increased strength to the connection.

2. The currently accepted model, i.e., that developed by Kanvinde et al. (2011) although not meant for embedded columns can be informative for a highly conservative estimate.
3. Rotational stiffness can be modeled as a fixed connection at the top of footing elevation instead of a rotational spring at the top of footing elevation if there was sufficient depth. Although the depth that would prove sufficient is unknown, the embedment depth – column depth ratio should be greater than 1.22.

2.2.6 Grilli and Kanvinde (2017)

Grilli and Kanvinde (2017) investigated the current methods for estimating the strength of Embedded Column Base (ECB) connections as well as developed a new method for strength determination. The method was developed by examining the work by Grilli and Kanvinde (2015), Barnwell (2015), and Cui et al. (2009).

They assumed internal force transfer of horizontal bearing on the column flanges against the concrete panel shear and the vertical bearing on the embedded base plate against the concrete. The proposed method assumed a moment distribution between the horizontal and vertical bearing mechanisms and corresponding stress distribution. The proposed model attempted to balance reliance on mechanics and physics interactions, minimize ad-hoc calibration factors, agree with test data, and simplify equations for design. Figure 2-8 shows the breakdown of the assumed interaction of forces. Equation (2-5) through Equation (2-11) demonstrated how the moment capacity of the connection can be estimated with their model.

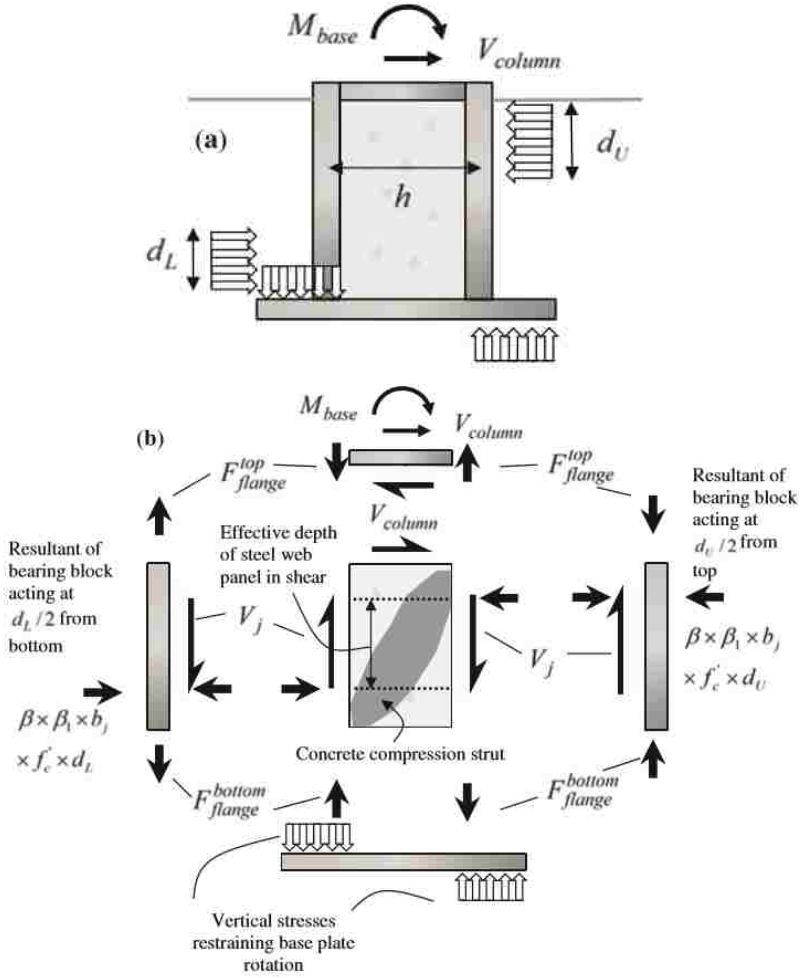

Figure 2-8: Idealization of moment transfer- (a) overall equilibrium and (b) explode detail.

$$M_{HB} = M_{base} - M_{VB} = \left(F_{flange}^{top} - F_{flange}^{bottom}\right) * h = V_j * h \quad (2\text{-}5)$$

$$V_{column} = \beta * \beta_1 * f'_c * (d_U - d_L) * b_j \quad (2\text{-}6)$$

$$M_{HB}^{bearing} = \beta * \beta_1 * f'_c * b_j * \left[d_L * d_{effective} - \frac{(d_L^2 - d_U^2)}{2}\right] \quad (2\text{-}7)$$

$$M_{VB} = \alpha * M_{base} \quad (2\text{-}8)$$

$$M_{HB} = (1 - \alpha) * M_{base} \quad (2\text{-}9)$$

$$\alpha = 1 - \left(d_{embed}/d_{ref}\right) \geq 0 \quad (2\text{-}10)$$

$$M_{base}^{capacity} = M_{HB}^{bearing}/(1 - \alpha) \quad (2\text{-}11)$$

α = Fraction applied moment resisted by the vertical bearing mechanism

β = Factors to account for concrete confinement and the effective bearing

b_j = effective joint width, outer joint panel zone width

d_L = Depth of lower horizontal concrete bearing stress

d_U = Depth of upper horizontal concrete bearing stress

d_{embed}, $d_{effective}$ = Embedment depth

d_{ref} = Depth at which the horizontal bearing stress attenuate to zero.

h = web height of column.

F_{flange}^{top} , F_{flange}^{bottom} = Force in the column flanges at the top and bottom of the embedment zone.

M_{base} = Generic base moment notation.

$M_{base}^{capacity}$ = Base moment capacity as determine by the proposed method.

M_{base}^{max} = Maximum base moment observed by tests.

M_{HB} , M_{VB}= Moment resisted through horizontal or vertical bearing mechanisms.

$M_{HB}^{bearing}$ = Moment capacity provided by horizontal bearing.

P = Axial force in column.

V_j = Vertical shear force in the joint panel.

V_{column} = Imposed column shear.

In order to determine the validity of their results, the maximum moment found during the tests was compared to the moment capacity determined by the method. The proposed strength estimation method was found to give good estimations for the five tests conducted by the authors with an average test ratio of 1.01 in comparison to the current method which gives a ratio of 1.32. The authors warned that the proposed method is limited due to the small pool of data and limited failure modes examined.

2.2.7 Rodas, et al. (2017)

Rodas et al. (2017), presented a model representing the rotational stiffness of the deeply embedded columns. The data used was that of Grilli and Kanvinde (2015). The authors also used data collected from Barnwell (2015) as supplemental data in order to determine how their model transitioned from the deeper embedment to a shallower embedment.

The model decomposed the total rotational stiffness into two parts: deformation from the concrete and deformation from the column due to shear or flexure. These separate deformations are determined by using the theory for beams on elastic foundations. They then attempted to simplify the elements of the model so that it would be more convenient. In order for the stiffness of the system to be determined, the base connection must be designed for strength before their method can be used. This is due to the fact that the model was predominantly developed as a strength method. Good estimations of the rotational stiffness were found for a range of embedment depths. Using all of the test data, the test-predicted ratio was 1.20, if only the data from UC Davis was used, the ratio can be improved to 1.15.

The authors cautioned that the developed model was not as accurate for shallow embedded column connections. Additionally, the model only considered local deformation that was in the vicinity of the embedment. The model also did not consider additional stiffness provided by

reinforcement welded to the column flanges. It should also be noted that this model accounted for axial loads.

3 DATA REDUCTION

3.1 Introduction

Experimental data from two different test series were used in this research. The experiments were conducted by Barnwell (2015) and Hanks (2016), details of testing and setup were given in Sections 2.2.3 and 2.2.5, respectively. In order for these data sets to be comparable, they needed to be processed with the same procedure. This section describes the method for the consistent calculation of the drift, moment at the top of the slab, and the rotational stiffness for each specimen in each of the separate experiments. In addition, the resulting rotational stiffness values for each individual specimen are summarized.

3.2 Generating Hysteretic Plots

Hysteretic plots were created for each specimen in order to understand the behavior of the specimens. The process of generating these plots was implemented in three general steps. The first step was to calculate the moment at the top of the slab. Second was to calculate the total drift. The final step was to generate the hysteretic plots.

The moment at the top of the slab was calculated with the applied load by the actuator and the distance from the top of slab to the line of action of the actuator. The moment was calculated for each time step. The load that was applied was determined by the loading cycle of the experiments. The length of the exposed column was defined as the distance from the top of the

slab to the line of action of the actuator. Table 3-1 and Table 3-2 show the exposed length for each of Barnwell's and Hanks' specimens respectively.

Two additional values are shown in Table 3-1 and Table 3-2; the total blockout depth and the embedment depth. The total blockout depth was the full depth thickness of the main slab or floor slab, which was poured on top of the foundation slab. The embedment depth was defined as the distance from bottom of the base plate to the top of the blockout concrete slab. The embedment depth was closely related to the total blockout depth, since the embedment depth was equivalent to the depth of the blockout minus the layer of grout between the column base plate and the base foundation concrete.

The values listed in Table 3-1 and Table 3-2 were used throughout this thesis. The exposed length was investigated further for its influence on Tryon model in Section 4.2.1. The embedment depth was used in several figures of rotational stiffness versus the embedment depth throughout the thesis in order to evaluate the stiffness models.

The second step for generating hysteric plots was to calculate the total drift of the column. The total drift of the column was determined by the total displacement of the column divided by the exposed length of the column. The displacement of the column was calculated from the string potentiometer measurements. The exposed length are the values listed in Table 3-1 and Table 3-2. The total drift was then calculated for each time step.

The final step was to generate the hysteretic plots. Figure 3-1 shows the hysteretic plots for each of Barnwell's specimens and Figures 3-2 and 3-3 show the hysteretic plots for each Hanks' testing series.

Table 3-1: Barnwell's Experiment Parameters

Specimen	Exposed Length (in)	Total Blockout depth (in)	Embedment Depth (in)
A1	80.375	8	6.5
A2	80.375	8	6.5
A3	80.375	8	6.5
A4	80.375	8	6.5
B1	83.375	16	14.5
B2	83.375	16	14.5
B3	83.375	16	14.5
B4	83.375	16	14.5

Table 3-2: Hanks' Experimental Parameters

Specimen	Exposed Length (in)	Total Blockout depth (in)	Embedment Depth (in)
D1	102	0	0
D2	93	8	7
D3	86	16	15
D4	86	16	15
F1	102	0	0
F2	93	8	7
F3	86	16	15
F4	86	16	15

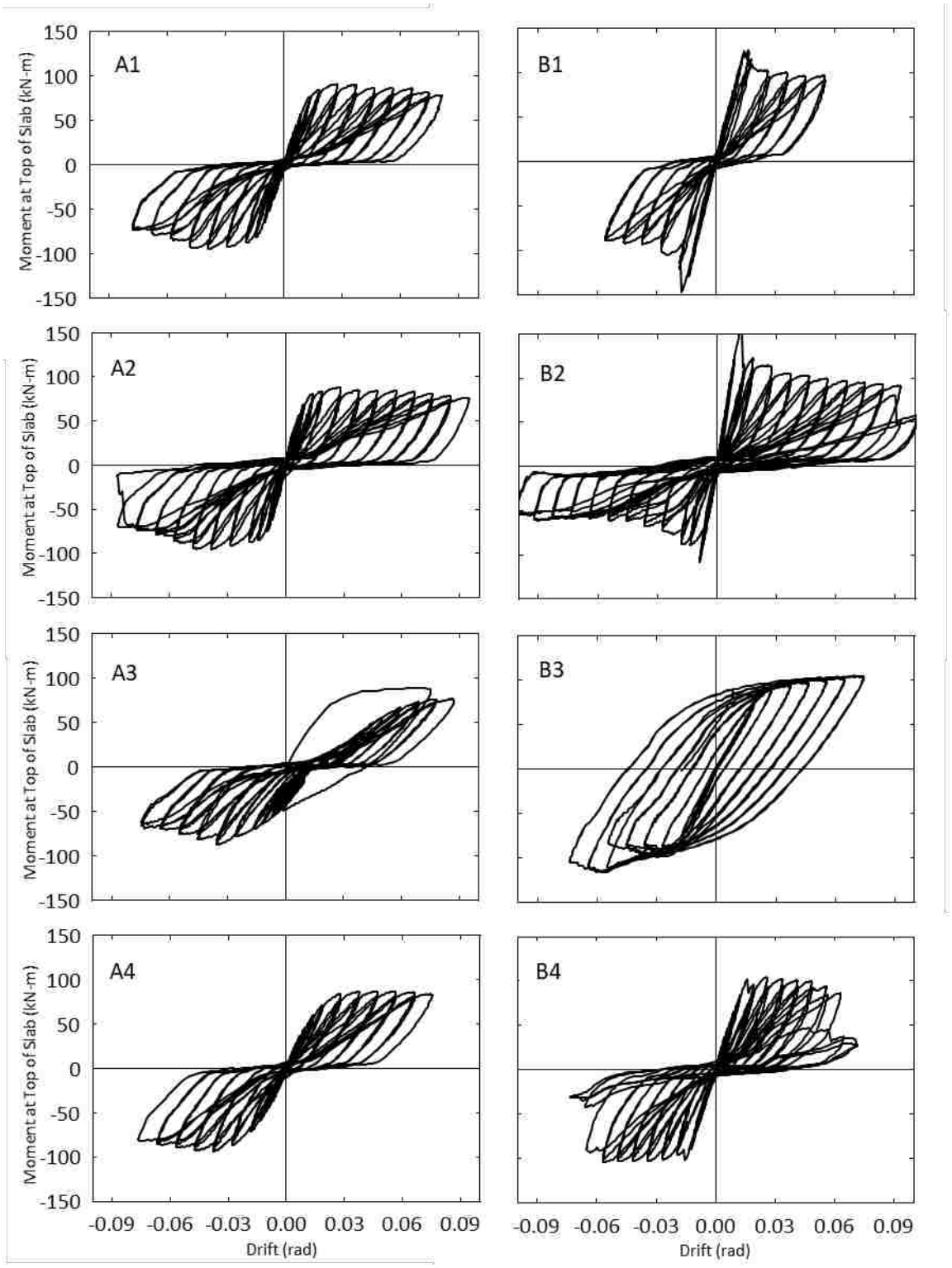

Figure 3-1: Hysteretic plot for Barnwell's specimens.

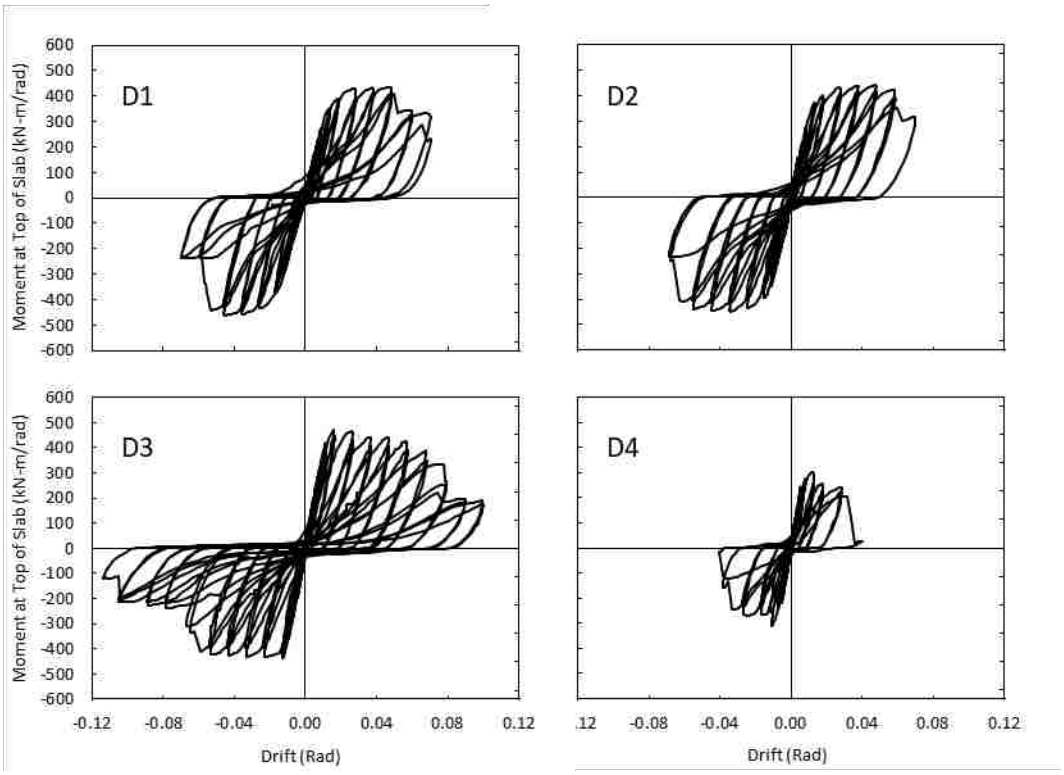

Figure 3-2: Hysteretic plot for Hanks' D- series specimens.

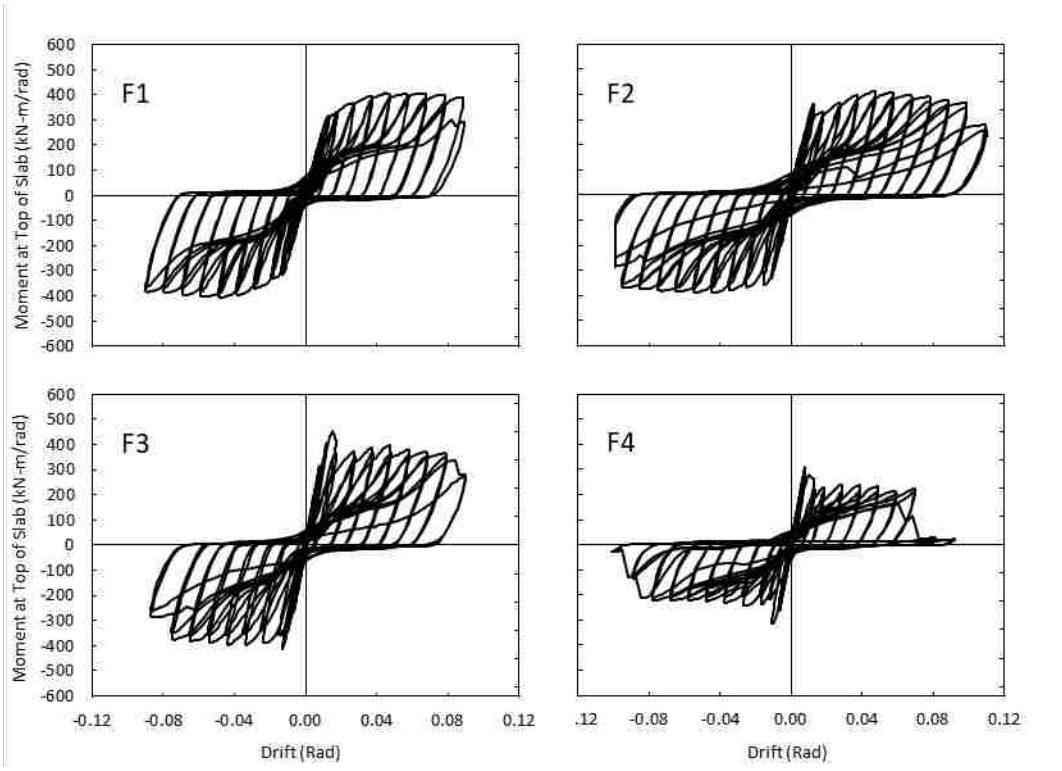

Figure 3-3: Hysteretic plot for Hanks' F-series specimens.

3.3 Calculating Effective Rotational Stiffness

In order to calculate the effective rotational stiffness for each specimen, five steps were implemented. These steps were: first, decompose the displacements of the column; second, calculate the effective rotation of the connection; third, generate the backbone curves; fourth, determine the intersection of the backbone with particular drift values; and fifth, find the slope of the line representing the rotational stiffness.

The first step in calculating the rotational stiffness was to decompose the displacements of the column. The total displacement of the column was made up of two components: the displacement from the exposed column and the displacement from the base connection. The total displacement was determined directly from the experimental testing, this was the same value as was used in Section 3.2. The total displacement is defined as Equation (3-1). The deflection from the column is simply the elastic deformation of a single column, which is represented by the Equation (3-2). The parameters were F, the applied force; L, the distance from the top of the slab to the line of action of the actuator or the exposed column length; E, Young's modulus; and I, the moment of inertia. The deformation from the connection was determined from these two equations as shown in Equation (3-3). This decomposition is only valid as long as the column stays in the elastic region; therefore, Young's modulus stays constant.

$$\delta_{total} = \delta_{column} + \delta_{connection} \tag{3-1}$$

$$\delta_{column} = \frac{FL^3}{3EI} \tag{3-2}$$

$$\delta_{connection} = \delta_{total} - \frac{FL^3}{3EI} \quad (3\text{-}3)$$

With the column displacement decomposed, the effective base rotation was determined by using the displacement of column from only the connection, Equation (3-3). The effective rotation was found by dividing the displacement due to the connection by the column exposed length given in Tables 3-1 and 3-2.

The third step in the process of calculating the effective rotational stiffness was to generate the backbone curve for each specimen. The backbone curve is the plot of the effective base rotation, which was found in the previous step and plotting it against the moment at the top of the slab, which was found in Section 3.2. The difference was that not all of the moment data was used, only the maximum values per cycle or the backbone points.

The fourth step was to identify points corresponding to particular drift values. This was done by finding the intersection of the backbone curve with a particular value of drift or the effective base rotation. Values of 0.004 and 0.005 effective base rotation were used as reasonable estimates. The 0.4 percent drift and the 0.5 percent drift were essentially averages of the higher stiffness at lower percentages and the reduced stiffness at later percentages. The drift values chosen were the same for all specimens. The drift was linearly interpolated from the available data points of the backbone curve.

The final step was to find the slope of the line between the two drift points. This slope value was the estimated effective rotational stiffness. A typical plot is shown in Figure 3-4. The A2 line represents the backbone curve and the two dashed lines are the estimated effective rotational stiffness for two assumed drift values.

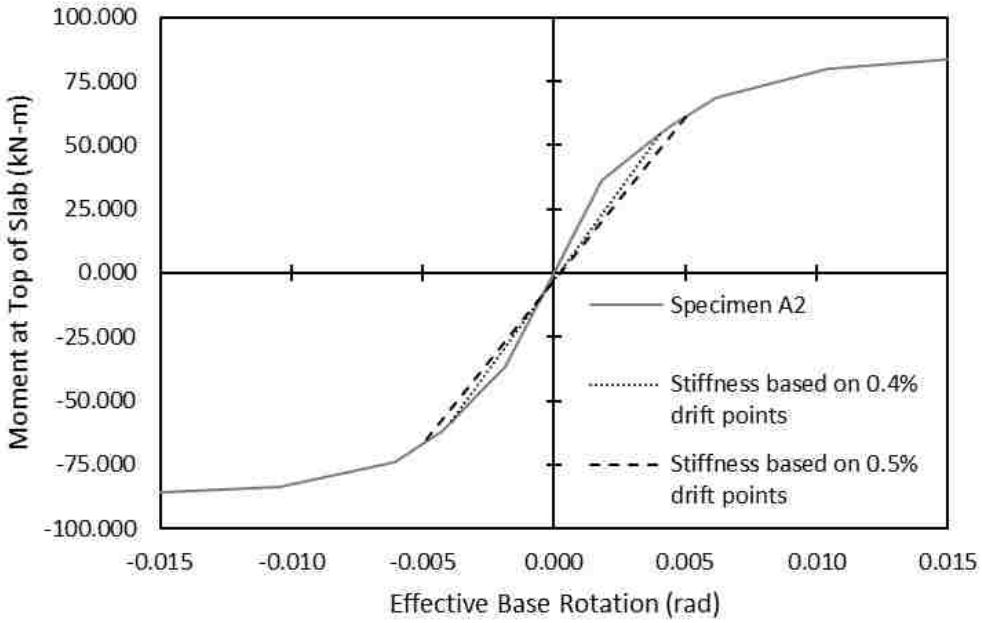

Figure 3-4: Specimen A2 rotational stiffness calculation.

3.4 Results

Figure 3-5 through Figure 3-20 show the plots for each specimen in the Barnwell's and Hanks' test with the moment at the top of the slab versus the effective base rotation. Barnwell's series A are presented in Figure 3-5 through Figure 3-8 and Figure 3-9 through Figure 3-12 are for Barnwell's series B. Figure 3-13 through Figure 3-16 are for Hanks' series D and Hanks' series F is as shown in Figure 3-17 through Figure 3-20.

The rotational stiffness values were calculated based on the slope of the line through the 0.5 percent story drift points in Figure 3-5 through Figure 3-20. The rotational stiffness values obtained are listed in Table 3-3 for Barnwell's specimens and in Table 3-4 for Hanks' specimens. Note that in Table 3-3 specimen B3 and B4 did not have a value for the rotational stiffness. This was because the general method was not reliable for these specimens since they had flexible columns and limited connection deformation before column yielding. Additionally, the method for decomposing the drift may not be valid in these cases.

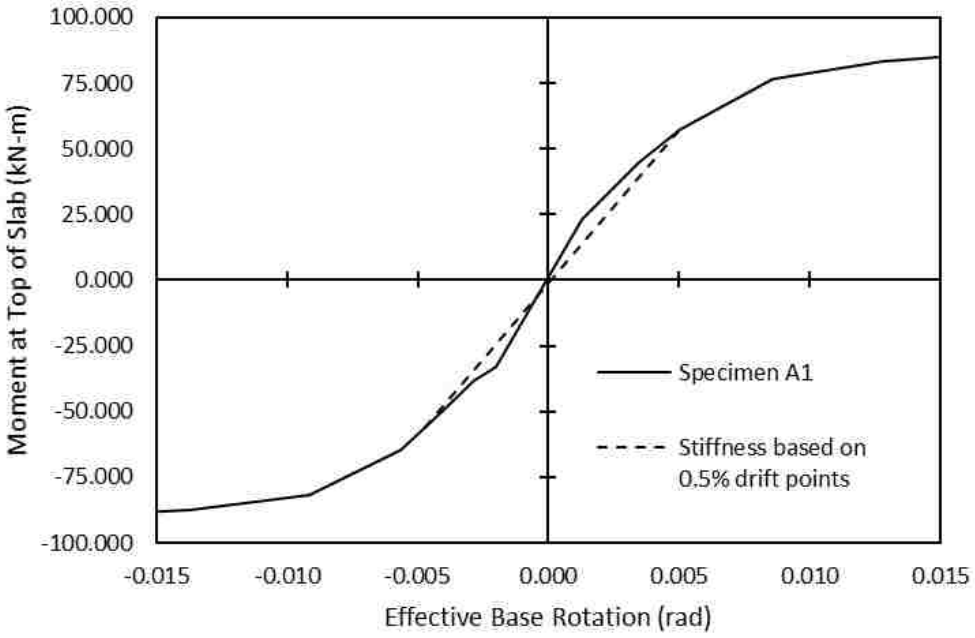

Figure 3-5: Specimen A1 moment at top of slab versus effective base rotation. (W8x35 Strong – 6.5 inches embedment depth).

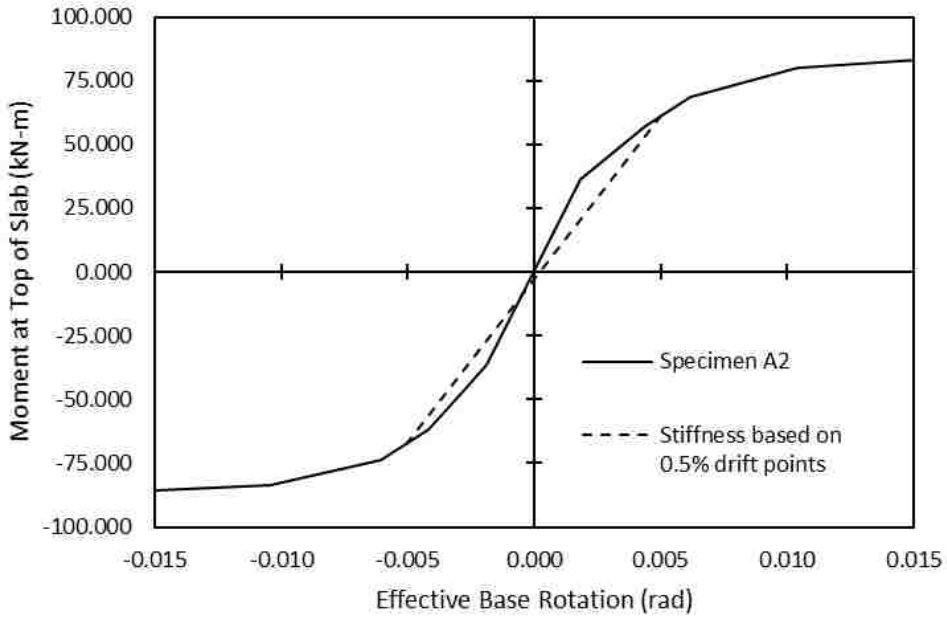

Figure 3-6: Specimen A2 moment at top of slab versus effective base rotation (W8x48 Strong – 6.5 inches embedment depth).

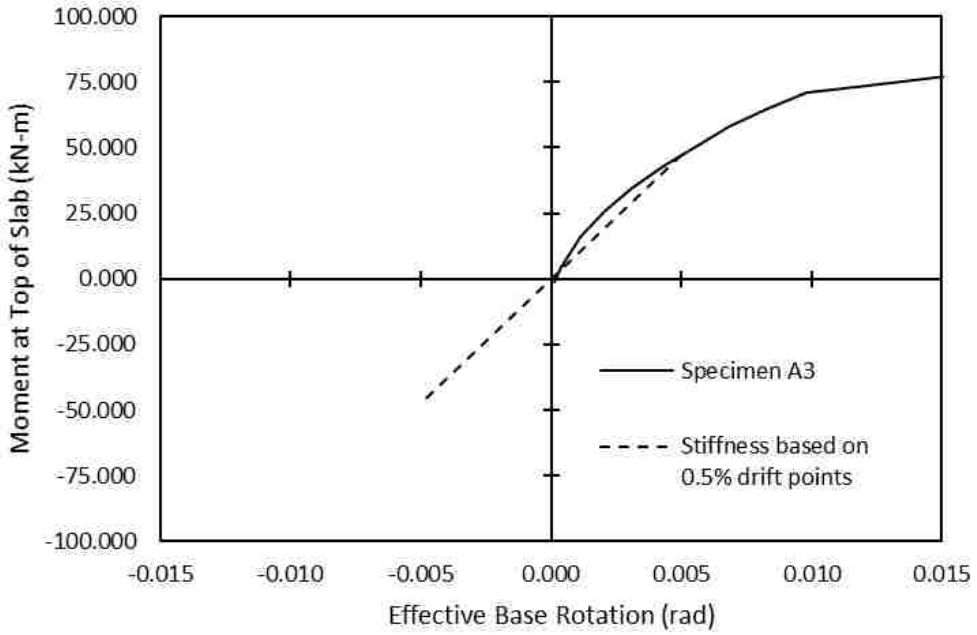

Figure 3-7: Specimen A3 moment at top of slab versus effective base rotation (W8x35 Weak – 6.5 inches embedment depth).

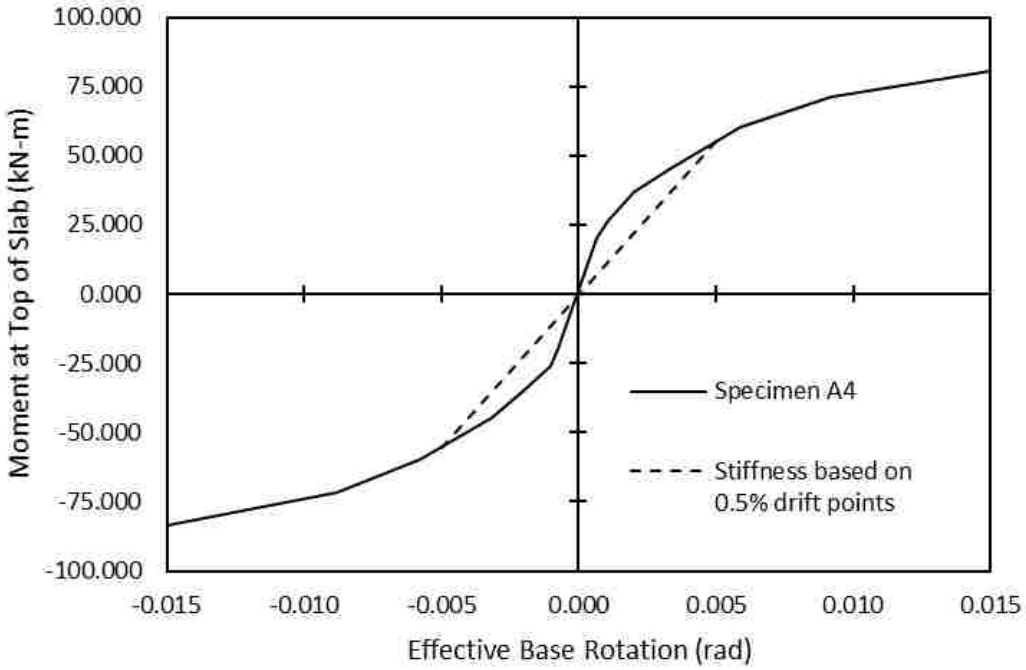

Figure 3-8: Specimen A4 moment at top of slab versus effective base rotation (W8x48 Weak – 6.5 inches embedment depth).

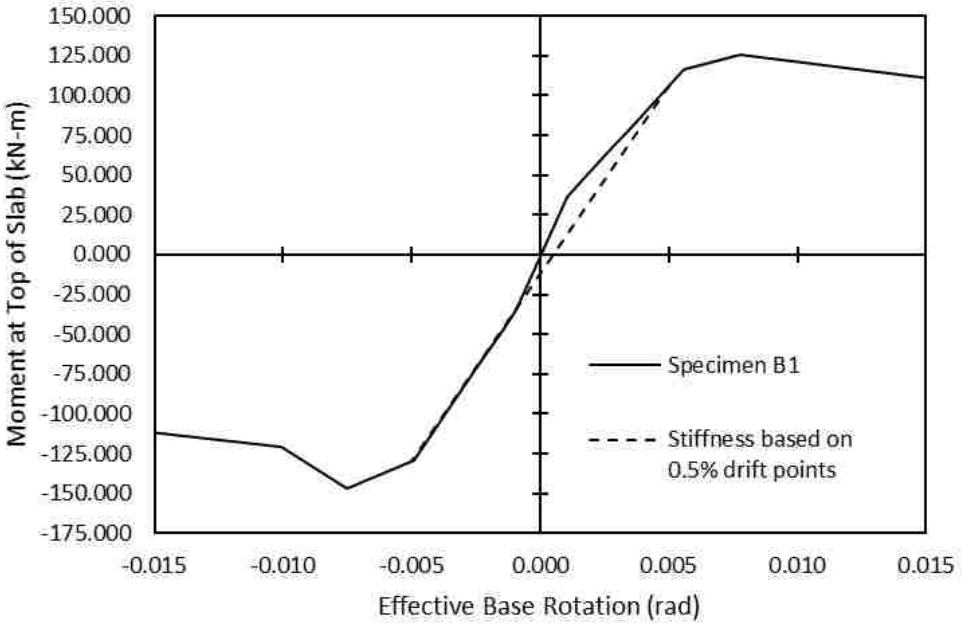

Figure 3-9: Specimen B1 moment at top of slab versus effective base rotation (W8x35 Strong – 14.5 inches embedment depth).

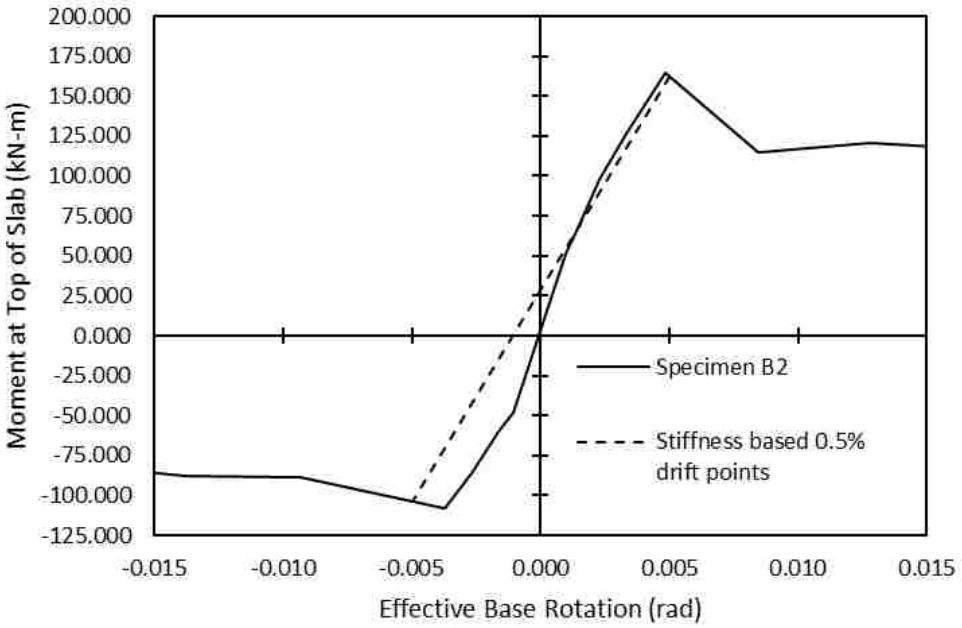

Figure 3-10: Specimen B2 moment at top of slab versus effective base rotation (W8x48 Strong – 14.5 inches embedment depth).

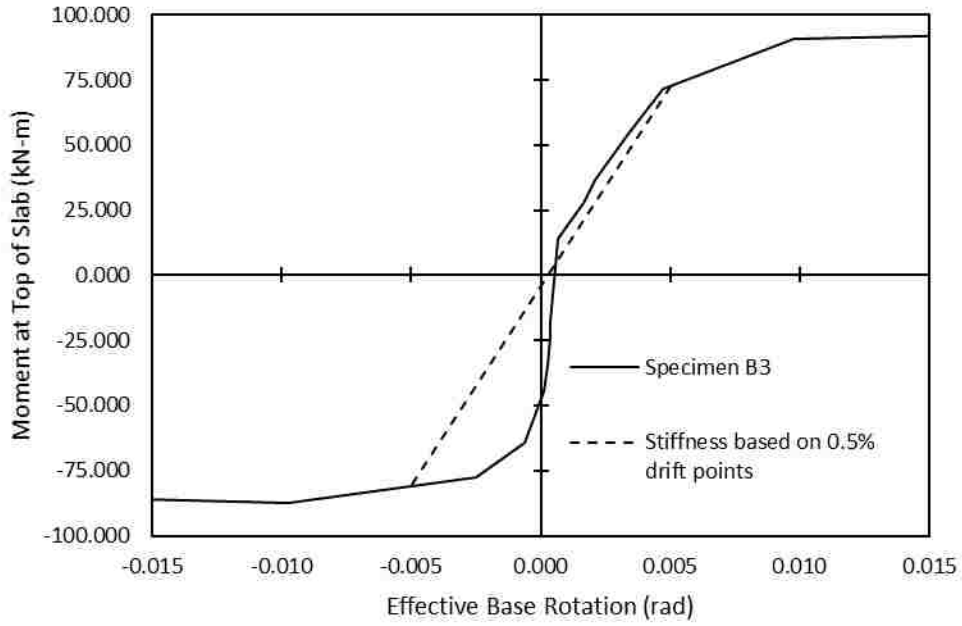

Figure 3-11: Specimen B3 moment at top of slab versus effective base rotation (W8x35 Weak – 14.5 inches embedment depth).

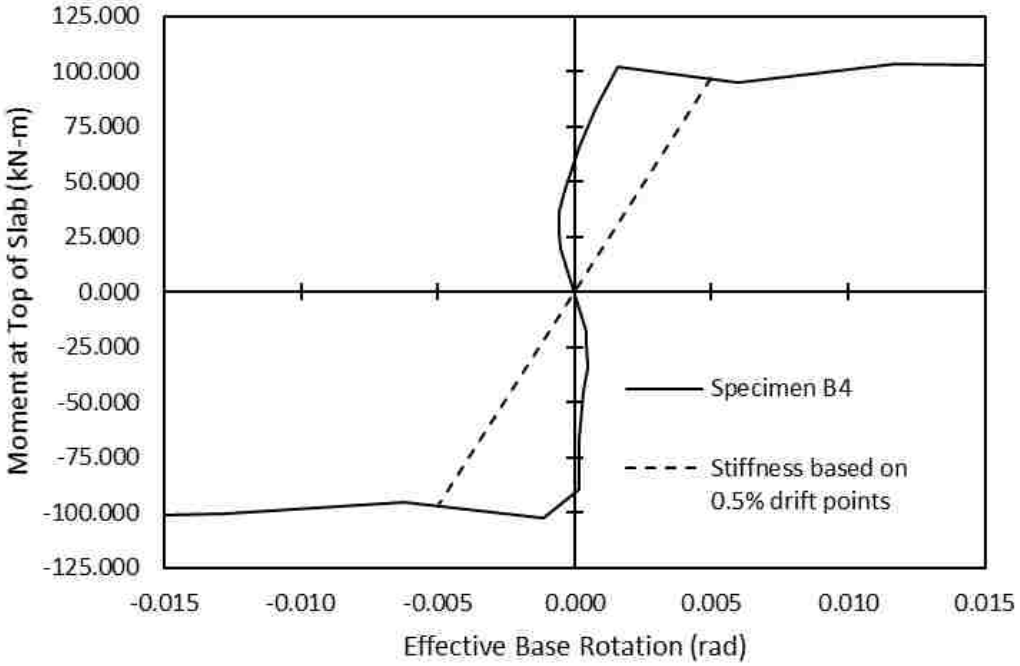

Figure 3-12: Specimen B4 moment at top of slab versus effective base rotation (W8x48 Weak – 14.5 inches embedment depth).

Hanks D Series

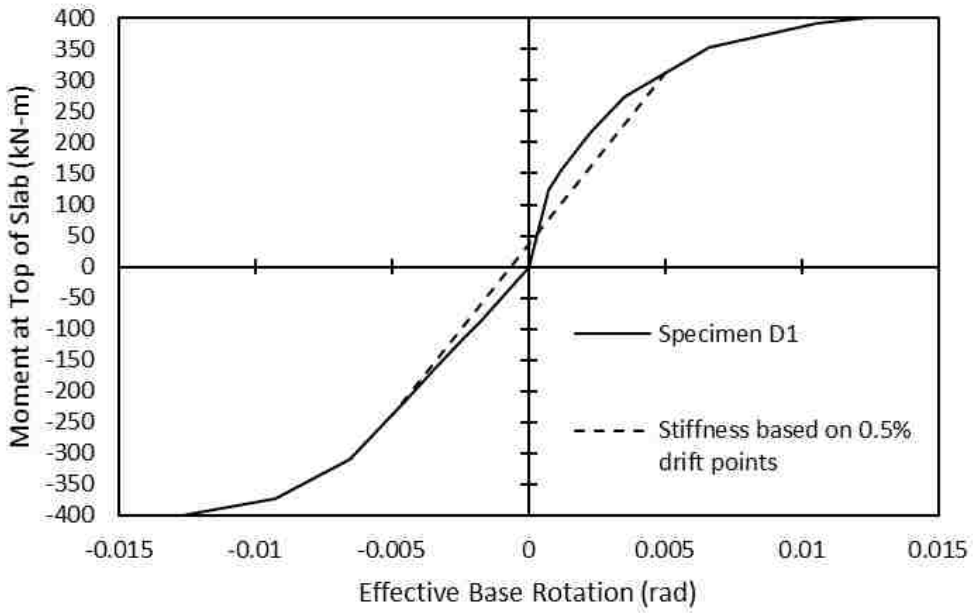

Figure 3-13: Specimen D1 moment at top of slab versus effective base rotation (W14x35 Strong – 0 inches embedment depth).

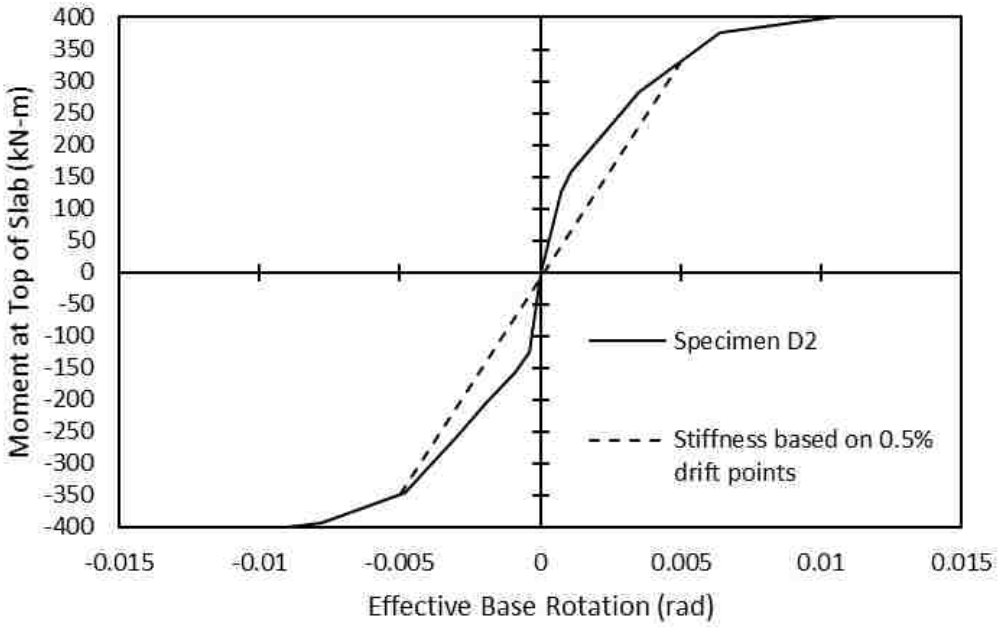

Figure 3-14: Specimen D2 moment at top of slab versus effective base rotation (W14x35 Strong – 7 inches embedment depth).

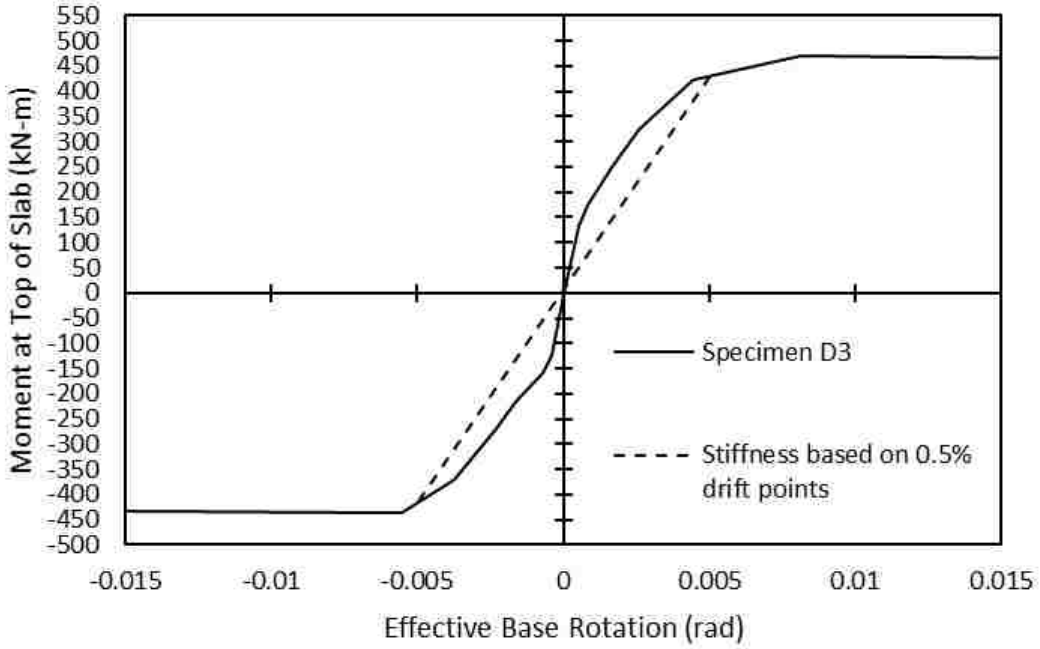

Figure 3-15: Specimen D3 moment at top of slab versus effective base rotation (W14x35 Strong – 15 inches embedment depth).

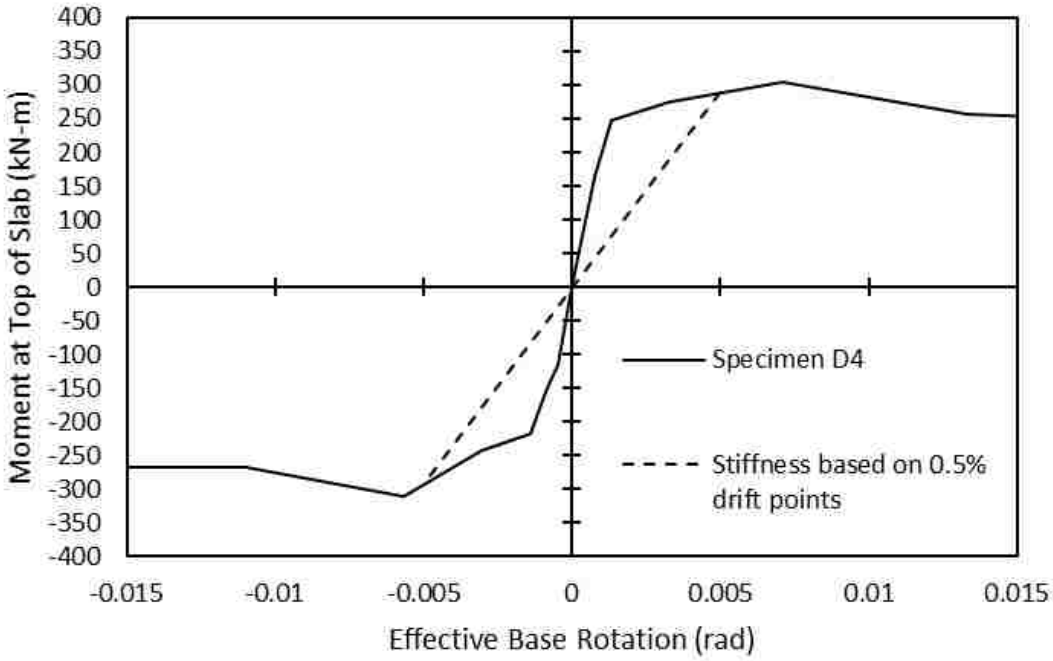

Figure 3-16: Specimen D4 moment at top of slab versus effective base rotation (W14x35 Strong – 15 inches embedment depth).

Hanks F Series

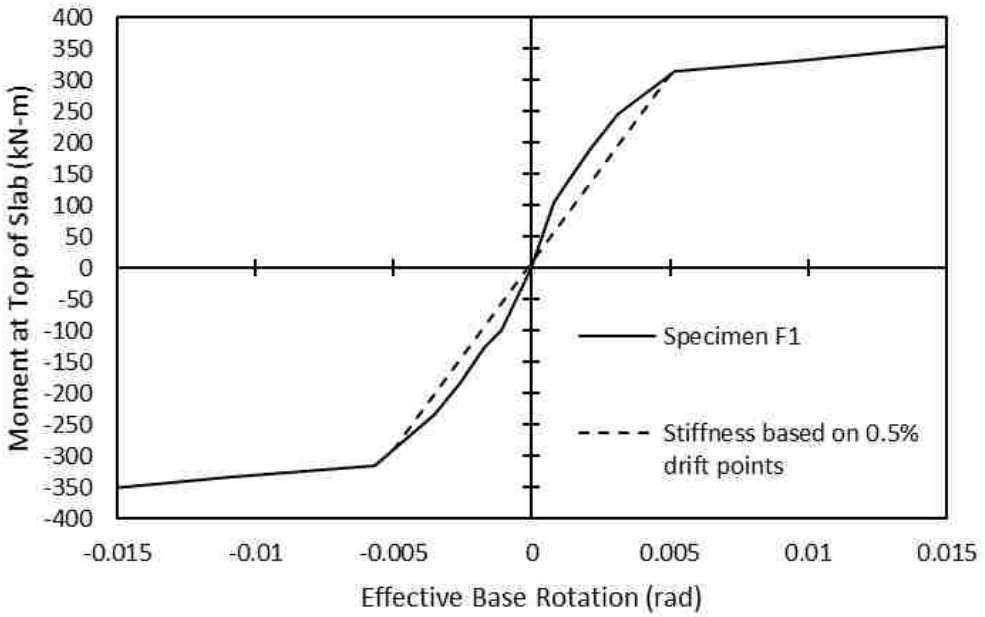

Figure 3-17: Specimen F1 moment at top of slab versus effective base rotation (W10x77 Strong – 0 inches embedment depth).

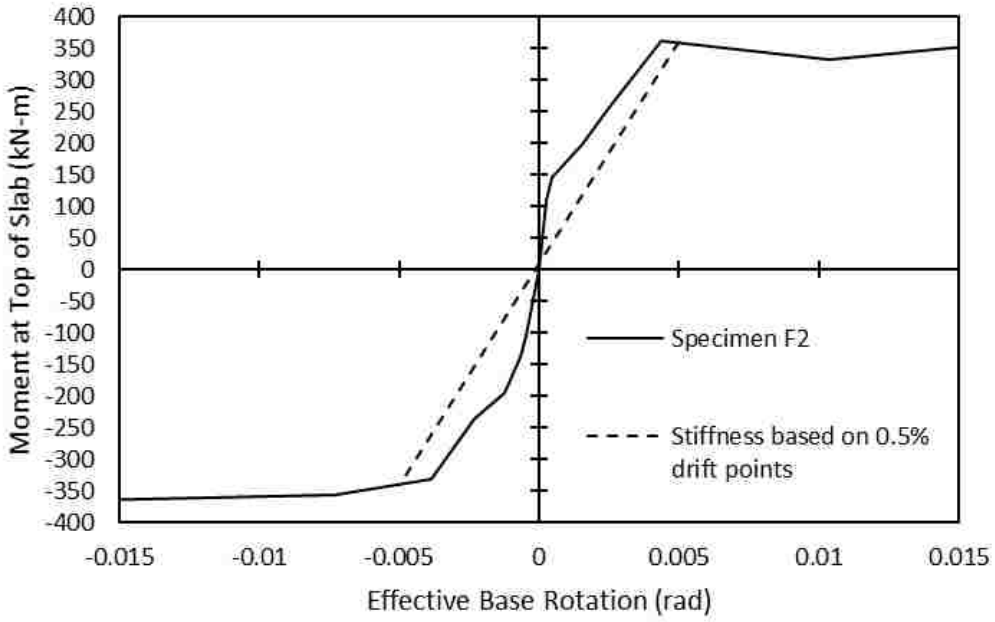

Figure 3-18: Specimen F2 moment at top of slab versus effective base rotation (W10x77 Strong – 7 inches embedment depth).

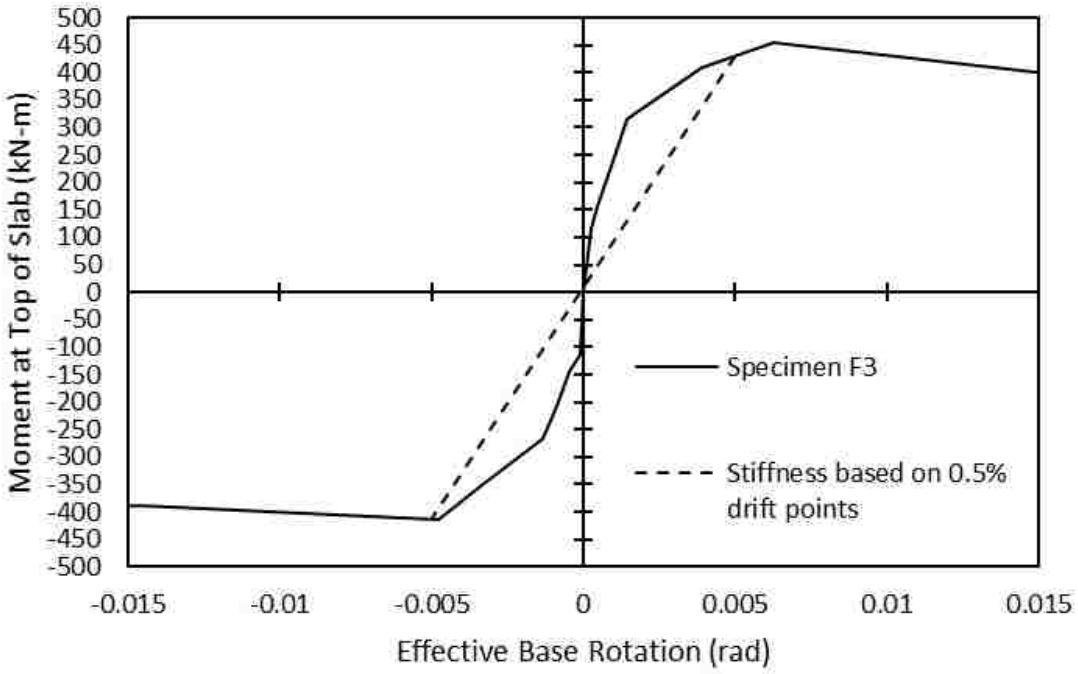

Figure 3-19: Specimen F3 moment at top of slab versus effective base rotation (W10x77 Strong – 15 inches embedment depth).

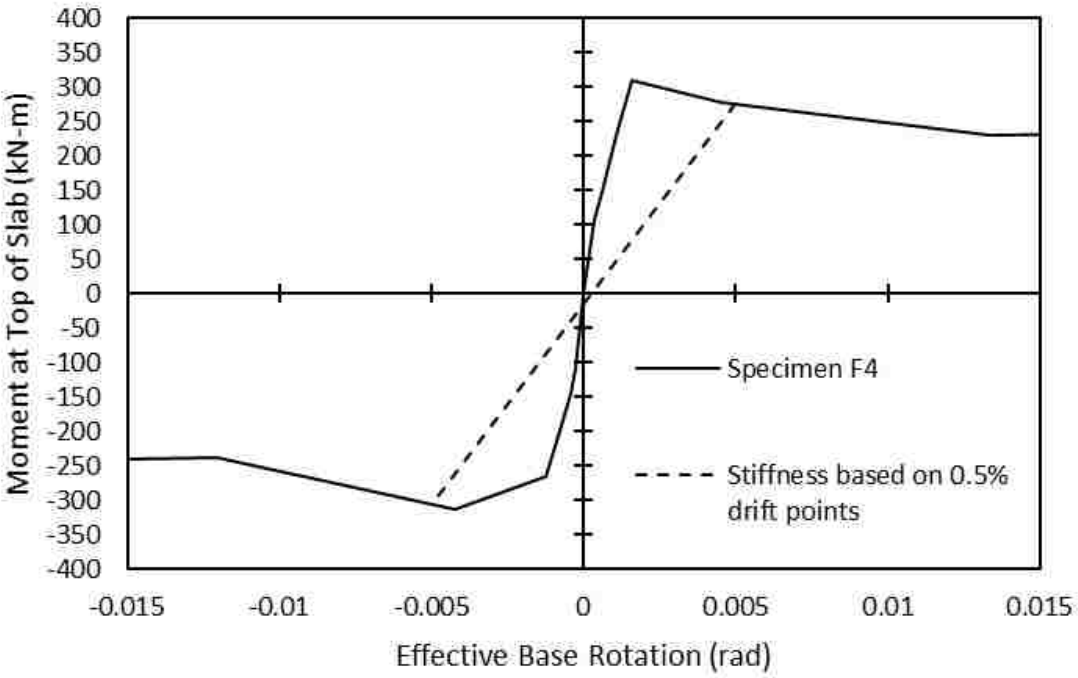

Figure 3-20: Specimen F4 moment at top of slab versus effective base rotation (W10x77 Strong – 15 inches embedment depth).

Table 3-3: Rotational Stiffness Values from Barnwell's Experiments

Specimens	Rotational Stiffness @ 0.5% Drift (kN-m/rad)	Rotational Stiffness @ 0.4% Drift (kN-m/rad)
A1	11567	12318
A2	12806	14212
A3	9470	10241
A4	11027	12353
B1	23587	24429
B2	26599	31392
B3	N/A	N/A
B4	N/A	N/A

Table 3-4: Rotational Stiffness Values from Hanks' Experiments

Specimens	Rotational Stiffness @ 0.5% Drift (kN-m/rad)	Rotational Stiffness @ 0.4% Drift (kN-m/rad)
D1	55145	59872
D2	68074	75914
D3	84606	97305
D4	58121	68416
F1	59811	65850
F2	69844	83928
F3	84239	98660
F4	58193	74185

3.5 Summary

Data reduction was necessary in order to ensure that similar values were being compared. The values determined in this section were the values that were used for analysis in the rest of the thesis. Although the rotational stiffness values seen in this section were approximations for the 0.5 percent story drift, any value of percent drift can be calculated and used in a similar

manner. The 0.5 percent story drift was chosen, because it was an average of the higher stiffness at lower story drift values and the lower stiffness at higher story drift values. However, as shown in Figure 3-5 through Figure 3-20, the 0.5 percent story drift was not always the best approximation.

The values presented in this section were slightly different from those that were presented in Tryon's or Hanks' theses, Barnwell did not present rotational stiffness values in his thesis. The values in Table 3-3 were about two times smaller than the values reported by Tryon for Barnwell's testing and the valued in Table 3-4 were also smaller than those reported in Hanks' thesis. Values from Table 3-4 were between 15% but less than 50% of Hanks' reported values, because both Hanks and Tryon used different percent story drifts than the value used in this thesis. In addition, the stiffness was calculated with small differences in the embedment depth and exposed length.

4 MODIFIED TRYON MODEL

4.1 Introduction

With the data reduction complete, the experimental data was compared with the results from Tryon's model. Tryon's model was investigated in order to determine the parameters that were significant. Each parameter was either added directly without modifications into a new version of Tryon's model or the parameter were altered for a better fit of the data before being added into the model.

The main parameters in Tryon's continuum model are embedment depth, exposed length, flange effective width, modulus of subgrade reaction, and base plate rotational stiffness, k_s, as stated in Section 2.2.4. The embedment depth was discussed in Section 3.2. The exposed length was introduced in Section 3.2 and is discussed further in Section 4.2.1. The flange effective width and modulus of subgrade reaction are influential components to the rotational stiffness equations and are discussed in Sections 4.2.2 and 4.2.3, respectively.

Results are shown in Section 4.3 for the relationship between the rotational stiffness that was determined in Section 3.4 and the model with the modified parameters.

4.2 Influence of Various Parameters in Tryon's Model

4.2.1 Effects of Exposed Lengths

The sensitivity of the resulting model for a single exposed length, when the column size and orientation match, was investigated. Since Barnwell's specimens had two different exposed lengths, the sensitivity of the model to this parameter was investigated. For Barnwell's tests, there was an exposed length of 80.375 inches for specimens with an 8-inch blockout depth and 83.375 inches for the specimens with a 16-inch blockout depth. It was believed that the 3-inch difference would not cause a significant change in the response of Tryon's model. Figure 4-1 shows the difference in the rotational stiffness as predicted by Tryon's model for the two different exposed lengths from Barnwell's data if all other parameters were held constant. The small difference in exposed length did not have much impact on the results from Tryon's model. Thus, an exposed length of 83.375 inches was assumed for comparison with Tryon's model in other parameter studies. The exposed length of 83.375 inches was used in Tryon's model to calculate the moment, which was in turn used to estimate the total rotation and displacement of the column.

Hanks', specimen D2 and F2 had an exposed length of 93 inches and specimen D3, D4, F3, and F4 had an exposed length of 86 inches. Specimens D1 and F1 did not have a blockout, so their exposed length was 102 inches. Even though there was a greater difference between the three exposed lengths for Hanks' data, it was still believed that the difference in exposed length was small enough that there would not be significant difference in the response of Tryon's model. Figure 4-2 shows the comparison of the three lengths with similar parameter assumptions. Since there was an insignificant difference in the response of the model, a single value of 86 inches was assumed for the exposed length for Hanks' experiments in other

parameter studies. The single value chosen for Hanks' data as well as Barnwell's data would be used to generate the curves shown throughout the remainder of this thesis. The exposed length was an important parameter in calculating the moment induced on the specimen.

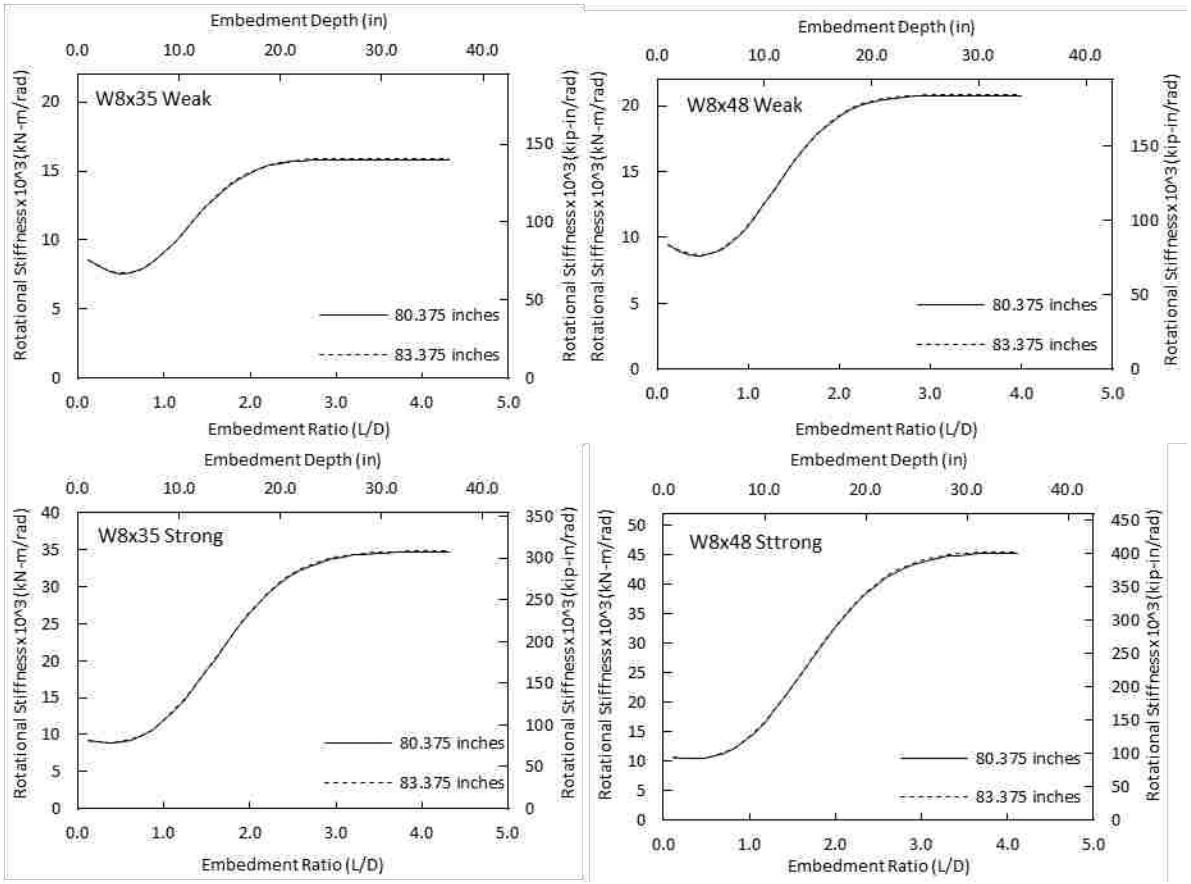

Figure 4-1: Exposed length comparison for Barnwell's experiments (k_o = 150kip/in^3).

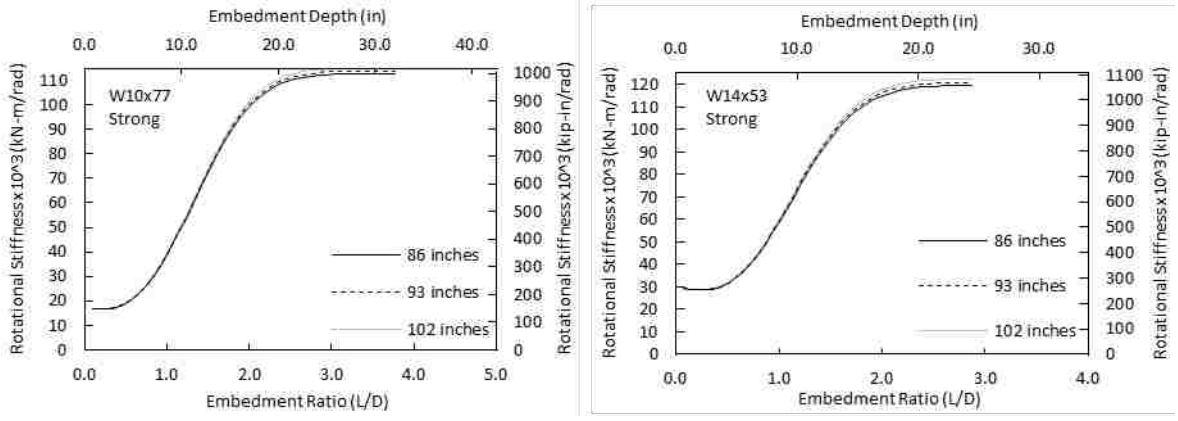

Figure 4-2: Exposed length comparison for Hanks' experiments (k_o = 150kip/in^3).

4.2.2 Effects of Flange Effective Width

A further assumption that was evaluated for Tryon's model was flange effective width, which Tryon called flange duality and the effective width of the column. As was discussed in Section 2.2.4, Tryon assumed that both flanges would act in resisting against the blockout concrete. In order to check the flange effective width, curves were generated using Tryon's model, one with the assumption of both flanges resisting and another accounting for only one of the flanges resisting against the blockout concrete. Barnwell's experimental data was then compared to the two curves to determine the best fit. The affected parameter was mainly the spring rotational stiffness; however, Tryon's calculations for the modulus of subgrade reaction was also affected.

The flange effective width was then removed from Equation (2-1) and Equation (2-2) which became Equation (4-1) and Equation (4-2), respectively. Notice that Equation (4-2) does not change since this was for the weak orientation of the column and therefore the two flanges were not acting in resistance. The variable k in theses equations represents the concrete stiffness and was determined by the modulus of subgrade reaction multiplied by the depth of the flanges if strong axis and the depth of the column if the weak axis was used.

$$k_s = \frac{kd^3}{24}\left(\frac{E_{footing}}{E_{blockout}} + 1\right) \quad (4\text{-}1)$$

$$k_s = \frac{kb_f^3}{24}\left(\frac{E_{footing}}{E_{blockout}} + 1\right) \quad (4\text{-}2)$$

The results of the flange effective width analysis are shown in Figure 4-3 for Barnwell's strong axis specimens and in Figure 4-4 for Hanks' specimens. The dashed line in these figures

represents the equation for excluding flange effective width and is label as “Excluded”. The solid line is the original response of the model, which includes the flange effective width and is labeled as “Included.” Only the strong column orientations are shown, since the weak axis orientation does not change as already noted. The modulus of subgrade reaction that was used for all of the figures are k_o = 150 kips/in^3. The modulus of the concrete that was used differed: for Barnwell $E_{footing}$ = 3600 ksi and $E_{blockout}$ = 2280 ksi; and for Hanks $E_{footing}$ = 3600 ksi and $E_{blockout}$ = 3600 ksi. These values were estimated from the information obtained from cylinders tests.

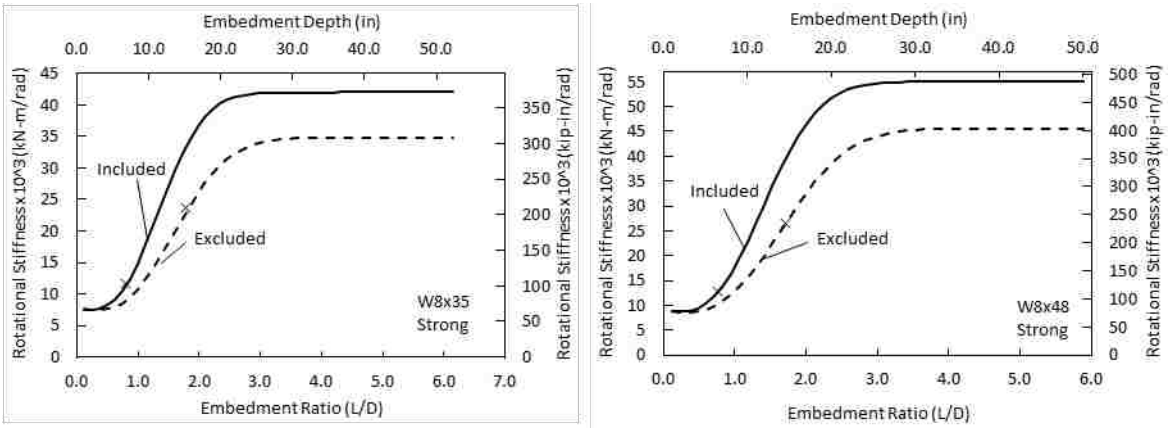

Figure 4-3: Flange effective width comparison of Barnwell's strong axis specimens (k_o = 150kip/in^3).

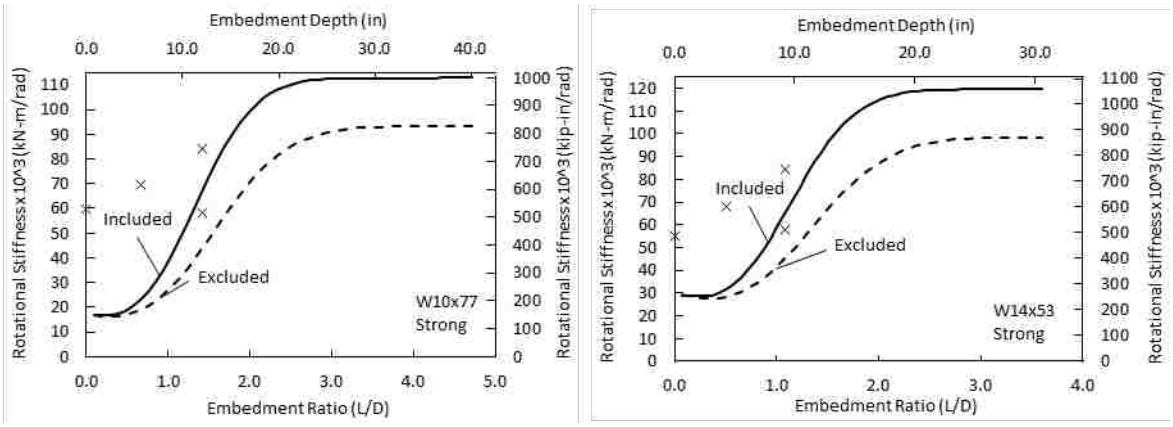

Figure 4-4: Flange effective width comparison of Hanks' specimens (k_o = 150kip/in^3).

Figure 4-3 shows that Barnwell's data fits better with flange effective width excluded; however, Figure 4-4 suggests that Hanks' data may fit slightly better with flange effective width included. Although there are too few points to say definitively which way is better. However, the flange effective width was removed for later parameter investigation, since there appeared to not be an extreme change between the two curves and Hanks' data in some cases seems to fit better with the excluded flange effective width.

4.2.3 Effects of Concrete Modulus

The next parameter that was evaluated was the effect of the concrete modulus ratio on the spring stiffness, k_s. If the flange effective width was excluded like what was discussed above, then the equation for k_s would become Equation (4-3), note this is the same equation as Equation (4-1), it was repeated for easier comparison. Two variations of the equation were investigated. The variations that were compared are shown in Equations (4-4) and (4-5). Equation (4-4) removes the assumption, $\frac{1}{2}\left(\frac{E_{footing}}{E_{blockout}}+1\right)$, and assumes that k_s was only a function of the modulus of the footing over the blockout and not an average of the two strengths. Equation (4-5) removes any effect from the concrete and tests for an adjustment factor instead. An adjustment factor of 2 was used for both Barnwell's and Hanks' data. Figure 4-5 shows the equations compared with Barnwell's data. Figure 4-6 shows the comparison of Hanks' data compared to the equations discussed.

$$k_s = \frac{kd^3}{24}\left(\frac{E_{footing}}{E_{blockout}} + 1\right) \quad (4\text{-}3)$$

$$k_s = \frac{kd^3}{12}\left(\frac{E_{footing}}{E_{blockout}}\right) \quad (4\text{-}4)$$

$$k_s = \frac{kd^3}{12}(adjustment) \quad (4\text{-}5)$$

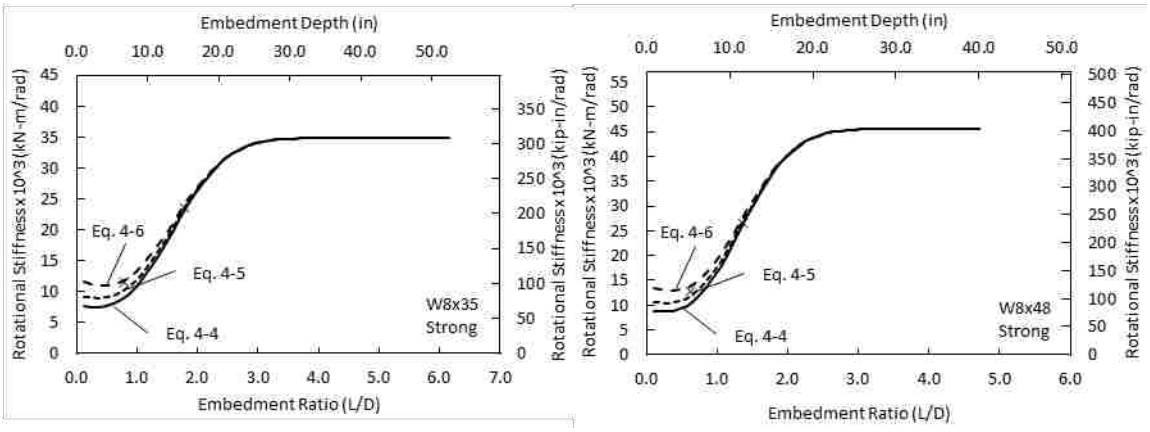

Figure 4-5: Barnwell's experiments compared to differing equations of the base plate rotational stiffness, k_s (k_o = 150kip/in^3).

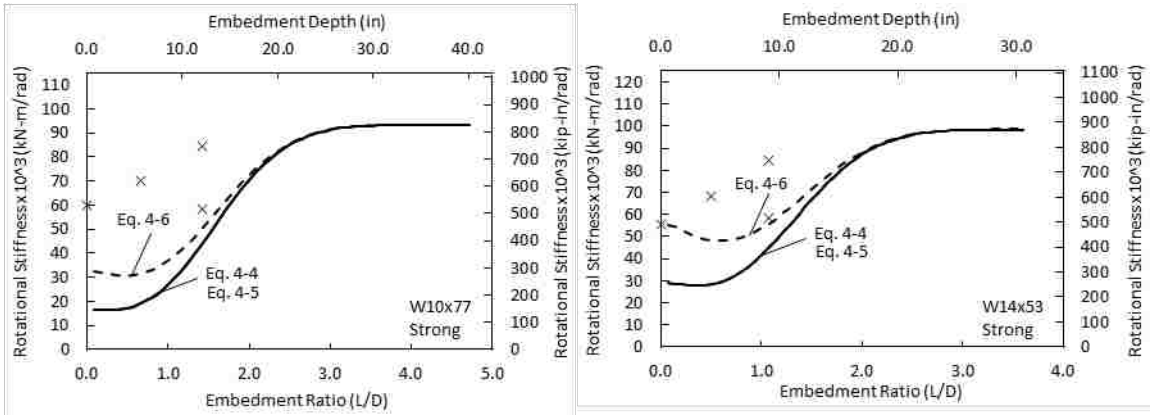

Figure 4-6: Hanks' experiments compared to differing equations of the base plate rotational stiffness, k_s, (k_o = 150kip/in^3).

Figure 4-5 shows that Barnwell's data fits fairly well with any of the equations, since Barnwell did not test any exposed base connection columns. Figure 4-6 suggests that a different modulus of subgrade reaction may be required or an additional change in a parameter. These equations will be evaluated further in the Section 4.3 on combined effects.

4.3 Combined Effects

4.3.1 Barnwell's Data

Figure 4-7 shows the relationship between Barnwell's data and Tryon's model. Tryon's model was updated with the assumptions that were described in the preceding subsections. The curves were generated using Equation (4-4) for two different shapes in the strong and weak axis direction, with a variety of values for the modulus of subgrade reaction, 100 kip/in^3, 150 kip/in^3, and 200 kip/in^3. The "xs" in the figure correlate to the stiffness calculated at 0.5 percent story drift. The results show that Tryon's model is sensitive to the modulus of subgrade reaction value assumed, as well as the way the stiffness was calculated for the specimen. The best fit for this strong axis loading is with k_o = 150 kip/in^3.

The best fit values for Tryon's model for the weak axis orientation was a little more difficult to determine since only one data point for each shape and orientation combination was available. The best approximation for k_o for the weak axis loading is 200 kip/in^3. The lack of experimental results was due to some errors during testing that did not allow for the actual stiffness to be calculated for comparison.

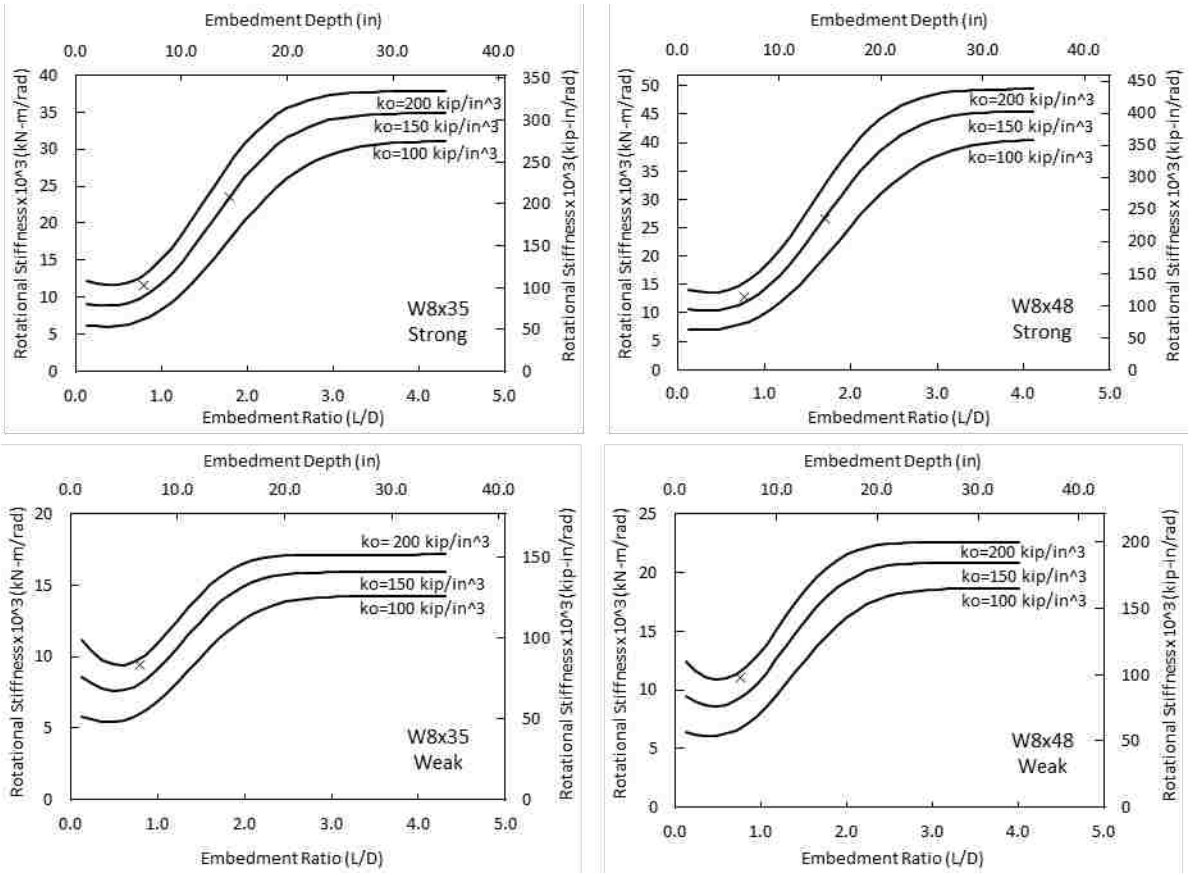

Figure 4-7: Barnwell's experiments compared to Tryon's model using Equation 4-5. The concrete footing modulus used was 3600 ksi and the concrete blockout modulus used was 2280 ksi.

4.3.2 Hanks' Data

Figure 4-8 shows the relationship between Hanks' data and the updated version of Tryon's model with the use of Equation (4-4) for the formula of k_s. It should be remembered that Hanks' testing did not include the weak orientation. The results show the model under predicts Hanks' data points. Therefore, it was determined that a larger modulus of subgrade reaction value was needed. Additional values for the modulus of subgrade reaction were evaluated and the results are shown in Figure 4-9.

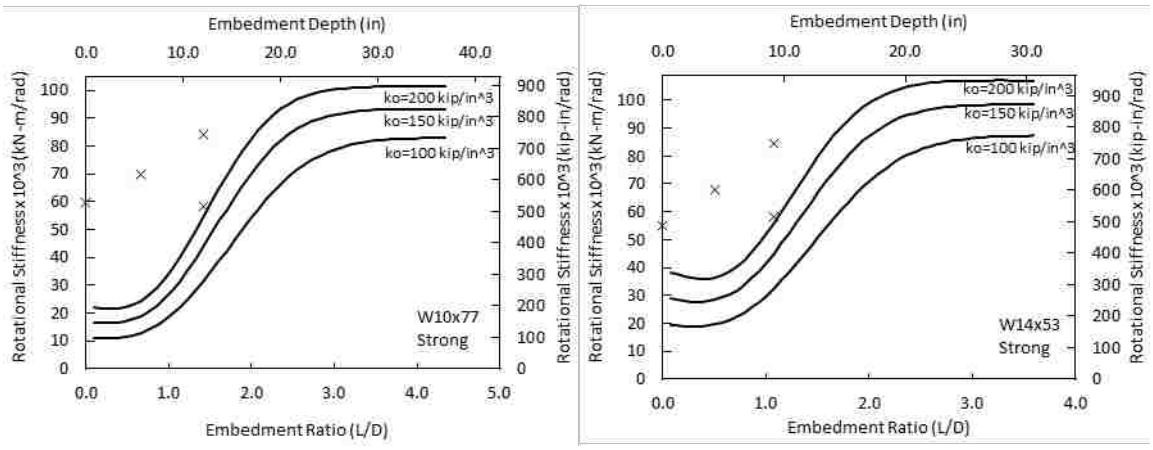

Figure 4-8: Hanks' experiments compared to Tryon's model using Equation 4-5. The concrete footing blockout moduli were 3600 ksi.

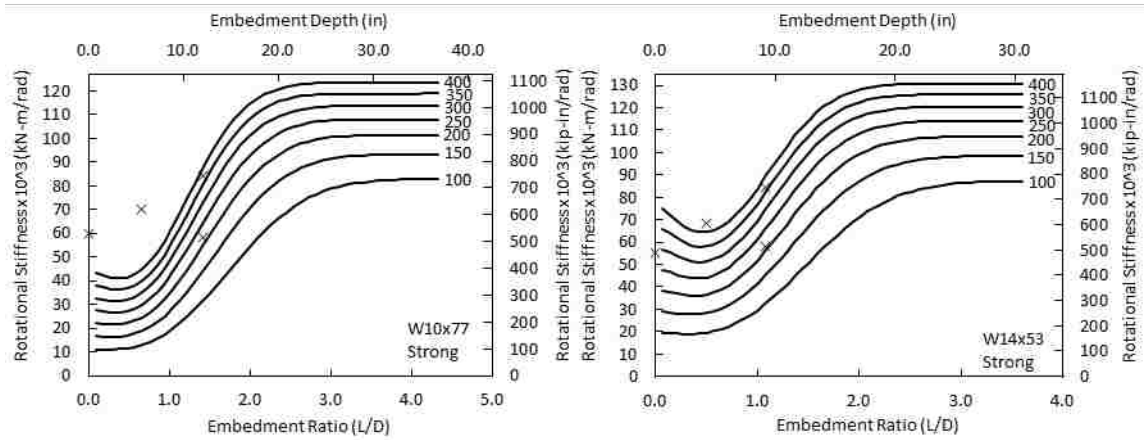

Figure 4-9: Hanks' experiment compared to Tryon's model using Equation 4-5 for multiple values of k_o. The concrete footing and blockout moduli were 3600 ksi.

The responses of the model are shown again with the modulus of subgrade reaction, k_o, ranging from 100 to 400 kip/in^3 with 50 kip/in^3 increments. Figure 4-9 shows that an adjustment of the modulus of subgrade reaction only may not be enough to represent the rotational stiffness of a column.

Figure 4-8 and Figure 4-9 show that Tryon's modified model under predicts values for these two larger shapes. Therefore, Tryon's model needed to account for the increased stiffness that Hanks' experiments were suggesting. This increased stiffness was most likely due to the base plates of Hanks' experiments being thicker than that in Barnwell's specimens. Therefore, this affected the flexibility of the base plate and thus the effective depth of the column, or the variable d. To test the theory, the effective depth of the column was changed in Equation (4-4). The effective depth was changed to be the distance between the centerline of the anchor rods, which was 16 inches for the F series and 18 inches for the D series and the results are shown in Figure 4-10. The figure shows increased predicted rotational stiffness from what is shown in Figure 4-8; this increase in stiffness brings the curves predicted stiffness closer to Hanks specimen data. Figure 4-11 shows the response of the model with k_o values are used ranging from 100 to 400 kip/in^3 with 50 kip/in^3 increments.

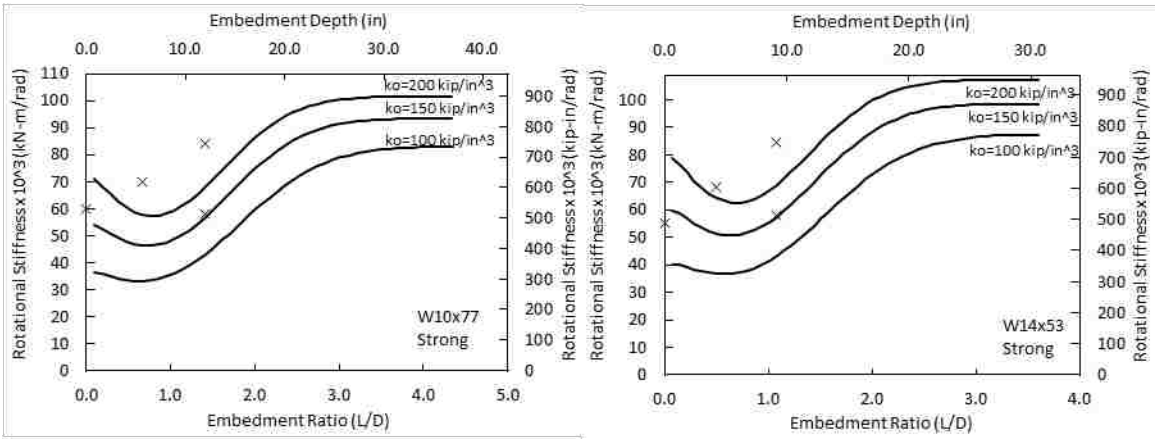

Figure 4-10: Hanks' experiments compared to Tryon's model using Equation 4-5 when d is the distance between anchor bolts. The concrete footing and blockout moduli were 3600 ksi.

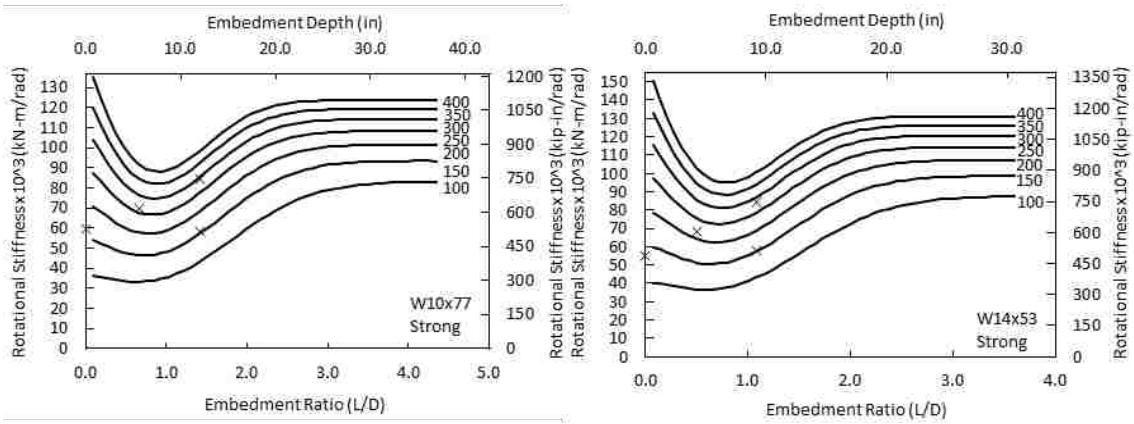

Figure 4-11: Hanks' experiment compared to Tryon's model using Equation 4-5 when d is the distance between anchor bolts and with multiple k_o. The concrete footing and blockout moduli are 3600 ksi.

The model response for either assumption of d, the depth of the column or the distance between anchor rods, did not indicate sensitivity to of the subgrade modulus value, thus values between 150 and 300 kip/in^3 seem reasonable. Some judgement was required for selecting a single value of the modulus of subgrade reaction, but a value of k_o of 200 kip/in^3 is a decent approximation. However, it appeared that the increased effective depth was beneficial in modeling Hanks' specimens with thicker base plates.

Before the new assumption of the parameter d, column depth, for Hanks' specimen was used, the model was validated using the exposed length assumptions made in Section 4.2.1. Figure 4-12 shows the response of the model for the two column lengths and there is not a significant difference between them. Therefore, the exposed length of 86 inches is continued to be used.

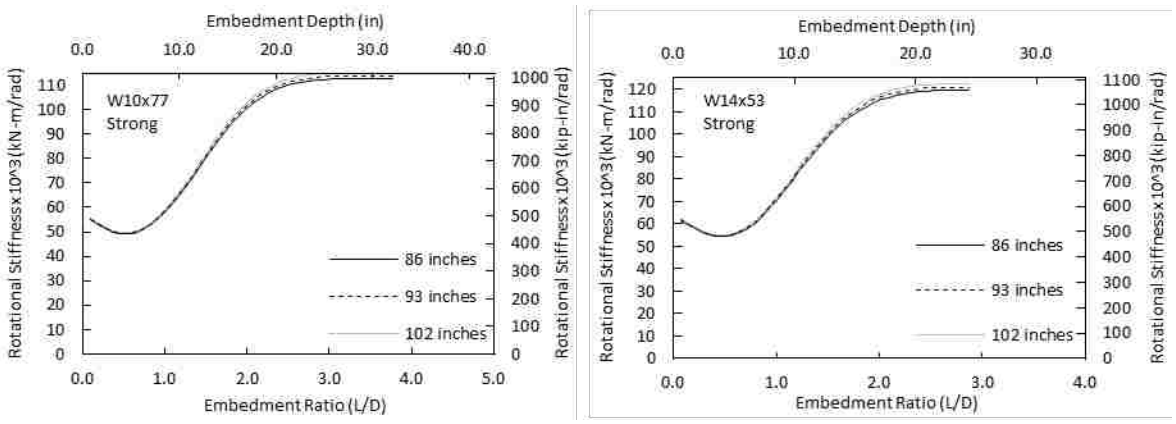

Figure 4-12: Exposed length comparison for Hanks' experiments when d is the distance between anchor bolts. d = 16 inches for W10 and d = 18 inches for W14 (k_o = 150 kip/in^3).

4.3.3 Direct Comparison

Figure 4-13 shows the direct comparison of Tryon's original model to the modified model with Barnwell's specimens represented with "xs". A value for the modulus of subgrade reaction of 150 kip/in^3 was used for modeling as was suggested in Section 4.3.1. It can be seen that for the lower embedment there is not a lot of difference in the model, but for the deeper embedment there is a greater change. A similar comparison is shown for Hanks data in Figure 4-14. Again, a direct comparison of the original model and the modified model. Hanks' specimens are shown with "xs". A modulus of subgrade reaction of 200 kip/in^3 was used as suggested in Section 4.3.2. There is not as close a solution for Hanks' specimens; however, Hanks' results are fairly close to the predicted rotational stiffnesses.

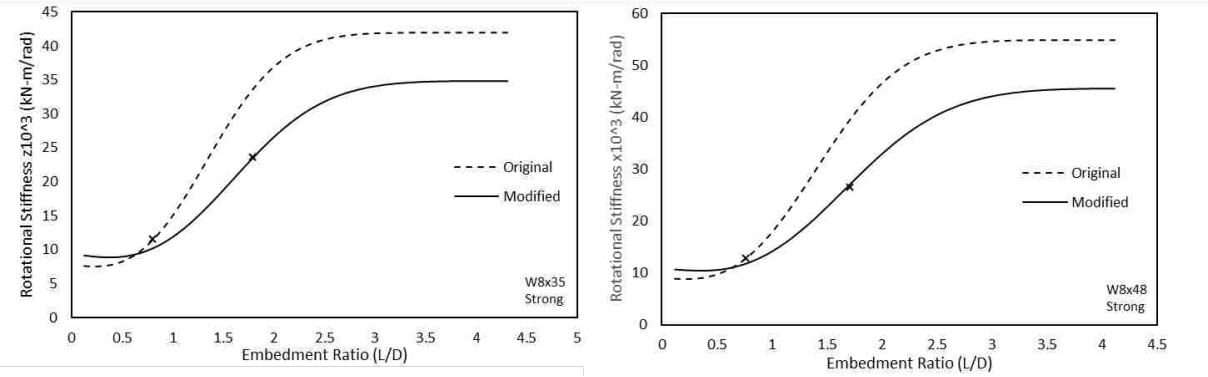

Figure 4-13: Comparison of Tryon's original model to the modified model with Barnwell's specimens (k_o=150 kip/in^3).

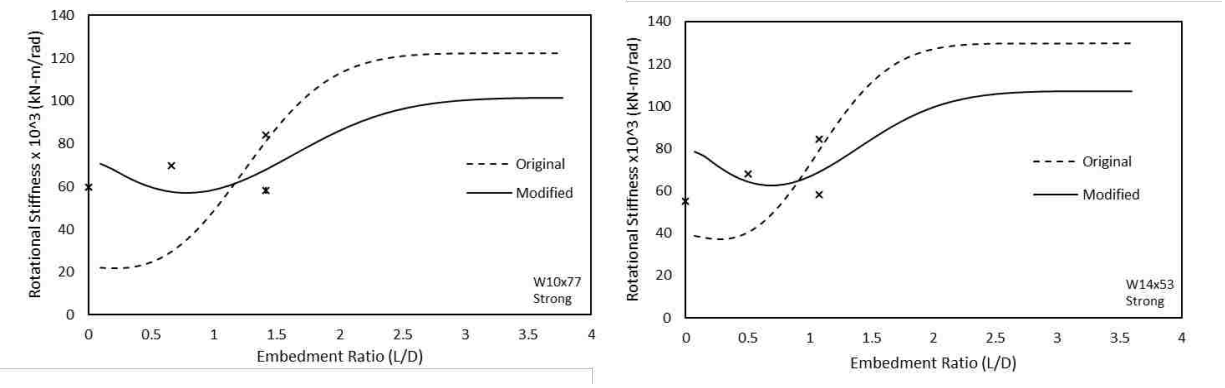

Figure 4-14: Comparison of Tryon's original model to the modified model with Hanks' specimens (k_o=200 kip/in^3).

4.4 Summary

Tryon's model was improved to account for several different assumptions for the given parameters and has better predictive capabilities for any wide-flange shape. The effect of the exposed length, flange effective width, concrete modulus, and the column depth were evaluated to determine the sensitivity of the model.

The first parameter that was evaluated was the exposed length. It was noted that the model was not sensitive to this parameter, and therefore, a single length for all of Barnwell's specimens and a single length for all of Hanks' specimens were used. Barnwell's specimens used an exposed length of 83.375 inches and Hanks' specimens had an exposed length of 86 inches.

The next parameter evaluated was flange effective width. It was determined that looking at flange effective width by itself did not give a clear idea whether it should be included or excluded; however, when this parameter was combined with other parameters the response of the model improved. Therefore, the flange effective width parameter was excluded from the model.

The influence of the concrete modulus was not immediately obvious and the assumption was made to use instead the ratio of the footing concrete over the blockout concrete. This new assumption, when combined with the other parameters, improved the response of the model. The equation used was Equation (4-4).

The final parameter investigated was the depth of the column. Barnwell's base plate was not very thick and therefore, the depth of the column seemed to be sufficient. However, Hanks' thicker base plate led to greater rotational stiffness. Therefore, the effective depth of the column was increased for the thicker base plates to be the distance between the centerline of the anchor bolts. Therefore, the parameter d was equal to 16 inches for the W10 column and 18 inches for the W14 column.

5 SYSTEM LEVEL SENSITIVITY

5.1 Introduction

In Tryon's model the rotational stiffness, β, was dependent upon the value chosen for the modulus of subgrade reaction, k_o. However, determining an appropriate value for the modulus of subgrade reaction is a challenge. It was, therefore, determined to study the sensitivity of the total stiffness to the rotational stiffness, β, and determine how accurate β must be in order to obtain reasonable values for the total stiffness. The sensitivity analysis was done by comparing the system stiffness to the rotational stiffness, β, for several values of the modulus of subgrade reaction. A moment frame with partially fixed base columns was used in this study.

5.2 Method

5.2.1 Sensitivity of Total Stiffness as Modulus of Subgrade Reaction Changes

The total stiffness of a column was investigated to determine its sensitivity to β as k_o was changed. This was done by determining the stiffness of the column and base connection separately. Equation (5-1) is the flexural stiffness of a single cantilever column, which depends on the modulus of elasticity, the moment of inertia, and the exposed length of the column. The stiffness of the embedment depth was determined by Equation (5-2). This was the stiffness provided by a rotational spring at the top of the slab. The rotational stiffness at the top of the slab provided by the embedment, β, was determined by using Hetényi's beam equations and the

work completed by Tryon as described previously in Section 2.2.4. The same exposed length of the column was used in Equation (5-2) as was used in Equation (5-1). Equation (5-3) was used to combine the stiffness provided by the column and the stiffness provided by the base in order to determine total stiffness of the exposed column and the embedded portion.

$$k_{cantilever} = \frac{3EI}{L^3} \tag{5-1}$$

$$k_{base} = \frac{\beta}{L^2} \tag{5-2}$$

$$k_{column} = \frac{1}{\frac{1}{k_{base}} + \frac{1}{k_{cantilever}}} \tag{5-3}$$

5.2.2 Sensitivity of Total Stiffness as the Rotational Stiffness β Changes

The sensitivity of k_{column} with respect to β was investigated for a moment frame with rotational springs at top of the slab as depicted in Figure 5-1. A closed form solution was developed for half of the moment frame with corresponding variables: EI_b, EI_c, H, L, β, and F. The half moment frame was chosen for simplicity, as shown in Figure 5-2. The frame was divided into three members: Member AB, Member BC, and the rotational spring. The three members, boundary conditions, and the degrees of freedom are shown in Figure 5-3. The four degrees of freedom: 1) rotation at A, 2) constrained to be equal DOF translation at B, 3) rotation at B, and 4) rotation at C.

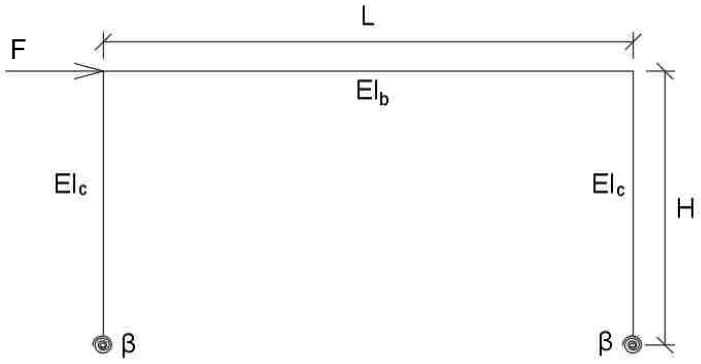

Figure 5-1: Full moment frame and system parameters with partial fixity denoted at the top of the slab.

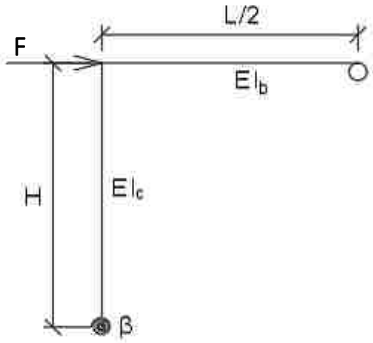

Figure 5-2: Half the moment frame and system parameters for the system analyzed with partial fixity denoted at the top of the slab.

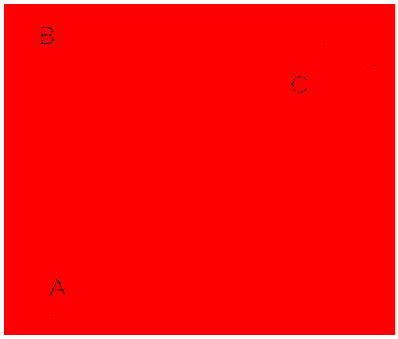

Figure 5-3: The four degrees of freedom and nodes for the half moment frame.

The closed form solution was developed by using the stiffness method. A brief explanation of the steps is discussed here. Appendix A presents, in detail the development of the closed form solution. Individual stiffness matrices were constructed for each of the three members. These three matrices were then used to construct the global stiffness matrix. A force vector was defined, which was simply a horizontal force applied at node B as shown in Figure 5-3. Deformation was then calculated from the global stiffness and the forcing vector with the equation $F = k_{half-frame} * \Delta$. The total stiffness of the half-frame was then determined by dividing the applied force by the translational deformation at node B or node C or as expressed in equation, $F/\Delta_{B||C}$. This value was then multiplied by two if a full moment frame was desired. The final equation for the system stiffness is given by Equation (5-4).

$$k_{half-frame} = \frac{36I_b E^2 I_c^2 + 6L\beta E I_c^2 + 36HI_b\beta E I_c}{3H^4 I_b \beta + 12EH^3 I_b I_c + 2H^3 I_c L\beta + 6EH^2 I_c^2 L} \quad (5\text{-}4)$$

Equation (5-4) was validated by doing hand calculations as well as creating a simple computer model for a single moment frame. Two cases were checked with the computer model: First, β = 100,000 kip-in/rad, $I_c = I_b$ = 200 in^4, E = 29,000 ksi, H = 86 inches, L = 2*H, which resulted in a stiffness of 56.84 kip/in; Second, β = 200,000 kip-in/rad, $I_c = I_b$ = 200 in^4, E = 29,000 ksi, H = 86 inches, L = 2*H, which resulted in a stiffness of 72.67 kip/in. These results matched to at least three decimal places to that obtained using the closed form solution. Assuming values of beta of zero and infinity, the closed form solution is that of the pinned-pinned situation and the fixed-fixed situation.

5.2.3 Sensitivity Analysis for Larger Moment Frame Systems

An equation for the stiffness of a single moment frame with partially fixed base connections was developed in the previous section, Section 5.2.2. In this section, equations are presented for elements of a larger system with multiple bays and stories with partially fixity at the top of the slab as shown in Figure 5-4.

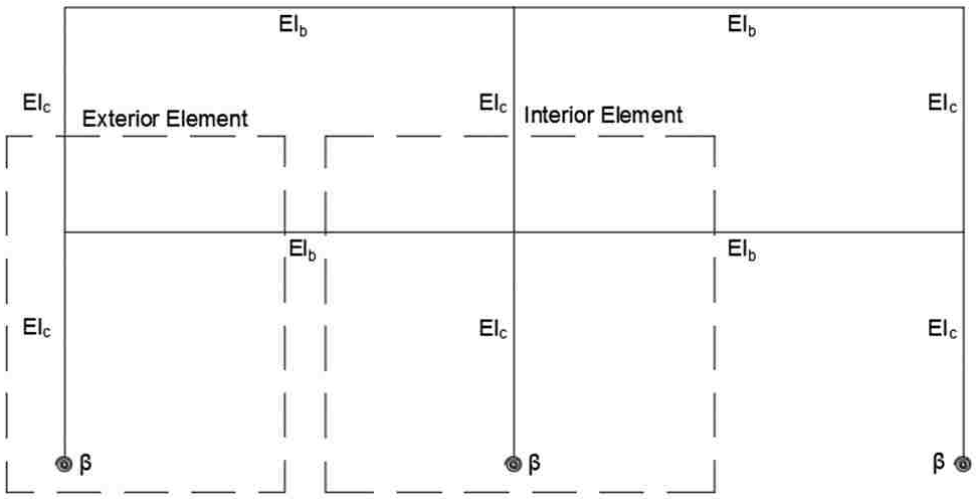

Figure 5-4: Multi-story and bay moment frame with system parameters labeled and partial fixity denoted at each top of the slab.

There were two configurations developed, which were used to create the stiffness of a multi-story and multi-bay moment frames. The configurations are shown in Figure 5-5 for the exterior elements and Figure 5-6 for the interior elements. Figure 5-7 and Figure 5-8 show the degrees of freedom for the exterior and the interior sections, respectively. The configuration in Figure 5-7 has six degrees of freedom: 1) rotation at A, 2) constrained to be equal DOF translation at B and C, 3) rotation at B, 4) rotation at C, 5) translation at D, and 6) rotation at D. Figure 5-8 has seven degrees of freedom: 1) rotation at A, 2) constrained to be equal DOF translation at B and E, 3) rotation at B, 4) rotation at C, 5) translation at D, 6) rotation at D, and 7) rotation at E.

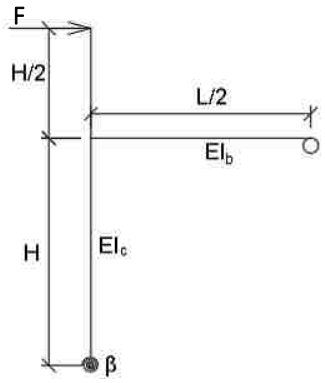

Figure 5-5: Exterior element of a multi-story and bay moment frame with system parameters labeled and partial fixity noted at the top of the slab.

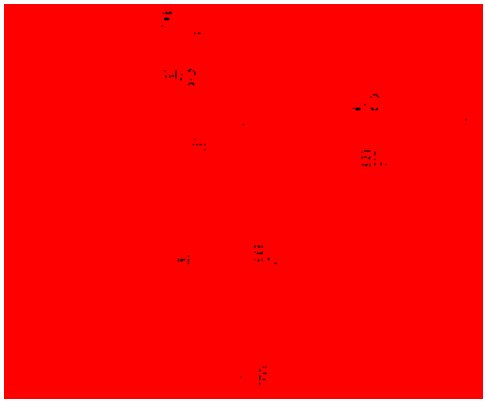

Figure 5-6: Interior element of multi-story and bay moment frame with system parameters labeled and partial fixity noted at the top of the slab.

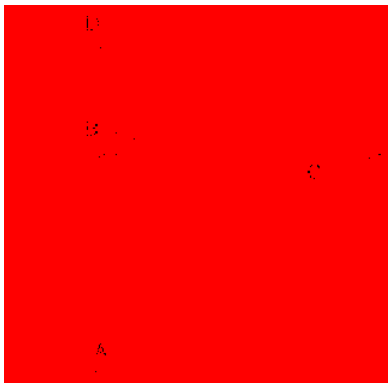

Figure 5-7: Six degrees of freedom for the exterior elements of a multi-story and bay moment frame as used in analysis.

Figure 5-8: Seven degrees of freedom for the interior elements of a multi-story and bay moment frame as used in analysis.

Using the direct stiffness method, the stiffness Equation (5-5) and Equation (5-6) were obtained for the configurations on the exterior of the frame and for an interior section, respectively. These modules were used to construct the stiffness for a full frame of multiple bays and stories.

$$k_{exterior} = \frac{48I_bE^2I_c^2 + 8L\beta EI_c^2 + 48HI_b\beta EI_c}{6H^4I_b\beta + 18EH^3I_bI_c + 9H^3I_cL\beta + 18EH^2I_c^2L} \quad (5\text{-}5)$$

$$k_{interior} = \frac{96I_bE^2I_c^2 + 8L\beta EI_c^2 + 96HI_b\beta EI_c}{12H^4I_b\beta + 36EH^3I_bI_c + 9H^3I_cL\beta + 18EH^2I_c^2L} \quad (5\text{-}6)$$

The resulting equations were verified with a computer model. There were two different cases verified for the interior frame: First, β = 100,000 kip-in/rad, $I_c = I_b = 127$ in^4, E = 29,000 ksi, H = 170 inches, H = 2*L, which resulted in a stiffness of 3.45 kip/in; Second, β = 200,000 kip-in/rad, $I_c = I_b = 120$ in^4, E = 29,000 ksi, H = 170 inches, H = 2*L, which resulted in a stiffness of 3.87 kip/in. These results matched to at least three decimal places to that obtained using the closed from solution.

5.3 Results

5.3.1 Sensitivity of Total Stiffness as Modulus of Subgrade Reaction Changes

With Equation (5-3) determined for the total stiffness of the column, a graph was developed to compare the effects of the rotational stiffness, β, on the total stiffness of the system. Figure 5-9 shows the total stiffness versus the rotational stiffness, β. Different values of β were calculated by changing the modulus of subgrade reaction, k_o, incrementally in order to achieve a smooth curve. Constant values for E, I, and L were assumed in order to plot the graph. (E = 29000 ksi, I = 127 in^4, and L = 83.375 inches, for a W8 × 35 column).

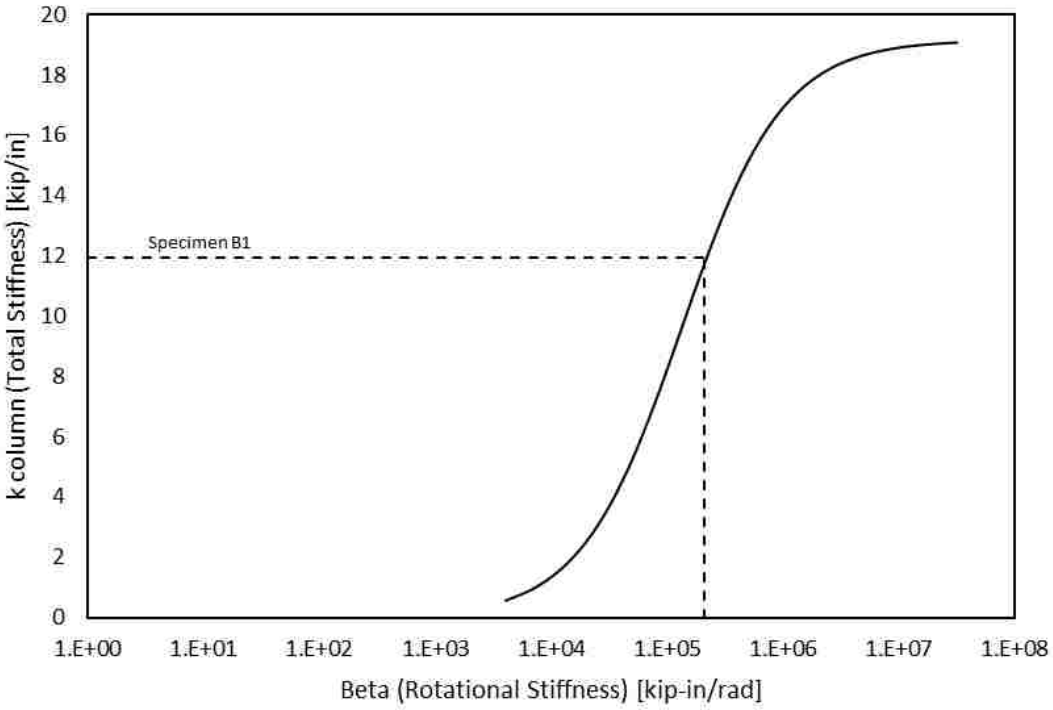

Figure 5-9: Barnwell's W8x35 14.5 inches embedment depth - single column stiffness analysis.

Figure 5-9 shows a steep rise in the middle of the graph. This suggested that the rotational stiffness was more sensitive for these particular parameters, due to the rapidly changing total stiffness values as the modulus of subgrade reaction was changing. This observation was expected, considering that the properties of the concrete were essential to the stiffness provided to the system from the embedment depth.

5.3.2 Sensitivity of Total Stiffness as the Rotational Stiffness β Changes

The closed form solution developed for a simple moment frame with a partially fixed base was used to evaluate the total stiffness as the rotational stiffness changes. The first step in determining the sensitivity of the total stiffness was to select several values for the modulus of

subgrade reaction, 100 kip/in^3 – 200 kip/in^3. These values for the subgrade modulus were then used in Tryon's model to develop a range of rotational stiffness values when the parameters for a specific column was chosen. The range of rotational stiffness values were then plugged into the closed form solution. The beam length was two times the height with the height representing a single 10-foot story height. Figure 5-10 gives reference to the extremes of the rotational stiffness and is similar for all analysis. When the rotational stiffness is zero then this is considered a pinned connection and as the rotational stiffness goes to infinity then this is considered a fixed connection.

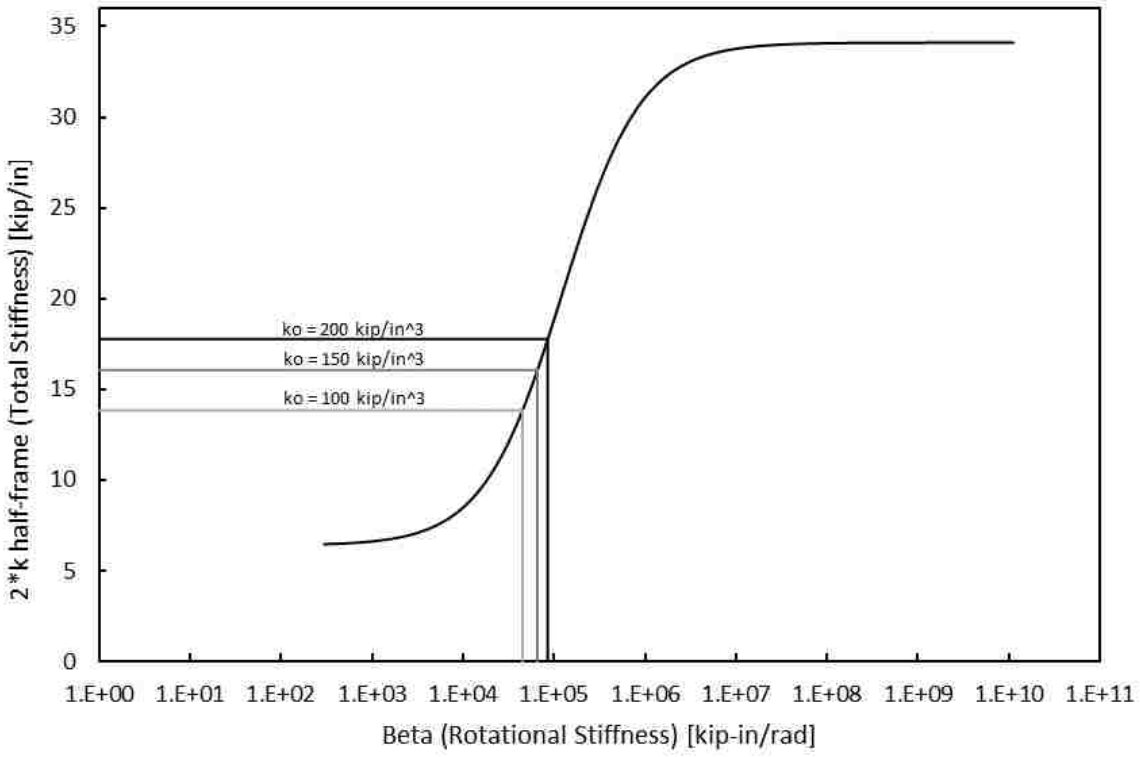

Figure 5-10: Comparison of stiffness for W8x35 of 6.5 inches embedment depth for a large range of rotational stiffness.

Figure 5-11 shows the predicted total stiffness values of a moment frame with W8 × 35 columns and beam and a column embedment depth of 6.5 inches. This resulted in a range of

rotational stiffness values, β, between 45,092 kip-in/rad and 85,438 kip-in/rad and a corresponding range of total stiffness values between 13.8 kip/in and 17.8 kip/in. The high end of β is 89% greater than the low end β, and the high end of stiffness is 28% greater than the low end. Therefore, stiffness can probably be predicted within 28%.

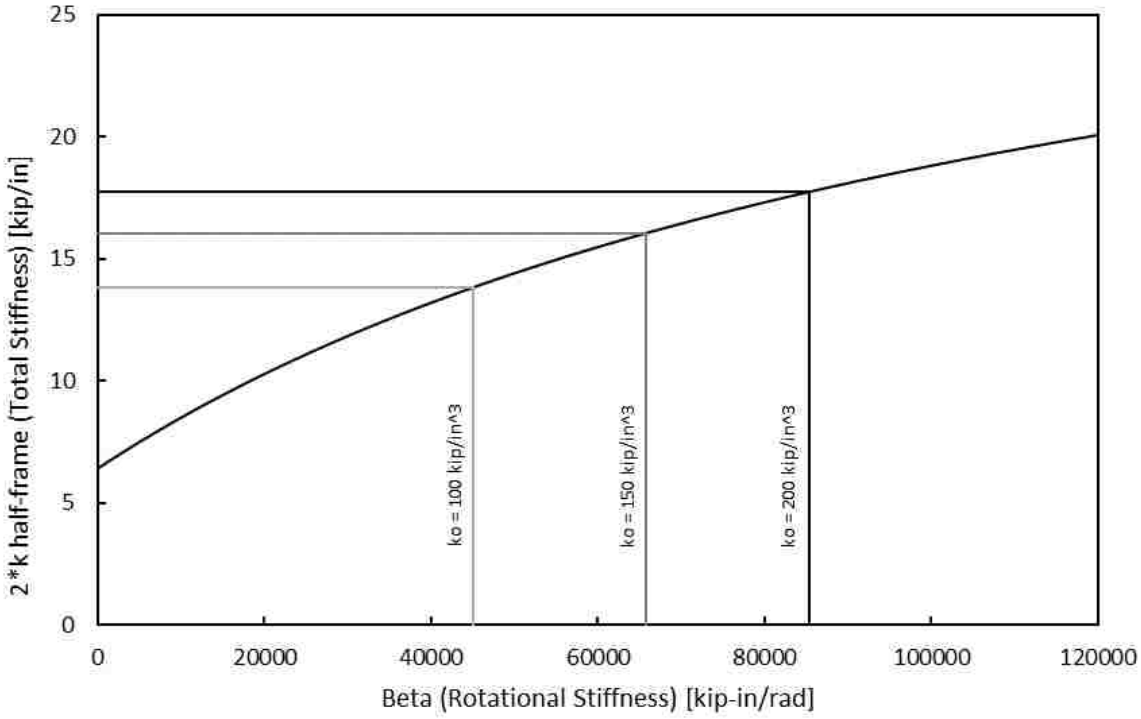

Figure 5-11: Comparison of stiffness for W8x35 of 6.5 inches embedment depth from Barnwell's experiments and Tryon's model for a partially fixed moment frame

Figure 5-12 shows the predicted total stiffness values when the column embedment was increased to 14.5 inches keeping the columns and the beam the same as W8 × 35. The figure shows that a range of β values between 147,933 kip-in/rad and 239,654 kip-in/rad results in a range for the total stiffness between 21.5 kip/in and 24.7 kip/in. The high end of β is 62% greater than the low end β, and the high end of stiffness is 15% greater than the low end. Therefore, stiffness can probably be predicted within 15%. Table 5-1 shows a more complete

list of rotational stiffness values and their corresponding total stiffness values calculated for all of the modulus of subgrade reaction values shown in the figures, as well as the two embedment depths discussed.

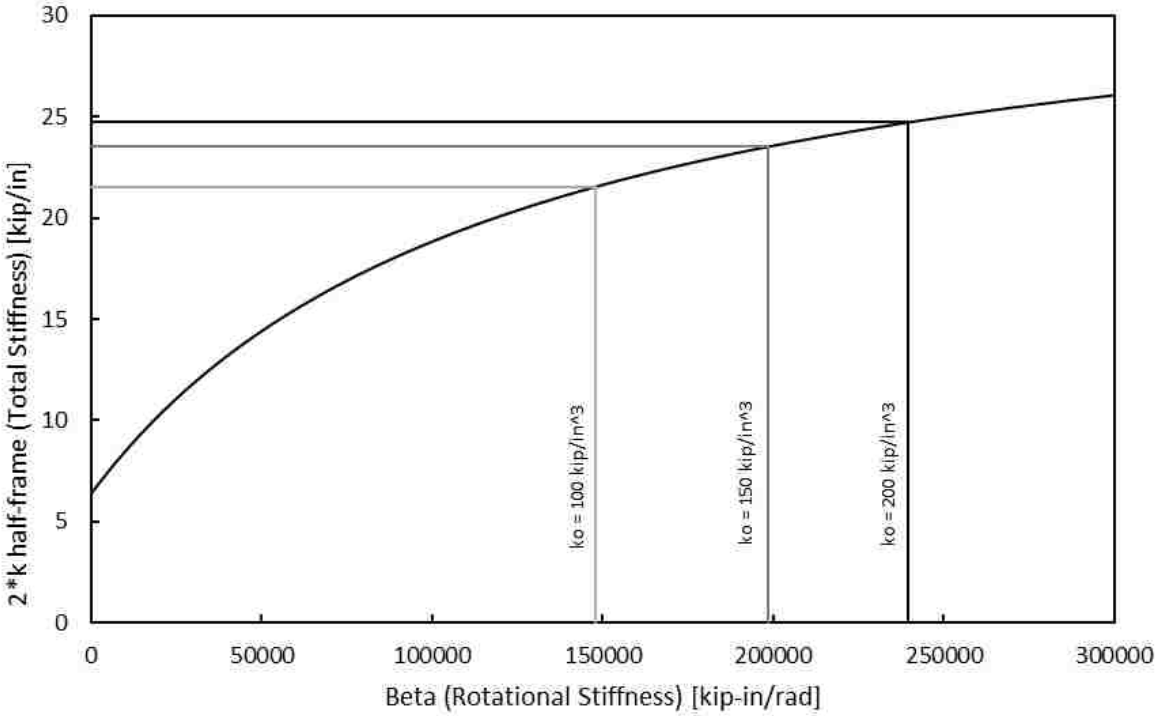

Figure 5-12: Comparison of stiffness for W8x35 of 14.5 inches embedment depth from Barnwell's experiments and Tryon's model for a partially fixed moment frame.

Table 5-1: W8x35 Percent Change Comparison of Stiffness

Embedment Depth (inches)	Modulus of Subgrade Reaction (k_o=kips/in^3)	Value of β (kip-in/rad)	Value of Total Stiffness (kip/in)
6.5	100	45,092	13.8
	150	65,807	16.1
	200	85,438	17.8
14.5	100	147,933	21.5
	150	198,430	23.5
	200	239,654	24.7

Figure 5-13 shows the predicted stiffness values if a W10 × 77 was used for the columns and beam; a column embedment depth of 7 inches was assumed. These assumptions resulted in a range of rotational stiffness values between 300,809 kip-in/rad and 522,451 kip-in/rad and resulted in a range of total stiffness values between 63.2 kip/in and 76.8 kip/in. The high end of β is 74% greater than the low end β. The high end of stiffness is 21% greater than the low end. Therefore, stiffness can probably be predicted within 21%.

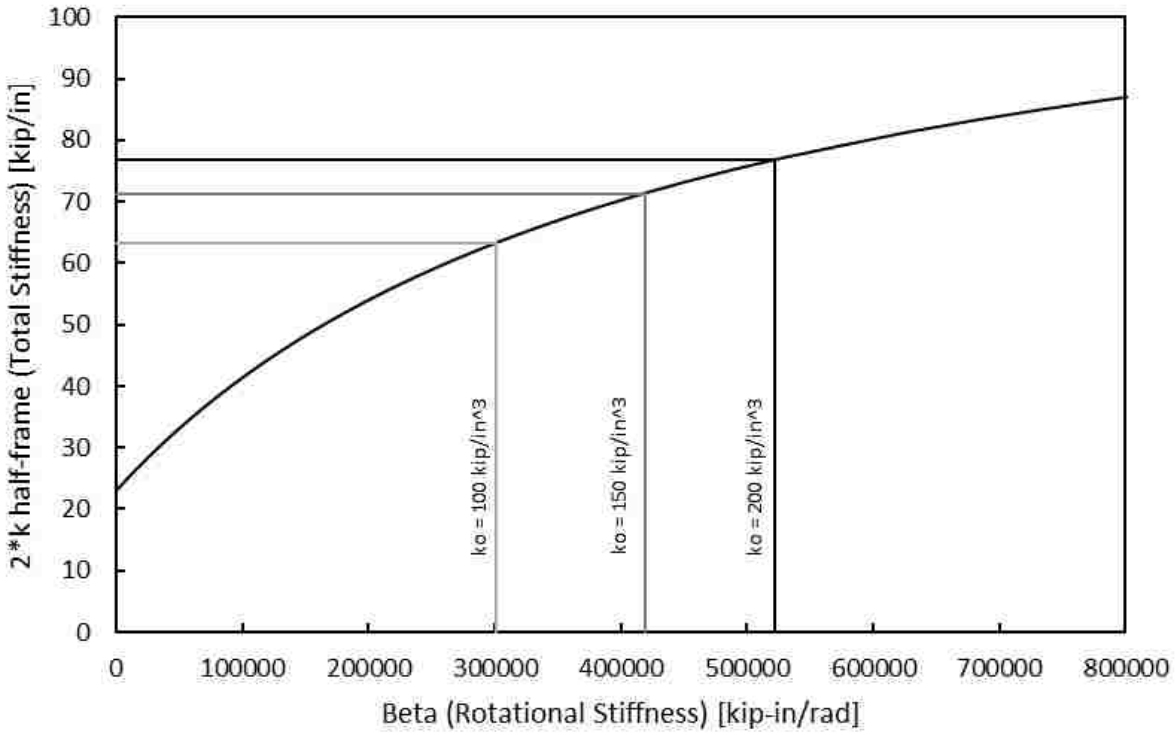

Figure 5-13: Comparison of stiffness for W10x77 of 7 inches embedment depth from Hanks' experiments and Tryon's model for a partially fixed moment frame.

Figure 5-14 shows the results for a moment frame with columns and beam with W10 × 77 shape, but the column embedment depth is increased to 15 inches. Figure 5-14, shows a range of

β values between 398,196 kip-in/rad and 626,350 kip-in/rad, which resulted with a total stiffness range between 70.1 kip/in and 81.2 kip/in. The high end of β is 57% greater than the low end β. The high end of stiffness is 16% greater than the low end. Therefore, stiffness can probably be predicted within 16%. Table 5-2 shows a more complete list of rotational stiffness values and total stiffness values calculated for all of the modulus of subgrade reaction values shown in the figure, as well as the two embedment depths discussed.

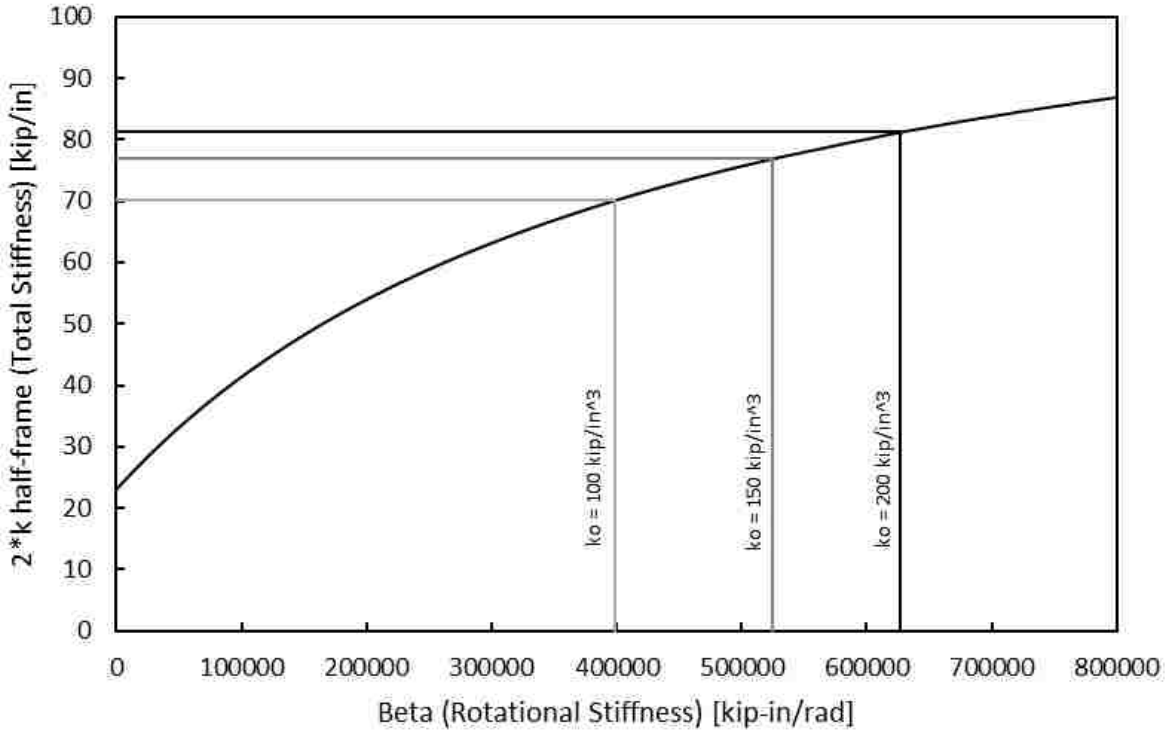

Figure 5-14: Comparison of stiffness for W10x77 of 15 inches embedment depth from Hanks' experiments and Tryon's model for a partially fixed moment frame.

Table 5-2: W10x77 Percent Change Comparison of Stiffness

Embedment Depth (inches)	Modulus of Subgrade Reaction (k_o=kips/in^3)	Value of β (kip-in/rad)	Value of Total Stiffness (kip/in)
7	100	300,809	63.2
	150	419,380	71.4
	200	522,451	76.8
15	100	398,196	70.1
	150	524,920	76.9
	200	626,350	81.2

5.3.3 Sensitivity Analysis for Larger Moment Frame Systems

In the previous section a single bay moment frame was analyzed for the sensitivity of the total stiffness to the rotational stiffness. In this section, a larger moment frame was analyzed in a similar manner. Values for the modulus of subgrade reaction was chosen and used in Tryon's model to get a range of rotational stiffness values. These rotational stiffness values were then used in the closed form solutions that were developed in Section 5.2.3. There were two separate configurations, one for the exterior sections of the moment frame and one for the interior sections of the moment frame as seen in Figure 5-4. Figure 5-15 through Figure 5-22 were developed for several different assumptions for the column size and column embedment depth; the beam size was assumed to be similar to the column. The height of each story was to represent a 10-foot story height. The length was represented as two times the height.

Figure 5-15 shows the predicted stiffness of an exterior column assembly when a W8 × 35 column was used with a column embedment depth of 6.5 inches. The beam was also assumed to

have a similar moment of inertia. A range of rotational stiffness values, β, between 45,092 kip-in/rad and 85,438 kip-in/rad resulted in a range of total stiffness values between 3.39 kip/in and 3.99 kip/in. The high end of β is 89% greater than the low end β, and the high end of stiffness is 18% greater than the low end. Therefore, stiffness can probably be predicted within 18%.

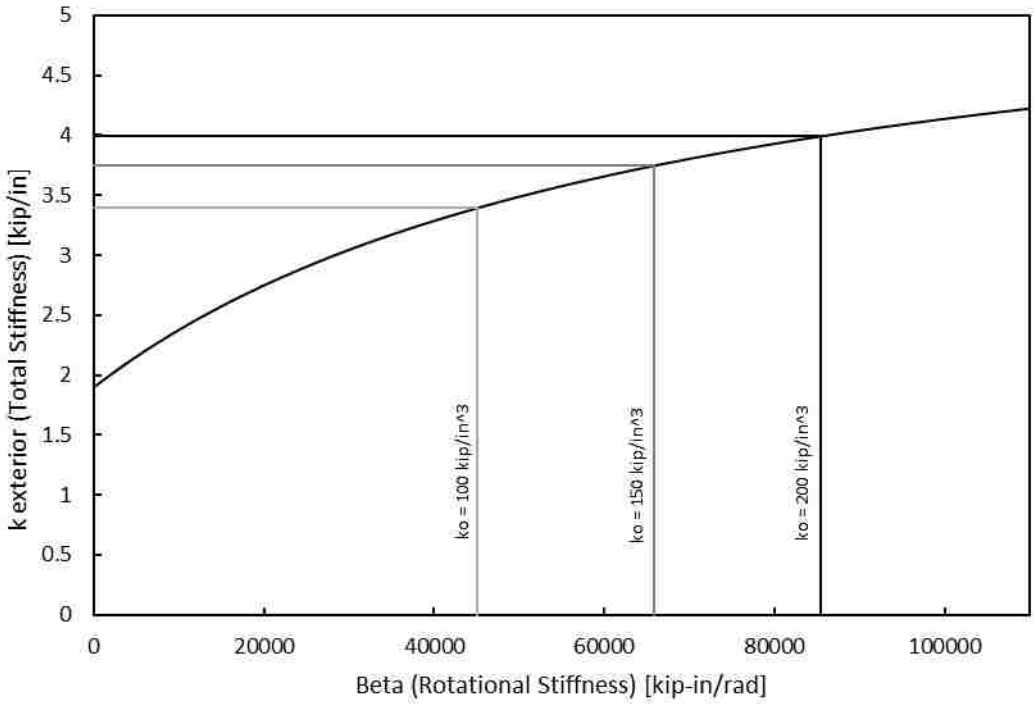

Figure 5-15: Plot of total stiffness versus rotational stiffness for exterior assembly (W8x35 – 6.5 inches embedment depth).

Figure 5-16 is for an exterior column assembly when a W8 × 35 column was used with the beam using a similar moment of inertia and a column embedment depth of 14.5 inches. The figure shows that for a range of β values between 147,933 kip-in/rad and 239,654 kip-in/rad resulted in a range for the total stiffness between 4.48 kip/in and 4.84 kip/in. The high end of β is 62% greater than the low end β, and the high end of stiffness is 8% greater than the low end.

Therefore, stiffness can probably be predicted within 8%. Additional information on the modulus of subgrade reaction that was used and its corresponding total stiffness, see Table 5-3 for both embedment depth shown in Figure 5-15 and Figure 5-16.

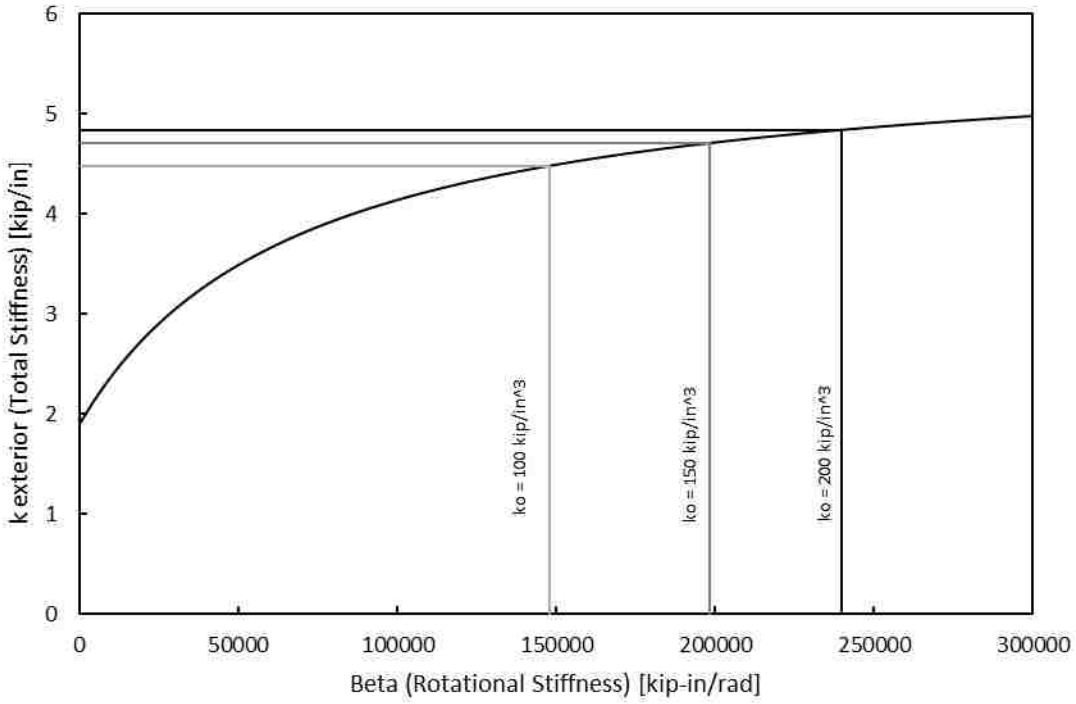

Figure 5-16: Plot of total stiffness versus rotational stiffness for exterior assembly (W8x35 – 14.5 inches embedment depth).

Table 5-3: W8x35 Exterior Percent Change Comparison of Stiffness

Embedment Depth (inches)	Modulus of Subgrade Reaction (k_o=kips/in^3)	Value of β (kip-in/rad)	Value of Total Stiffness (kip/in)
6.5	100	45,092	3.39
	150	65,807	3.74
	200	85,438	3.99
14.5	100	147,933	4.48
	150	198,430	4.71
	200	239,654	4.84

Comparison of the same shapes and embedment depths were used for an interior column assembly. Figure 5-17 shows the total stiffness for an interior W8 × 35 column with a column embedment depth of 6.5 inches. The beam was also assumed to have a similar moment of inertia. This figure shows a range for the rotational stiffness between 45,092 kip-in/rad and 85,438 kip-in/rad, which was the same range as seen in Figure 5-15; however, the range resulted in total stiffness values ranging between 4.78 kip/in and 5.59 kip/in. The high end of β is 89% greater than the low end β, and the high end of stiffness is 17% greater than the low end. Therefore, stiffness can probably be predicted within 17%. It can be noted the stiffness was increased from the exterior column, as shown in Figure 5-15 for the same values of rotational stiffness.

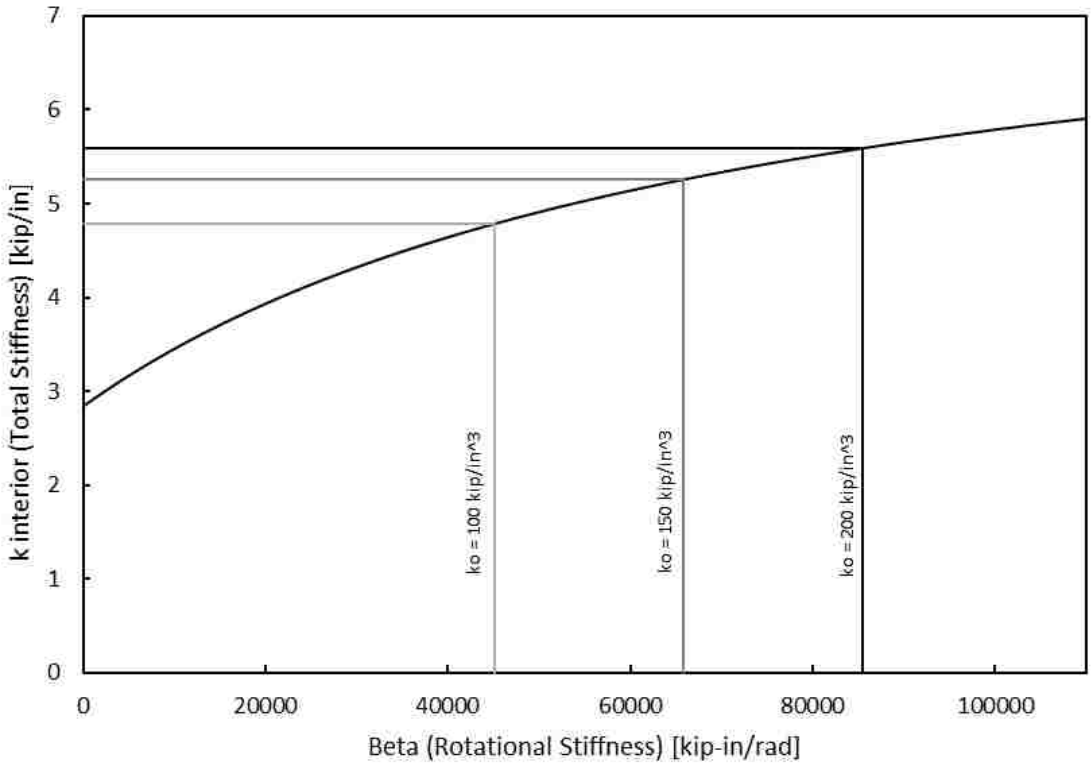

Figure 5-17: Plot of total stiffness versus rotational stiffness for interior assembly (W8x35 – 6.5 inches embedment depth).

Figure 5-18 shows the total stiffness of an interior W8 × 35 column with a column embedment depth of 14.5 inches. Again, a similar shape was used for the beam as was used for the column. This figure shows that for a range between 147,933 kip-in/rad and 239,654 kip-in/rad the rotational stiffness there was a range of total stiffness between 6.26 kip/in and 6.75 kip/in. The high end of β is 62% greater than the low end β, and the high end of stiffness is 8% greater than the low end. Therefore, stiffness can probably be predicted within 8%. This was similar to the results that were shown in Figure 5-16; however, it can be seen that there was an increased total stiffness. For additional details of the rotational stiffness corresponding to its total stiffness see Table 5-4.

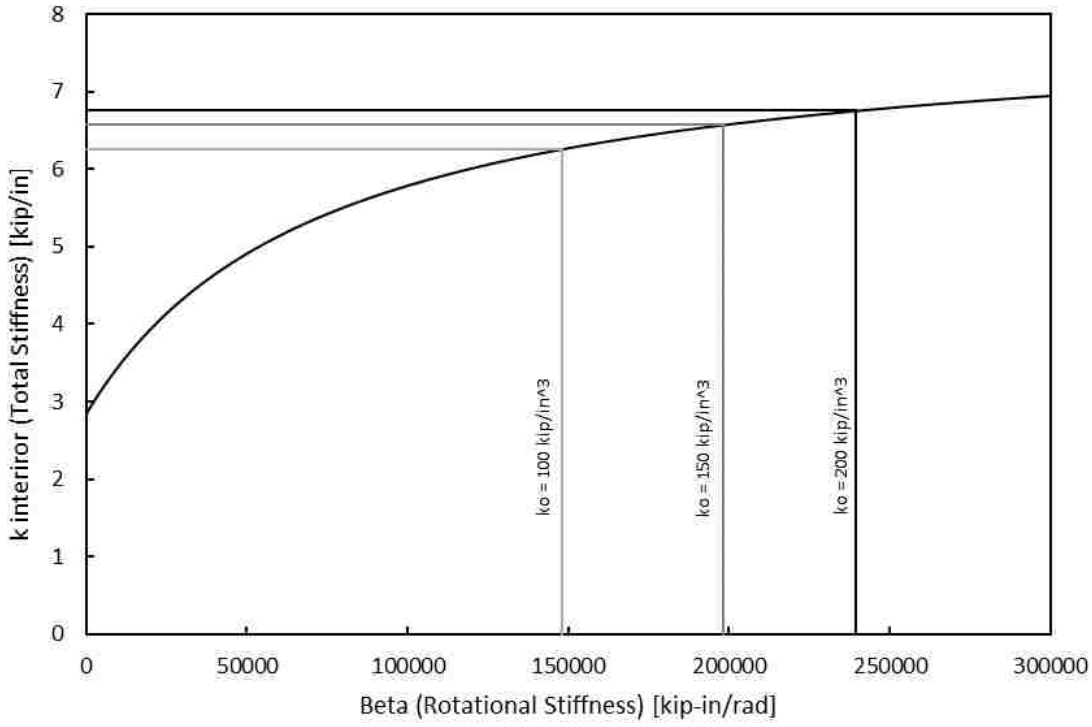

Figure 5-18: Plot of total stiffness versus rotational stiffness for interior assembly (W8x35 – 14.5 inches embedment depth).

Table 5-4: W8x35 Interior Percent Change Comparison of Stiffness

Embedment Depth (inches)	Modulus of Subgrade Reaction (k_o=kips/in^3)	Value of β (kip-in/rad)	Value of Total Stiffness (kip/in)
6.5	100	45,092	4.78
	150	65,807	5.26
	200	85,438	5.59
14.5	100	147,933	6.26
	150	198,430	6.57
	200	239,653	6.75

A larger shape size was evaluated next for both the exterior column assembly as well as the interior column assembly. Figure 5-19 shows the values for the total stiffness if a W10 × 77 exterior columns and the same shape for the beam was used. A column embedment depth of 7 inches was assumed. These assumptions resulted in a range of rotational stiffness values between 300,809 kip-in/rad and 522,451 kip-in/rad and resulted in a range of total stiffness values between 14.2 kip/in and 16.0 kip/in. The high end of β is 74% greater than the low end β, and the high end of stiffness is 12% greater than the low end. Therefore, stiffness can probably be predicted within 12%.

Figure 5-20 shows the values for the total stiffness if a W10 × 77 shape is used for the exterior columns and a beam with similar moment of inertia as the column; however, with 15 inches of column embedment depth. This resulted in a range of rotational stiffness values between 398,195 kip-in/rad and 626,350 kip-in/rad, which resulted in a total stiffness range between 15.2 kip/in and 16.5 kip/in. The high end of β is 57% greater than the low end β, and the high end of stiffness is 9% greater than the low end. Therefore, stiffness can probably be predicted within 9%. For additional information on the results seen in Figure 5-19 and Figure 5-20 see Table 5-5.

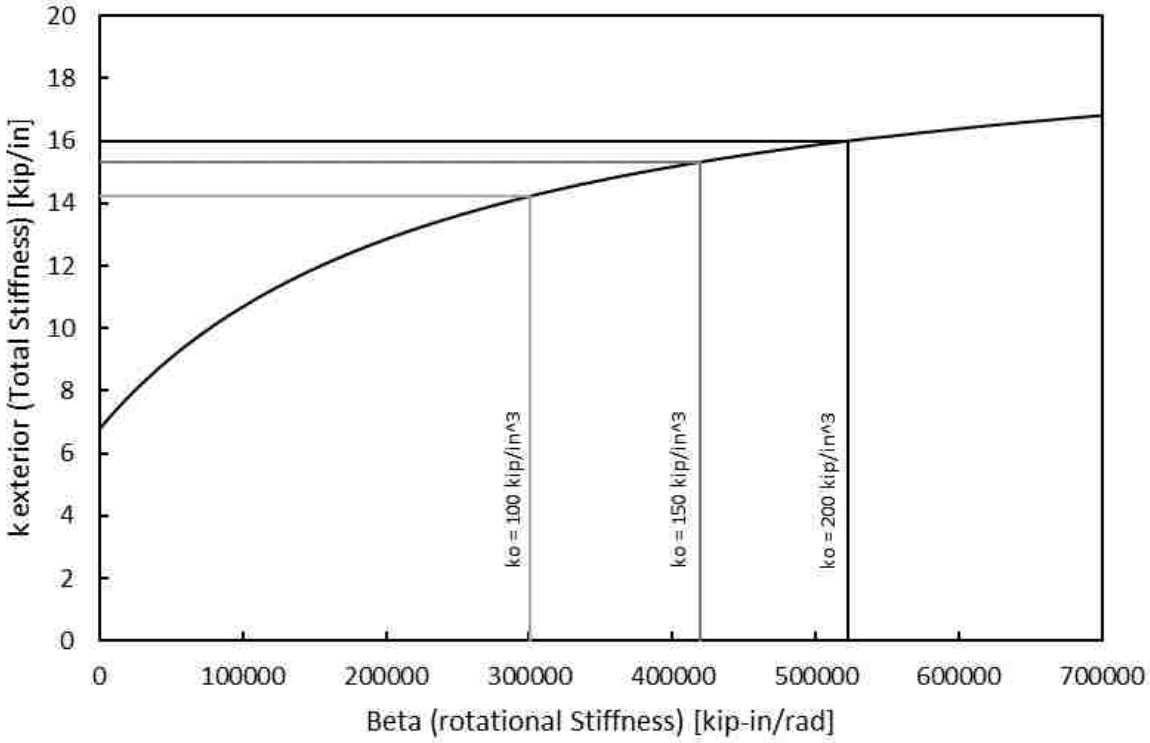

Figure 5-19: Plot of total stiffness versus rotational stiffness for exterior assembly (W10x77 – 7 inches embedment depth).

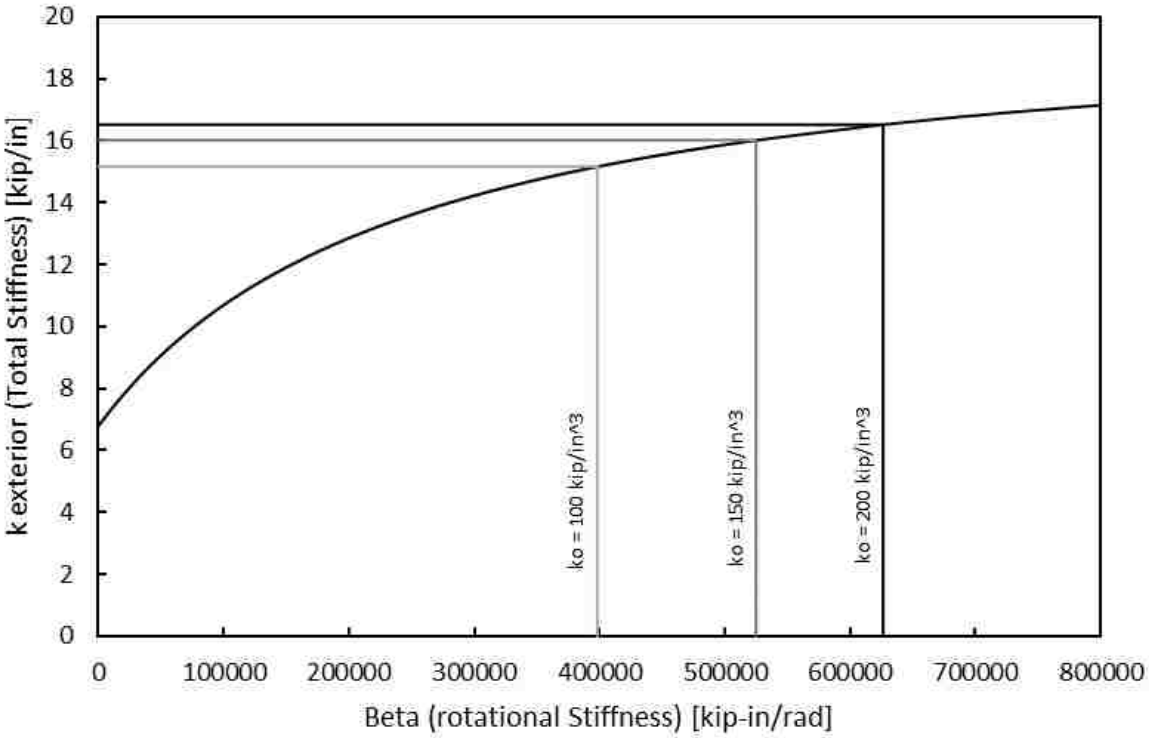

Figure 5-20: Plot of total stiffness versus rotational stiffness for exterior assembly (W10x77 – 15 inches embedment depth).

Table 5-5: W10x77 Exterior Percent Change Comparison of Stiffness

Embedment depth (inches)	Modulus of Subgrade Reaction (k_o=kips/in^3)	Value of β (kip-in/rad)	Value of Total Stiffness (kip/in)
7	100	300,809	14.2
	150	419,380	15.3
	200	522,451	16.0
15	100	398,196	15.2
	150	524,920	16.0
	200	626,350	16.5

The interior column assembly was evaluated next for comparison of the same shape and embedment depths. Figure 5-21 is the results for the total stiffness versus the rotational stiffness

when a W10 × 77 column and beam was used for the interior assembly and a column embedment depth of 7 inches. The figure shows a range for the rotational stiffness between 300,809 kip-in/rad and 522,451 kip-in/rad, which was the same range as seen in Figure 5-19; however, this range of β results in increased total stiffness values between 19.9 kip/in and 22.4 kip/in. The high end of β is 74% greater than the low end β, and the high end of stiffness is 12% greater than the low end. Therefore, stiffness can probably be predicted within 12%.

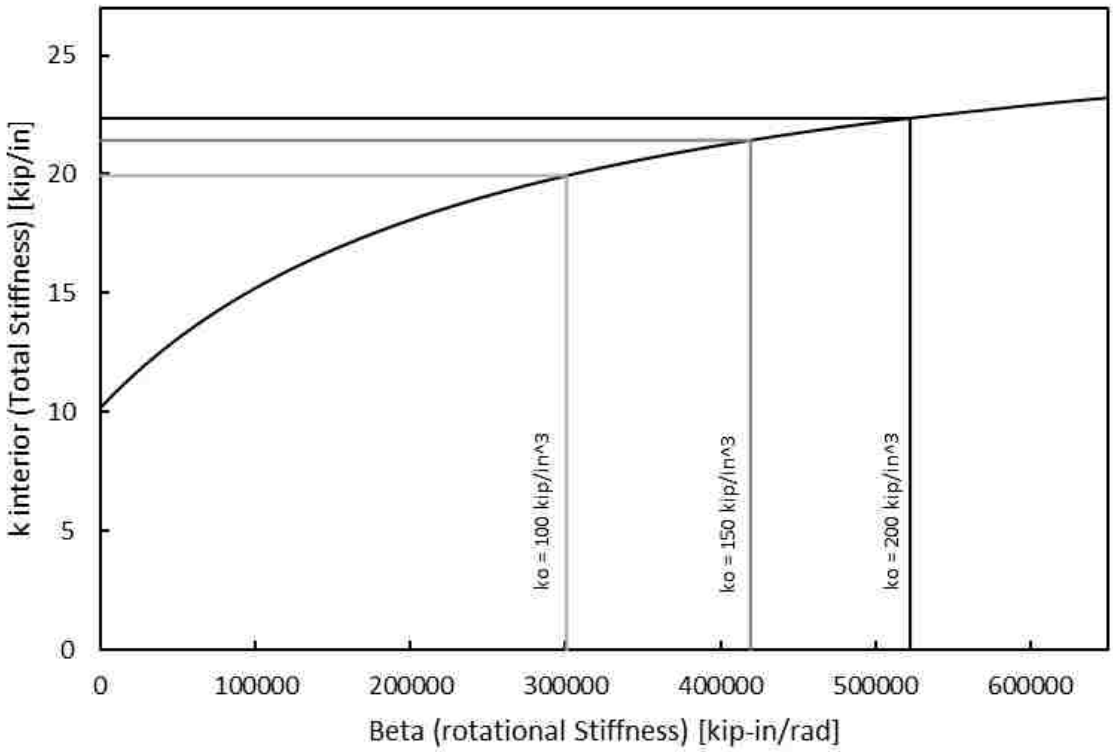

Figure 5-21: Plot of total stiffness versus rotational stiffness for interior assembly (W10x77 – 7 inches embedment depth).

Figure 5-22 is also for an interior column assembly using the W10 × 77 shape, a beam shape of a similar moment of inertia, and 15 inches of column embedment depth. The figure shows that the rotational stiffness ranges between 398,195 kip-in/rad and. 626,350 kip-in/rad. This is the same range as seen in Figure 5-20; however, the range resulted in an increased total

stiffness values between 21.2 kip/in and 23.1 kip/in. The high end of β is 57% greater than the low end β, and the high end of stiffness is 9% greater than the low end. Therefore, stiffness can probably be predicted within 9%. Additional analysis of Figure 5-21 and Figure 5-22 is found in Table 5-6.

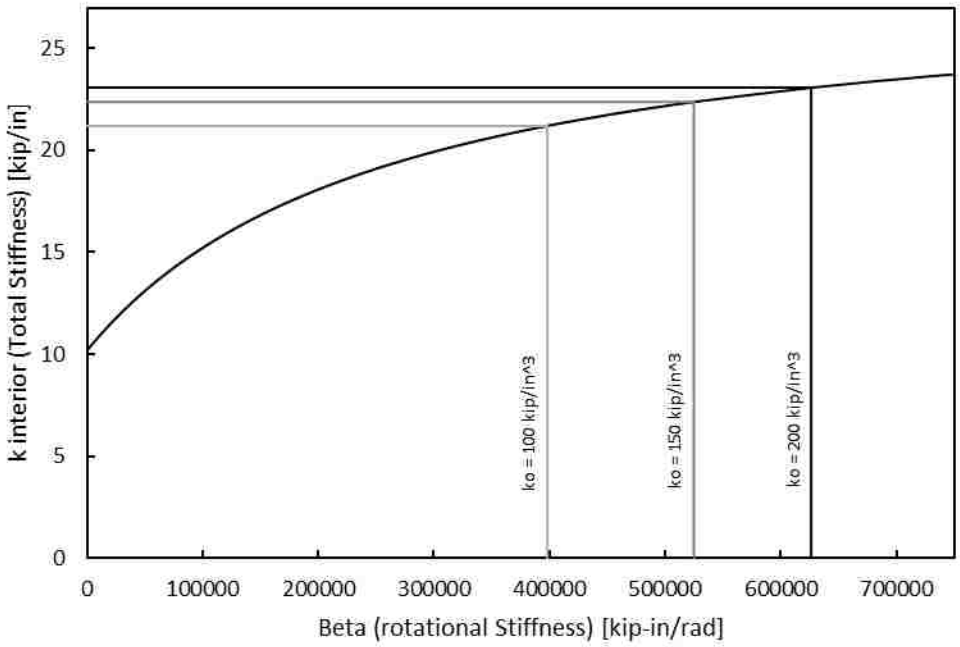

Figure 5-22: Plot of total stiffness versus rotational stiffness for interior assembly (W10x77 – 15 inches embedment depth).

Table 5-6: W10x77 Interior Percent Change Comparison of Stiffness

Embedment Depth (inches)	Modulus of Subgrade Reaction (k_o=kips/in^3)	Value of β (kip-in/rad)	Value of Total Stiffness (kip/in)
7	100	300,809	19.9
	150	419,380	21.4
	200	522,451	22.35
15	100	398,195	21.2
	150	524,920	22.4
	200	626,350	23.1

5.4 Summary

The total stiffness is very for values of β from around 1e+04 to 1e+06. However, the exact values will vary as shown herein for the W10 and W8 columns. The effect of β remains semi-regular for different shapes as well as for the different column configurations used during investigation. The main difference was in the total stiffness per column. It was expected that the moment frame with partial fixity at the base would have greater stiffness then a single partially fixed column.

Better accuracy in predicting the rotational stiffness is obtained with better estimation of the modulus of subgrade reaction; however, even if the rotational stiffness may only be predicted to within a 100%, then the total stiffness of a partially fixed frame may be predicted only within a 15% to 20% change. The percentage was reduced based on the type of configuration use.

6 CONCLUSIONS

This thesis outlined the work done to further the understanding of the rotational stiffness of shallow embedded columns. This thesis evaluated the model created by Tryon with the data collected from the physical test conducted by Barnwell and Hanks. The research completed for this thesis resulted in creating an improved model.

The new model shows:

1. The modulus of subgrade reaction was a sensitive parameter for the model. However, when the modulus of subgrade reaction is in the correct range for the column connection then there is not a large change on the total stiffness.
2. The exposed length did not have a large effect on the model predicted results, especially for small changes.
3. The modulus of concrete for the slab and the blockout had a large effect on the model predicted results.
4. Flange effective width was not an influential parameter to the model. It appeared that only one flange acted in resistance against the concrete blockout was a better estimation.
5. The base plate thickness had a large effect on the predicted rotational stiffness, by adjusting the effective column depth.

6. The model was not a good predictor for little to no embedment depth due to the lack of specimen data.
7. Shallow embedded columns had a great deal more stiffness than a pinned system and less stiffness than a fixed system.
8. Values for beta or the stiffness of the rotational spring were in the sensitive region; however, a large change in the spring stiffness will result in a change of less than 20% in the stiffness of the whole system.

This model was meant as an approximation and to give a good range for estimating rotational stiffness values. However, it is important to use good judgement and check the limits of your design, since, the number of anchor bolts, base plate thickness, embedment depth, column and or beam size as well as the type of loads that the system is subjected to has a large effect on the design. Different shapes other than the wide flange shape may not work with this model.

Further research could be completed by adding in more data sets with more range in shape sizes and embedment depths, so that more accurate curves can be developed. Additional tests should be done for the weak orientation, since there were only two points in all the data presented.

REFERENCES

Barnwell, N. V. (2015). Experimental Testing of Shallow Embedded Connections Between Steel Columns and Concrete Footings. (Master of Science), Brigham Young University.

Cui, Y., Nagae, T., & Nakashima, M. (2009). Hysteretic behavior and strength capacity of shallowly embedded steel column bases. Journal of structural engineering, 135(10), 1231-1238.

DeWolf, J. T., & Sarisley, E. F. (1980). Column base plates with axial loads and moments. Journal of the Structural Division, 106(11), 2167-2184.

Fisher, J. M. and L. A. Kloiber (2006). Base Plate and Anchor Rod Design, 2nd Ed. American Institute of Steel Construction.

Grilli, D. A., & Kanvinde, A. M. (2015). Embedded column base connections subjected to flexure and axial load: Tests and strength models.

Grilli, D. A., & Kanvinde, A. M. (2017). Embedded column base connections subjected to seismic loads: Strength model. Journal of Constructional Steel Research, 129, 240-249.

Hanks, K. N. (2016). Rotational Strength and Stiffness of Shallowly Embedded Base Connections in Steel Moment Frames. (Master of Science), Brigham Young University.

Hetényi, M. (1971). Beams on elastic foundation: theory with applications in the fields of civil and mechanical engineering: University of Michigan.

Kanvinde, A. M., & Deierlein, G. G. (2011). Recent research on column base connections. Modern Steel Construction.

Kanvinde, A. M., Grilli, D. A., & Zareian, F. (2011). Rotational stiffness of exposed column base connections: Experiments and analytical models. Journal of structural engineering, 138(5), 549-560.

Kanvinde, A. M., Jordan, S. J., & Cooke, R. J. (2013). Exposed column base plate connections in moment frames-Simulations and behavioral insights. Journal of Constructional Steel Research, 84, 82-93.

Rodas, P. T., Zareian, F., & Kanvinde, A.M. (2017). Rotational stiffness of Deeply Embedded Column-Base Connections. Journal of structural engineering, 143(8): 04017064.

Sall, O. A., Fall, M., Berthaud, Y., & Ba, M. (2013). Influence of the Elastic Modulus of the Soil and Concrete Foundation on the Displacements of a Mat Foundation. *Open Journal of Civil Engineering, 3*(04), 228

Tryon, J. E. (2016). Simple Models for Estimating the Rotational Stiffness of Steel Column-to-Footing Connections. (Master of Science), Brigham Young University.

APPENDIX A

Half Moment Frame With Nodes A, B, and C

Step 1: Construct indiviual member k matrix

k hat for member AB

$$k_{hatab} = \begin{pmatrix} \frac{E\cdot A_c}{H} & 0 & 0 & -\frac{E\cdot A_c}{H} & 0 & 0 \\ 0 & \frac{12\cdot E\cdot I_c}{H^3} & \frac{6\cdot E\cdot I_c}{H^2} & 0 & -\frac{12\cdot E\cdot I_c}{H^3} & \frac{6\cdot E\cdot I_c}{H^2} \\ 0 & \frac{6\cdot E\cdot I_c}{H^2} & \frac{4\cdot E\cdot I_c}{H} & 0 & -\frac{6\cdot E\cdot I_c}{H^2} & \frac{2\cdot E\cdot I_c}{H} \\ -\frac{E\cdot A_c}{H} & 0 & 0 & \frac{E\cdot A_c}{H} & 0 & 0 \\ 0 & -\frac{12\cdot E\cdot I_c}{H^3} & -\frac{6\cdot E\cdot I_c}{H^2} & 0 & \frac{12\cdot E\cdot I_c}{H^3} & -\frac{6\cdot E\cdot I_c}{H^2} \\ 0 & \frac{6\cdot E\cdot I_c}{H^2} & \frac{2\cdot E\cdot I_c}{H} & 0 & -\frac{6\cdot E\cdot I_c}{H^2} & \frac{4\cdot E\cdot I_c}{H} \end{pmatrix}$$

$$T = \begin{pmatrix} 0 & 1 & 0 & 0 & 0 & 0 \\ -1 & 0 & 0 & 0 & 0 & 0 \\ 0 & 0 & 1 & 0 & 0 & 0 \\ 0 & 0 & 0 & 0 & 1 & 0 \\ 0 & 0 & 0 & -1 & 0 & 0 \\ 0 & 0 & 0 & 0 & 0 & 1 \end{pmatrix}$$

Transform so that the member is vertical

$$k_{ab} = T^T \cdot k_{hatab} \cdot T$$

$$k_{ab} = \begin{pmatrix} \frac{12 \cdot E \cdot I_c}{H^3} & 0 & -\frac{6 \cdot E \cdot I_c}{H^2} & -\frac{12 \cdot E \cdot I_c}{H^3} & 0 & -\frac{6 \cdot E \cdot I_c}{H^2} \\ 0 & \frac{A_c \cdot E}{H} & 0 & 0 & -\frac{A_c \cdot E}{H} & 0 \\ -\frac{6 \cdot E \cdot I_c}{H^2} & 0 & \frac{4 \cdot E \cdot I_c}{H} & \frac{6 \cdot E \cdot I_c}{H^2} & 0 & \frac{2 \cdot E \cdot I_c}{H} \\ -\frac{12 \cdot E \cdot I_c}{H^3} & 0 & \frac{6 \cdot E \cdot I_c}{H^2} & \frac{12 \cdot E \cdot I_c}{H^3} & 0 & \frac{6 \cdot E \cdot I_c}{H^2} \\ 0 & -\frac{A_c \cdot E}{H} & 0 & 0 & \frac{A_c \cdot E}{H} & 0 \\ -\frac{6 \cdot E \cdot I_c}{H^2} & 0 & \frac{2 \cdot E \cdot I_c}{H} & \frac{6 \cdot E \cdot I_c}{H^2} & 0 & \frac{4 \cdot E \cdot I_c}{H} \end{pmatrix}$$

k for member BC

$$k_{bc} = \begin{bmatrix} \frac{E \cdot A_b}{\frac{L}{2}} & 0 & 0 & -\frac{E \cdot A_b}{\frac{L}{2}} & 0 & 0 \\ 0 & \frac{12 \cdot E \cdot I_b}{\left(\frac{L}{2}\right)^3} & \frac{6 \cdot E \cdot I_b}{\left(\frac{L}{2}\right)^2} & 0 & -\frac{12 \cdot E \cdot I_b}{\left(\frac{L}{2}\right)^3} & \frac{6 \cdot E \cdot I_b}{\left(\frac{L}{2}\right)^2} \\ 0 & \frac{6 \cdot E \cdot I_b}{\left(\frac{L}{2}\right)^2} & \frac{4 \cdot E \cdot I_b}{\frac{L}{2}} & 0 & -\frac{6 \cdot E \cdot I_b}{\left(\frac{L}{2}\right)^2} & \frac{2 \cdot E \cdot I_b}{\frac{L}{2}} \\ -\frac{E \cdot A_b}{\frac{L}{2}} & 0 & 0 & \frac{E \cdot A_b}{\frac{L}{2}} & 0 & 0 \\ 0 & -\frac{12 \cdot E \cdot I_b}{\left(\frac{L}{2}\right)^3} & -\frac{6 \cdot E \cdot I_b}{\left(\frac{L}{2}\right)^2} & 0 & \frac{12 \cdot E \cdot I_b}{\left(\frac{L}{2}\right)^3} & -\frac{6 \cdot E \cdot I_b}{\left(\frac{L}{2}\right)^2} \\ 0 & \frac{6 \cdot E \cdot I_b}{\left(\frac{L}{2}\right)^2} & \frac{2 \cdot E \cdot I_b}{\frac{L}{2}} & 0 & -\frac{6 \cdot E \cdot I_b}{\left(\frac{L}{2}\right)^2} & \frac{4 \cdot E \cdot I_b}{\frac{L}{2}} \end{bmatrix}$$

k for the spring

$$k_{spring} = \frac{\beta}{H^2}$$

Step 2: Construct the global K matrix

Corresponding DOF

$$K_{global} = \begin{pmatrix} \frac{4\cdot E\cdot I_c}{H} + \beta & \frac{6\cdot E\cdot I_c}{H^2} & \frac{2\cdot E\cdot I_c}{H} & 0 \\ \frac{6\cdot E\cdot I_c}{H^2} & \frac{12\cdot E\cdot I_c}{H^3} + \frac{A_b\cdot E}{\frac{L}{2}} + -\frac{E\cdot A_b}{\frac{L}{2}} & \frac{6\cdot E\cdot I_c}{H^2} + 0 + 0 & 0 + 0 \\ \frac{2\cdot E\cdot I_c}{H} & \frac{6\cdot E\cdot I_c}{H^2} & \frac{4\cdot E\cdot I_c}{H} + \frac{4\cdot E\cdot I_b}{\frac{L}{2}} & \frac{2\cdot E\cdot I_b}{\frac{L}{2}} \\ 0 & 0 & \frac{2\cdot E\cdot I_b}{\frac{L}{2}} & \frac{4\cdot E\cdot I_b}{\frac{L}{2}} \end{pmatrix} \begin{matrix} \theta_A \\ \Delta_{BlC} \\ \theta_B \\ \theta_C \end{matrix}$$

Step 3: Develop the global F vector

Corresponding DOF

$$F = \begin{pmatrix} 0 \\ \text{Force} \\ 0 \\ 0 \end{pmatrix} \begin{matrix} \theta_A \\ \Delta_{BlC} \\ \theta_B \\ \theta_C \end{matrix}$$

Force is applied horizontally at node B

Step 4: Find all displacments and deformations

$$U = K_{global}^{-1} \cdot F$$

$$U = \begin{bmatrix} -\dfrac{Force \cdot \left(3 \cdot I_b \cdot H^2 + I_c \cdot L \cdot H\right)}{6 \cdot E \cdot I_b \cdot I_c + 6 \cdot H \cdot I_b \cdot \beta + I_c \cdot L \cdot \beta} \\ \dfrac{Force \cdot \left(3 \cdot H^4 \cdot I_b \cdot \beta + 12 \cdot E \cdot H^3 \cdot I_b \cdot I_c + 2 \cdot H^3 \cdot I_c \cdot L \cdot \beta + 6 \cdot E \cdot H^2 \cdot I_c^{\,2} \cdot L\right)}{36 \cdot I_b \cdot E^2 \cdot I_c^{\,2} + 6 \cdot L \cdot \beta \cdot E \cdot I_c^{\,2} + 36 \cdot H \cdot I_b \cdot \beta \cdot E \cdot I_c} \\ -\dfrac{Force \cdot \left(L \cdot \beta \cdot H^2 + 2 \cdot E \cdot I_c \cdot L \cdot H\right)}{12 \cdot E^2 \cdot I_b \cdot I_c + 12 \cdot E \cdot H \cdot I_b \cdot \beta + 2 \cdot E \cdot I_c \cdot L \cdot \beta} \\ \dfrac{Force \cdot \left(E \cdot I_c \cdot L + H \cdot L \cdot \beta\right) \cdot \left(\beta \cdot H^2 + 2 \cdot E \cdot I_c \cdot H\right)}{\left(2 \cdot E \cdot I_c + 2 \cdot H \cdot \beta\right) \cdot \left(12 \cdot E^2 \cdot I_b \cdot I_c + 12 \cdot E \cdot H \cdot I_b \cdot \beta + 2 \cdot E \cdot I_c \cdot L \cdot \beta\right)} \end{bmatrix}$$

Corresponding DOF

θ_A

Δ_{BlC}

θ_B

θ_C

Step 5: Determine the stiffness of the system at the base

Stiffness of the system is

$$K = \frac{Force}{\Delta_{BlC}}$$

$$K = \frac{36 \cdot I_b \cdot E^2 \cdot I_c^{\,2} + 6 \cdot L \cdot \beta \cdot E \cdot I_c^{\,2} + 36 \cdot H \cdot I_b \cdot \beta \cdot E \cdot I_c}{3 \cdot H^4 \cdot I_b \cdot \beta + 12 \cdot E \cdot H^3 \cdot I_b \cdot I_c + 2 \cdot H^3 \cdot I_c \cdot L \cdot \beta + 6 \cdot E \cdot H^2 \cdot I_c^{\,2} \cdot L}$$

This is the stiffness for the half moment frame.

For the full moment frame use 2*K